EPFL

Thèse n° 10080

Development of next-generation microfluidic systems for enhanced, faster, and cost-effective immunoassays for tissue diagnostics - Ac electrothermal flow & Acoustofluidics

Présentée le 20 septembre 2023

Faculté des sciences et techniques de l'ingénieur
Laboratoire de microsystèmes 2
Programme doctoral en microsystèmes et microélectronique

pour l'obtention du grade de Docteur ès Sciences

par

Muaz Salama Abdelmonem DRAZ

Acceptée sur proposition du jury

Prof. G. Boero, président du jury
Prof. M. Gijs, Dr D. G. Dupouy, directeurs de thèse
Prof. A. deMello, rapporteur
Prof. N. Paust, rapporteur
Prof. H. Shea, rapporteur

École polytechnique fédérale de Lausanne

2023

I dedicate this work to the unsung heroes of this world, whose names may never grace the headlines but whose impact is immeasurable, and whose tireless efforts and selfless acts of kindness weave a tapestry of love and compassion that uplifts humanity

Acknowledgments

I would like to express my extreme gratitude to my advisor Prof. Martin Gijs for offering me to be part of this collaboration and for his support during the Ph.D. Martin gave me a unique opportunity to try and test several ideas and trusted me to initiate and build whole new projects within the Ph.D., yet he was available all the time for our discussions and always motivated me to focus and look deeper, and think in unconventional ways. He offered me a lot of flexibility in the Ph.D. and schedule planning, and on a personal level, he is a very modest person. Thank you, Martin, for your support.
I would love to thank the respectful committee for offering their time and expertise to evaluate and discuss the current work. I would like to express my gratitude to Prof. Giovanni Boero, Prof. Herbert Shea, Prof. Andrew DeMello, and Prof. Nils Paust for their time and efforts to review and discuss the current thesis work and their valuable feedback.

I would like also to thank Dr. Diego G. Dupouy from our industrial partner Lunaphore Technologies. Thanks to this collaboration, I was able to conduct my Ph.D. research in an industrial environment in parallel to the university. This luckily gave me the opportunity, not just to test and develop new scientific ideas, but to tailor them to the industry needs and integrate them at the market device level. Diego, despite his busy schedule as the company CTO, has been always trying to be present for our meetings and discussions to ensure that we achieve the best results.

I would like to give a million special thanks to all my friends and colleagues, both in EPFL and Lunaphore, for being part of my Ph.D. journey and supporting me. I would like to thank Daniel Migliozzi for his early support in the Ph.D., Farzad Rezaeianaran for our interesting and never-ending discussions and his companionship during the last years, Asim Faridi for our scientific discussions, Melis Martin for her continuous support in the lab from first to the last day of the Ph.D. and her quick support with our research and administrative processes, Lucie Auberson for her support on all the university and institute matters and her efforts to find solutions for the students' problems, and Abdeljalil Sayah for his support all the time in the lab. I would love to thank Thomas Lehnert and Arnaud Bertsch for their help with the abstract translations into German and French. Additionally, I am thankful to all other teams and labs in EPFL who offered us great support and help including the CMI and the different EDMI and SV labs. I would like to thank everyone on Lunaphore from the application development scientists to the R&D, HW, and SW teams to the HR and all other teams, for providing me with all that I needed to progress in our projects. This includes Pino Bordignon, Benjamin Pelz, Marco Ammann, Pierre Joris, Sylvain Scalmazzi, Walid Bellafdil, Joanna Kowal, Saska Brajkovic, Emilie Pérès, Jonathan Mignot, Anais Ly, Alix Faillétaz, Abdelillah Al Baraka, Victor de Gautard, Lionel Mury, Alice Comberlato, Samuel Aubert, Lorenzo Bruno, Deniz Eroglu, Pedro Machado Almeida, , Alexandre Kehren, Cansaran Saygili Demir, Delphine Vacheron, Kim-Yen Nguyen, Doris Loutan, Dimitry Dumont-Fillon, Matthieu Rüegg, Niels Saalfeldt, Coralyne Saint-Cirel, Marc Mato Sabat, and Bruno Davicino and all other employees in Lunaphore.

This Ph.D. would have been possible to even start without the support of my dear family. All my personal and academic and career achievements wouldn't have existed without the support, love, and

faith of two parents who sacrificed countless times with the least provided support, to make us, me and my brothers, being highly successful in our lives and being active member towards the society. They still remind us to never forget the poor, the hungry, and those in need among us. My ultimate and deepest gratitude and admiration to Salama Draz and Oumayma Noamany. My life wouldn't have been such joyful without Mohamed, Moustafa, and Muhannad and their families and kids. Being with them provides me with a huge dose of happiness and the only sad part is when it is time to leave them. Finally, I am speechless when it comes to thinking of how my life turned out to be today with the support of Zahraa Ghanem and Yusr Muaz Draz. These two sweet and lovely angles were the guards of my life on a daily basis and have given me the support and the faith to fight depression and frustration. Zahraa sacrificed her scientific career so we can still all be together, and she took care of us ultimately and very kindly, and I am not exaggerating if I said she owns a large part of this Ph.D. I never understood my parents` feelings towards us until I was blessed with Yusr, Yusr means Easy, and indeed, she brought with her all the easiness, happiness, and kindness to our lives. Till now, I still can't believe how a small creature can be the major cornerstone of an adult's whole life. There are no available words that can express my feelings towards you both, but simply, thank you for every moment and for being here always.

Abstract

Microfluidics has had already a significant impact on science and humanity, by providing new experimental techniques that have numerous real-life and industrial applications. Its use spans across various scientific fields, including but not limited to biomedical research, medical diagnostics, pharmaceutical discovery, and environmental monitoring. Indeed, several advantages are offered by microfluidics, such as low reagents consumption, miniaturization and portability, high-throughput analysis, and high surface-to-volume ratios.

The application of microfluidics in the field of surface-based assays and more specifically, the spatial molecular profiling of tumor tissues has gained a lot of interest, especially with the increased interest in personalized medicine and targeted therapy. In this case, a large dissected and thin tissue section of a tumor is mounted on a substrate slide and incubated inside a microfluidic chamber for subsequent immunostaining and analysis. Subsequently, different specific immune detection reagents can be employed to immune-label the marker(s) of interest. This allows for detecting the presence and the level of expression of the biomarkers. The two most common techniques for tissue diagnostics are immunohistochemistry (IHC) and in situ hybridization (ISH). In IHC, the expression of protein markers can be detected (proteomics), while in ISH, the gene expression (transcriptomics) in the cellular environment can be analyzed.

During a static incubation of the immunoreaction reagents with the tissue section, the reagents begin to adsorb and bind to the target epitopes on the tissue sample. However, the laminar fluid flow associated with the small dimensions of microfluidic systems and the domination of the diffusional mass transport of reagents can limit their transport to the tissue. Furthermore, during the reaction time, a depletion region is formed around the target area with a much lower abundance of the reagent. At this point, the reaction rate becomes limited due to the scarcity of the detection reagents and their diffusion-limited transport, which can lead to very lengthy experiments. Moreover, uniform staining of the tissue plays an important role in the analysis, since it ensures that all relevant antigen epitopes on the tissue are equally exposed to the detection reagents, thereby enhancing the signal contrast and facilitating quantifiable detection. Non-uniform staining may jeopardize the analysis of the tumor section and lead to a false or biased diagnosis or prognosis.

In the current work, we have investigated and integrated two microfluidic mixing techniques, including AC electrothermal flow (ACET- Chapters 2, and 3), and acoustofluidic mixing (AF- chapter 4). ACET is an AC electrokinetic technique that can generate microfluidic vortices above the electrodes embedded in the chamber, which are actuated with an electrical AC signal leading to local temperature gradients that provide the driving force for the fluid flow. Here, we report a novel ACET electrode design concept for generating in-plane microfluidic mixing vortices that act over a large volume and close to the reaction surface of interest. This is different from the traditional ACET parallel electrode design that provides rather local vertical mixing vortices directly above the electrodes. As a proof of concept, the new design has been used in ACET-enhanced immunoassays to improve the immunostaining signal of the HER2 cancer biomarker (Human epidermal growth factor receptor 2) on

breast cancer cells. In addition to that, the concept of scaling up the design has been proven to enable the mixing of the fluid over large microfluidic volumes, which further enhances the immunoassay's output. We have achieved a 6-times enhancement in the assay signal with a 75% reduction in assay time. Moreover, we also provide detailed insight into the working mechanism of the new ACET design using finite element method simulations, allowing us to propose several new designs for the ACET in-plane microfluidic motion. Finally, a preliminary in-plane design is investigated for the application of our design in microfluidic pumping.

In the second topic of our research, AF mixing could be easily integrated into an industrial prototype system for fast and automatic tissue diagnostics by simply attaching two commercial AF actuators to the existing microfluidic staining system. Our new proposed AF technology has the advantage of the ease of integration, and operation at low frequencies (< 10 KHz range) thus omitting the need for advanced and high-frequency electronic devices, low cost of the core piezo-electric actuation elements, and retaining the possibility of microscopic imaging over the complete microfluidic chamber, and, finally, the absence of thermal interference with the conducted staining experiments. AF mixing was successfully used to achieve uniform staining on large cancer cell pellet sections, even when using small fluid flows and short incubation times. AF mixing could reduce by 80% the incubation time of the Her2 and CK (Cytokeratins) biomarkers on breast cancer cell pellets with respect to the existing protocol of spatial immunostaining, and reduce their concentration by 66% while achieving a higher signal-to-background ratio than obtained in comparable spatially resolved immunoassays with static incubation.

Keywords

Microfluidics, ac electrothermal, acoustofluidic, spatial proteomics, immunofluorescence, tumor diagnostics, microfluidic mixing, diffusional transport, tissue analytics, laminar flow, ac electrokinetics, acoustic streaming, immunohistochemistry, human epidermal growth factor receptor 2 (HER2), pan-cytokeratin, microfabrication, immunofluorescence, image processing analysis.

Résumé

La microfluidique a déjà eu un impact significatif sur la science et l'humanité, en produisant de nouvelles techniques expérimentales qui ont de nombreuses applications concrètes et industrielles. Son utilisation s'étend à divers domaines scientifiques, notamment la recherche biomédicale, le diagnostic médical, la découverte pharmaceutique et la surveillance environnementale. En effet, la microfluidique présente plusieurs avantages tels que la faible consommation de réactifs, la miniaturisation et la portabilité, l'analyse à haut débit et les rapports surface-volume élevés.

L'application de la microfluidique dans le domaine des dosages par interaction avec des surfaces et plus spécifiquement le profilage moléculaire spatial des tissus tumoraux a suscité beaucoup d'intérêt, en particulier avec l'attrait croissant des médecines personnalisées et de la thérapie ciblée. Dans ce cas, une grande surface de tissu tumoral disséqué, de fine épaisseur est montée sur une lame de substrat et incubée à l'intérieur d'une chambre microfluidique pour un immunomarquage et une analyse ultérieure. Ensuite, différents réactifs permettant une détection immunitaire spécifique peuvent être utilisés pour l'immunomarquage du (des) marqueur(s) d'intérêt. Cela permet de détecter la présence et le niveau d'expression des biomarqueurs. Les deux techniques les plus courantes pour le diagnostic tissulaire sont l'immunohistochimie (IHC) et l'hybridation in situ (ISH). En IHC, l'expression de marqueurs protéiques peut être détectée (protéomique), tandis qu'en ISH, l'expression génique (transcriptomique) dans l'environnement cellulaire peut être analysée.

Au cours d'une incubation statique des réactifs d'immunoréaction avec le tissu prélevé, les réactifs commencent à s'adsorber et à se lier aux épitopes cibles sur l'échantillon de tissu. Cependant, l'écoulement laminaire des fluides lié aux petites dimensions des systèmes microfluidiques et la dominance du transport de masse diffusif des réactifs peut limiter leur transport vers le tissu. De plus, pendant le temps de réaction, une région de déplétion se forme autour de la zone cible avec un afflux bien moindre du réactif. À ce stade, le taux de réaction devient limité en raison de la rareté des réactifs de détection et de leur transport limité par diffusion, ce qui peut conduire à des expériences très longues. De plus, l'uniformité de la coloration du tissu joue un rôle important dans l'analyse, car elle garantit que tous les épitopes antigéniques pertinents du tissu sont également exposés aux réactifs de détection, améliorant ainsi le contraste du signal et facilitant une détection quantifiable. Une coloration non uniforme peut compromettre l'analyse du prélèvement tumoral et conduire à un diagnostic ou à un pronostic faux ou biaisé.

Dans le cadre de ce travail, nous avons étudié et intégré deux techniques de mélange microfluidique, à savoir le mélange par flux électrothermique AC (ACET - chapitres 2 et 3) et le mélange acoustofluidique (AF - chapitre 4). ACET est une technique électrocinétique à courant alternatif, qui peut générer des tourbillons microfluidiques au-dessus des électrodes intégrées dans la chambre. Ces dernières sont actionnées par un signal électrique AC générant des gradients de température locaux induisant la force motrice pour l'écoulement du fluide. Nous présentons ici un nouveau concept de conception d'électrode ACET pour générer dans le plan, la vorticité nécessaire au mélange microfluidique. Ces électrodes agissent sur un grand volume et à proximité de la surface où ont lieu

les réactions étudiées. Ceci diffère de la conception d'électrode parallèle ACET traditionnelle qui permet d'obtenir des tourbillons verticaux localisés directement au-dessus des électrodes. À titre de preuve de concept, le nouvel agencement d'électrodes a été utilisée dans des tests immunologiques pour améliorer le signal d'immunomarquage du biomarqueur de cancer HER2 (récepteur 2 du facteur de croissance épidermique humain) sur les cellules cancéreuses du sein. De plus, le changement d'échelle de ce concept a été démontré et permet le mélange de grands volumes microfluidiques, ce qui renforce encore le signal du test immunologique : Le signal a été multiplié par 6 avec une réduction de 75% du temps d'analyse. En outre, nous avons également étudié en détail le mécanisme de fonctionnement du nouvel agencement ACET à l'aide de simulations par éléments finis, ce qui nous permet de proposer plusieurs nouveaux agencements permettant le mouvement microfluidique dans le plan par ACET. Enfin, une étude préliminaire de pompe microfluidique a été menée, utilisant également des électrodes planaires.

Dans le deuxième volet de notre recherche, le mélange acoustofluidique (AF) a pu être facilement intégré dans un système prototype industriel pour des diagnostics rapides et automatiques de biopsies tissulaires en attachant simplement deux actionneurs AF commerciaux au système de coloration microfluidique existant. Notre nouvelle technologie AF présente l'avantage de la facilité d'intégration en raison d'un fonctionnement à basse fréquence (<10 kHz) éliminant ainsi le besoin de dispositifs électroniques avancés et haute fréquence. Le coût des éléments d'actionnement piézoélectrique qu'elle utilise est réduit, et elle permet la possibilité d'imagerie microscopique sur l'ensemble de la chambre microfluidique. Enfin, dans cette technique, il n'y a pas d'interférence thermique avec les expériences de coloration menées. Le mélange AF a été utilisé avec succès pour obtenir une coloration uniforme sur de grandes surfaces de biopsies de tumeurs cancéreuses, même lors de l'utilisation de faibles débits de fluides et de courtes durées d'incubation. Le mélange AF a permis de réduire de 80% le temps d'incubation des biomarqueurs Her2 et CK (Cytokératines) sur des biopsies de cellules cancéreuses mammaires par rapport au protocole existant de coloration immunospatiale, et de réduire leur concentration de 66%, tout en obtenant un rapport signal sur bruit plus élevé que celui obtenu dans des tests immunologiques résolus spatialement comparables avec une incubation statique.

Mots-clés

Microfluidique, électrothermique AC, acoustofluidique, protéomique spatiale, immunofluorescence, diagnostic de tumeur, mélange microfluidique, transport diffusif, analyse de tissus, écoulement laminaire, électrocinétique AC, streaming acoustique, immunohistochimie, récepteur 2 du facteur de croissance épidermique humain (HER2), pan-cytokératine, microfabrication, immunofluorescence, analyse de traitement d'image.

Zusammenfassung

Die Mikrofluidik hat bereits einen signifikanten Einfluss auf Wissenschaft und Menschheit, indem sie neue experimentelle Techniken bereitstellt, die zahlreiche Anwendungen im realen Leben und in der Industrie finden. Ihr Einsatz erstreckt sich auf verschiedene wissenschaftliche Bereiche, einschließlich der biomedizinischen Forschung, der medizinischen Diagnostik, pharmazeutischer Entwicklungen und der Umweltüberwachung. Tatsächlich bietet die Mikrofluidik mehrere Vorteile, insbesondere einen geringen Verbrauch von Reagenzien, Miniaturisierung und Portabilität, Hochdurchsatzanalyse und ein hohes Oberflächen-zu-Volumen Verhältnis.

Die Anwendung der Mikrofluidik im Bereich von Oberflächenassays, insbesondere der räumlichen molekularen Profilierung von Tumorgeweben, hat viel Interesse gewonnen, vor allem im Hinblick auf das zunehmende Interesse an personalisierter Medizin und gezielter Therapie. In diesem Fall wird ein großes, dünnes Gewebeschnittstück eines Tumors auf einem Substratträger montiert und in einer Mikrofluidikkammer inkubiert, immunhistologisch gefärbt und analysiert. Es können verschiedene spezifische Immunerkennungsreagenzien eingesetzt werden, um entsprechende Marker zu kennzeichnen. Dies ermöglicht die Detektion der Anwesenheit und der Intensität der Indikatoren. Die beiden gängigsten Techniken für die Gewebediagnostik sind die Immunhistochemie (IHC) und die In-situ Hybridisierung (ISH). In der IHC wird die Expression von Proteinmarkern (Proteomik) nachgewiesen, während in der ISH die Genexpression (Transkriptomik) im zellulären Umfeld analysiert wird.

Während einer statischen Inkubation adsorbieren die Immunreaktionsreagenzien auf der Gewebeprobe und binden an die Zielepitope. Der mit den geringen Abmessungen von Mikrofluidsystemen verbundene laminare Flüssigkeitsfluss und die Dominanz von diffusivem Massentransport kann jedoch den Transport der Reagenzien zum Gewebe begrenzen. Während der Reaktionszeit bildet sich um den Zielbereich zudem eine Region mit einer stark reduzierten Konzentration der aktiven Moleküle. An diesem Punkt wird die Reaktionsrate aufgrund der Knappheit der Nachweisreagenzien und des diffusiven Transports begrenzt, was zu sehr langen Experimenten führen kann. Darüber hinaus spielt bei der Analyse eine gleichmäßige Färbung des Gewebes eine wichtige Rolle, da dies sicherstellt, dass alle relevanten Antigenepitope auf dem Gewebe gleichermaßen den Reagenzien ausgesetzt sind. Dies verbessert den Signalkontrast und erleichtert einen quantifizierbaren Nachweis. Eine ungleichmäßige Färbung kann die Analyse des Tumorabschnitts beeinträchtigen und zu einer ungenauen oder falschen Diagnose bzw. Prognose führen.

Im Rahmen der vorliegenden Dissertation haben wir zwei mikrofluidische Mischtechniken untersucht und integriert, nämlich die AC Elektrothermische Strömung (ACET - Kapitel 2 und 3) und die akustofluidische Mischmethode (AF - Kapitel 4). ACET ist eine elektrokinetische Technik, die Mikrofluidikwirbel über in der Kammer eingebetteten Elektroden erzeugt. Diese werden mit einem elektrischen AC Signal betrieben, das zu lokalen Temperaturgradienten führt, die die treibende Kraft für die Flüssigkeitsströmung liefern. Hier berichten wir über ein neuartiges Konzept des ACET

Elektrodendesigns zur Erzeugung von «in-plane» Mikrofluidikwirbeln, die über ein großes Volumen und in der Nähe der Reaktionsfläche wirken. Dies unterscheidet sich vom traditionellen ACET Parallelelektrodendesign, das lokale vertikale Mischwirbel direkt über den Elektroden erzeugt. Als Proof-of-Concept wurde das neue Design in ACET-verstärkten Immunoassays eingesetzt, um das Immunfärbesignal des HER2 Krebsbiomarkers (Humanes Epidermales Wachstumsfaktor-Rezeptor 2) auf Brustkrebszellen zu verbessern. Zusätzlich konnte auch durch eine Hochskalierung des Designs das Mischen großer Mikrofluidikvolumina ermöglicht werden, was den Output des Immunoassays weiter verbessert. Wir haben eine 6-fache Verbesserung des Assaysignals bei einer 75%-igen Reduktion der Assayzeit erreicht. Außerdem bieten wir, unter Verwendung von Finite-Elemente-Methoden-Simulationen, detaillierte Einblicke in den Funktionsmechanismus des neuen ACET Designs, was uns ermöglichte, mehrere Konfigurationen für die ACET «in-plane» Mikrofluidikbewegung vorzuschlagen. Schließlich untersuchen wir ein vorläufiges «in-plane» Konzept für die Anwendung als Mikrofluidikpumpen.

Im Rahmen des zweiten Themas unserer Forschung könnte die AF-Mischtechnik einfach in ein industrielles prototypisches System für schnelle und automatische Gewebediagnostik integriert werden. In diesem Fall würde man einfach zwei kommerzielle AF-Generatoren an das vorhandene Mikrofluidikfärbungssystem anbringen. Unsere neue AF-Technologie bietet den Vorteil einer einfachen Systemintegration und den Betrieb bei niedrigen Frequenzen (< 10 kHz), wodurch die Notwendigkeit fortschrittlicher und hochfrequenter elektronischer Geräte entfällt. Weitere Vorteile sind geringe Kosten der Piezo-Elektroaktuationselemente, die Möglichkeit der mikroskopischen Abbildung über die gesamte Mikrofluidikkammer sowie die Abwesenheit thermischer Interferenzen mit den durchgeführten Färbungsexperimenten. Die AF-Mischmethode wurde erfolgreich zur gleichmäßigen Färbung von großen Krebszellpelletabschnitten eingesetzt, auch bei Verwendung von geringen Flüssigkeitsströmen und kurzen Inkubationszeiten. AF-Mischung könnte die Inkubationszeit der HER2 und CK Biomarker (Cytokeratine) auf Brustkrebszellpellets im Vergleich zum vorhandenen Protokoll der räumlichen Immunmarkierung um 80 % und ihre Konzentration um 66 % reduzieren, während sie ein höheres Signal-zu-Rausch Verhältnis als bei vergleichbaren räumlich aufgelösten Immunoassays mit statischer Inkubation erreichen würde.

Schlüsselwörter

Mikrofluidik, Wechselstromelektrothermik, Akustofluidik, räumliche Proteomik, Immunfluoreszenz, Tumordiagnostik, mikrofluidisches Mischen, diffusionaler Transport, Gewebeanalytik, laminarer Fluss, Wechselstromelektrokinetik, akustische Strömung, Immunhistochemie, Humaner Epidermaler Wachstumsfaktor-Rezeptor 2 (HER2), Panzytokeratin, Mikrofabrikation, Immunfluoreszenz, Bildverarbeitungsanalyse.

Contents

List of Figures

List of Tables

List of Equations

List of Abbreviations

MMC	Multiple myeloma cells
SPR	Surface plasmon resonance
IHC	Immunohistochemistry
ISH	In situ hybridization
R_e	Reynolds number
P_e	Péclet number
D_a	Damköhler number
NdFeB	Neodymium-Iron-Boron
Fe_3O_4	Iron Oxide
ACEO	AC electroosmosis
DEP	Dielectrophoresis
ACET	AC electrothermal flow
EDL	Electrical double layer
IgG	Immunoglobulin G
MPO	Myeloperoxidase
BAW	Bulk acoustic waves
SAW	Surface acoustic waves
IDTs	Interdigital transducers
$LiNbO_3$	Lithium niobate
$LiTaO_3$	Lithium tantalate
F_R	Acoustic radiation force
ϕ	Acoustic contrast factor
F_{drag}	Stokes drag forces
ELISA	Enzyme-linked immunosorbent assay
PSA	Prostate-specific antigen
HER2	Human epidermal growth factor receptor 2
FDA	United States Food and Drug Administration
ITO	Indium tin oxide

k_{on}	Association rate constant
k_d	Dissociation rate constants
B_0	Initial target concentration
D	Diffusion coefficient
r	Particle radius
T	Absolute temperature
η	Solvent viscosity
k	Boltzmann constant
Vpp	Voltage peak to peak
S	Signal
B	Background
MTP	Microfluidic tissue processor system
CK	Cytokeratins
PZT	Piezoelectric transducer
ROI	Region of interest

1 Introduction & state of the art

1.1 Microfluidic applications

1.1.1 Introduction

Microfluidics is a multidisciplinary field that relies on the precise control and manipulation of fluids and particles at the micro and nanoscale, as well as the underlying scientific principles. The field of microfluidics has revolutionized scientific research and has found diverse applications in daily-life and industrial contexts across various fields. These applications were previously unattainable, but have now been made possible through microfluidic technologies. Microfluidics has found widespread use in medical diagnostics and the pharmaceutical industry [1], enabling advancements in diagnostics and drug discovery. Additionally, microfluidics has played a pivotal role in other areas including food safety and production [2,3], cosmetics [4,5], and environmental monitoring of air, water, and soil [6,7]. The success of microfluidics can be attributed to several advantages it offers, including low reagent consumption, miniaturized lab-on-a-chip devices with portability, high-throughput analysis capabilities, and high surface-to-volume ratios, among others [8,9]. The progress in microfluidics has been closely linked to advancements in microfabrication techniques. These techniques, including lithography, etching, hot embossing, injection molding, laser writing, and 3D printing, either used individually or in combination, have facilitated the fabrication of microfluidic devices [10,11]. The development of microfluidics has also been bolstered by advances in processing various materials, including glass, silicon, polymers, metals, hydrogels, and papers, along with the improved understanding of their properties [12].

Over the last decades, microfluidics has emerged as the mainstream technology in the field of biomedical research. It has been widely adopted for the diagnosis of various infectious diseases and viruses, including malaria [13], the hepatitis virus [14], *Salmonella typhimurium infection* [15], sepsis [16], HIV [17], SARS-CoV [18], Dengue virus [19], and *Mycobacterium tuberculosis* infection [20]. Several companies now offer commercialized diagnostic products for diseases with microfluidics as the core technology [21]. Moreover, microfluidics has shown immense potential for personalized medicine, allowing for tailored patient-specific treatments. One example is the use of microfluidic systems to culture tumor biopsy-derived cells from patients for subsequent molecular analysis. For instance, a 3D microfluidic tissue platform has been developed to culture and proliferate primary human-derived multiple myeloma cells (MMC) on a chip, despite the challenges of reproducing the complex *in vivo* bone marrow microenvironment [22]. This advancement enables testing and evaluation of different therapeutics for individual patients in advance of administering them and may shed light on the mechanisms responsible for drug resistance. Similarly, microfluidic devices have been utilized for producing patient-derived organoids on-a-chip, facilitating chemotherapy drug screening, and allowing for accurate *ex vivo* assessment and optimization of patient-specific drug treatments [23,24].

In addition to the applications mentioned earlier, microfluidics has opened up new avenues for drug synthesis and production [25,26], as well as high-throughput drug screening [27,28]. Many companies now utilize microfluidic technologies for identifying biomarker targets of interest and assessing corresponding drug candidates through preclinical studies on cells, tissues, and organoids [29]. Furthermore, microfluidic technologies allow for precise and controlled application of experimental conditions that are not achievable using macroscopic devices, opening up new possibilities and enabling successful studies of cellular biology at the single to multi-cellular levels. This includes large-scale and parallel measurements of cell motility [30], quantitative analysis of cancerous cell-cell interactions [31], natural killer cell-target cell interactions [32], investigation of T white blood immune cell activation [33], studying the binding energy landscape of transcription factors [34], and multiplex analysis of single cell protein secretion [35,36].

1.1.2 Surface-based assays

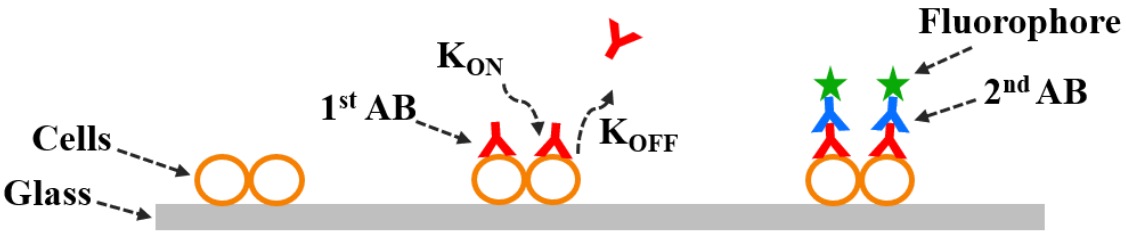

Figure 1.1 Schematic for a surface-based assay. *Cells mounted on a glass substrate, and primary antibody (1st AB) and secondary (2nd AB) antibody tagged with a fluorophore are used for the detection of the marker of interest on the cells. Reaction kinetics of a bioreagents is determined by K_{on} (association constant) and K_{off} (dissociation constant).*

The application of microfluidics for surface-based assays has gained a lot of interest in the last decades, where the target sample (proteins or DNA, cells, tissues, etc.) is immobilized on a surface and incubated inside the microfluidic chamber for subsequent analysis. Figure 1.1 shows an example of a surface-based assay where target cells are mounted on a glass substrate. Subsequently, an indirect immune-fluorescence assay is conducted where detection antibody molecules (1st AB followed by 2nd AB tagged with a fluorophore) are used for the selective detection of target molecules on the cells. Several immobilization surfaces can be used such as glass [37], silicon [38], polymers [39,40], metals [41,42], hydrogels [43], and papers [44,45]. Similarly, a wide variety of immobilization chemistries were developed for the successful mounting of target samples and surface blocking. This includes one or a combination of the techniques relying on electrostatic ionic interactions [46], hydrophobic interactions [47], bio-affinity adsorption [48,49], and covalent chemistry [50,51].

Moreover, several detection methods for the microfluidic surface-based assays were developed, including label and label-free detections, for scientific and commercial purposes. This includes surface plasmon resonance [52], electrochemistry [53], Raman spectroscopy [42], and mass-sensitive techniques, such as those used in deflecting cantilevers [54] and surface acoustic wave devices [55]. Commercial products relying on surface-based detection techniques including surface plasmon resonance (SPR), electrochemical, Raman- and mass-sensitive detection are now available as shown in Table 1-1.

Table 1-1 Commercial products relying on surface-based detection techniques

Device	Detection method	Company	Reference
Biacore	SPR	Cytiva	[56]
Sierra	SPR	Bruker	[57]
Electrochemical sensor	Electrochemical	Micruxfluidic	[58]
Electrochemical sensor kit	Electrochemical	Dolomite Microfluidics	[59]
DXR3 Raman series	Raman spectroscopy	Thermo Fisher Scientific	[60]
PeakSeeker Pro	Raman spectroscopy	Agiltron	[61]
QSense	Mass-sensitive	Biolinscientific	[62]

In addition to that, the application of microfluidics in the field of spatial molecular profiling of tumor tissues has gained a lot of interest in the last years [63–66], particularly with the increasing focus on personalized medicine and targeted therapy. In this approach, a large dissected and thin tissue section of the tumor is mounted on a substrate slide (e.g. a glass slide) and incubated inside a microfluidic chamber for subsequent immunostaining and analysis. After that, different specific immune detection reagents such as antibodies, or DNA oligos can be used to immune-label the marker(s) of interest, followed by subsequent visualization with microscopic techniques such as fluorescence or chromogenic bright-field microscopy. This allows for detecting both the presence and the level of expression of the markers. The two most common techniques for tissue diagnostics are immunohistochemistry (IHC) and *in situ* hybridization (ISH) [67,68], wherein the former the expression of certain markers (proteins) in a cell population can be detected (proteomics), and in the latter, a labeled RNA or DNA probe can be used for studying the gene expression (transcriptomics) in the tumor cellular environment.

Indeed, in recent years, several companies have developed and optimized automatic immune staining systems for microfluidic-based spatial molecular profiling of tumor tissues or cells. These systems allow for immune-staining of the target sample with multiple markers per cycle, and in some cases, also provide imaging capabilities for subsequent analysis. These commercial products have enabled a high-throughput analysis, are cost-effective, and yield automated analysis of tumor tissues, leading to more accurate proteomic and transcriptomic analysis for various fields, including scientific research, medical diagnostics, and drug discovery. Some examples of commercial products in this area are shown in Table 1-2.

Table 1-2 Commercial automatic Immune staining systems

Device	Company	Reference
PhenoCycler (Coedx)	Akoya Biosciences	[69]
MACSima	Miltenyi Biotec	[70]
GeoMX DSP	NanoString Technologies	[71]
Hyperion	Standard BioTools	[72]
COMET	Lunaphore technologies	[73]

1.1.3 Distributed channel network chips

Several microfluidic applications have been developed sharing the common feature of a multi-inlet / multi-outlet microfluidic chip design, with different names given such as the distributed channel network chip, the Christmas tree design chip, or the microfluidic concentration gradient generator. These designs allow for the precise manipulation of fluids, creating complex flow patterns and enabling various functionalities. The Christmas tree design microfluidic chip resembles the shape of a Christmas tree, with a single main channel serving as the trunk and multiple branches, emerging from that single main channel and serving as inlets or outlets. Figure 1.2 shows an example of the core functional part of the distributed channel network chip with a multi-inlet and multi-outlet design. Usually, one or several common inlets are used to feed these multi-inlet ports with one or several fluids in parallel, and outlet port/s are used for the common fluid withdrawal. Here, we show an example by numerical simulation (using COMSOL Multiphysics 6.1) of how this multi-inlet / multi-outlet design can be used for creating a microfluidic concentration gradient inside the chamber without any interior boundary walls.

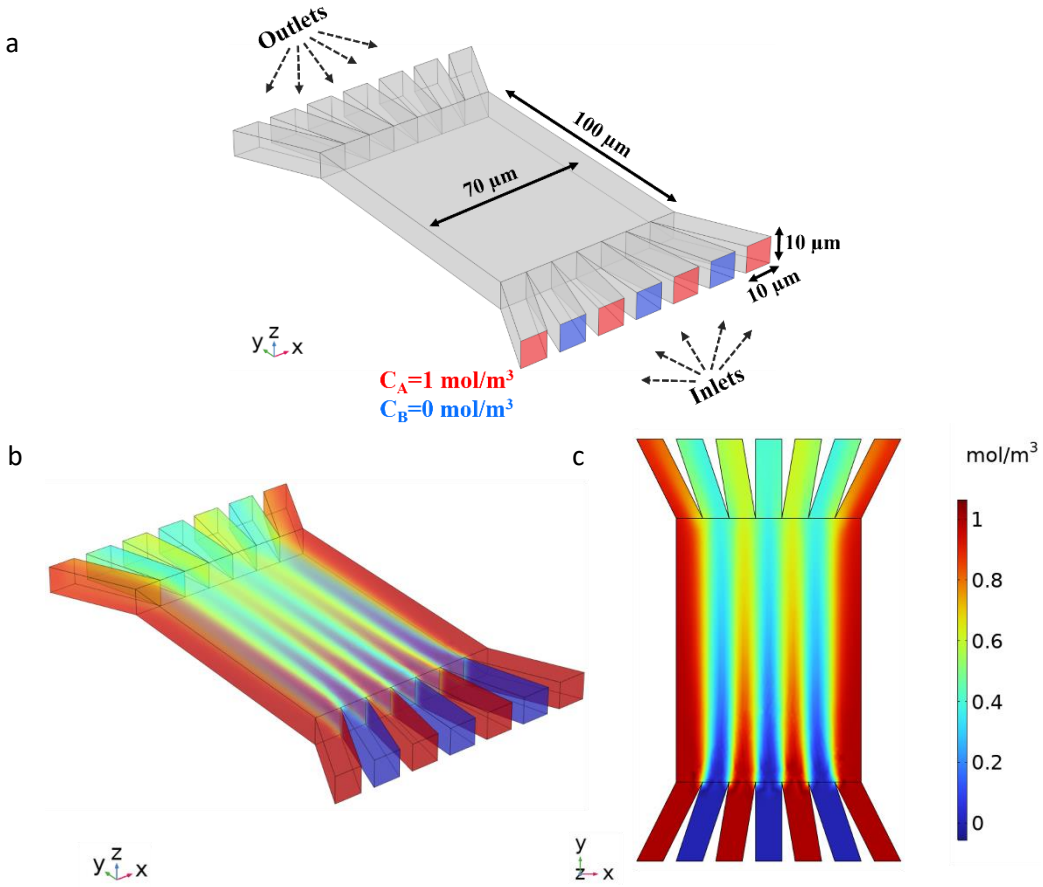

Figure 1.2 Distributed channel network chip-based concentration gradients. *(a) Microfluidic chip with a multi-inlet / multi-outlet design, each with an in-/output channel size of 10×10 µm², with each second inlet begin supplied with a fluid concentration of 1 mol/m³ and the other inlets with 0 mol/m³. The inlet flow rate is 7.5×10⁻¹⁵ m³/s. (b and c) Tilted-angle and top view, respectively, of the concentration (mol/m³) profile of the chip, showing the diffusion-based mixing profile throughout the chip.*

As shown in Figure 1.2a, different fluid concentrations of 1 or 0 mol/m^3 are supplied alternatively between the neighboring inlets, and the fluid flow rate is 7.5×10^{-15} m^3/s. Laminar fluid flow and the transport of diluted species modules were used for the simulation. Figure 1.2b and Figure 1.2c show a tilted angle and top views, respectively, of the microfluidic chip concentration profiles. It is clear how the concentration profile, just after the inlet, shows a sharp alternation between the high and low concentrations, in front of the high and low concentration inlets, respectively. Later, along the chip length and closer to the outlet ports, the concentration profile shows mixing between the parallel running fluid streams.

This design has been investigated and adapted by several groups for creating microfluidic concentration gradients along the width of the chamber and orthogonal to the fluid flow direction [74–76]. These concentration gradients have been successfully used in various studies, including chemotaxis studies to create a chemical gradient delivered to incubated cells [77], optimization of differentiation and proliferation of neural stem cells [78], gene expression and phenotypic changes analysis of *Saccharomyces cerevisiae* yeast under pheromone gradients [79] and investigating the effect of surface protein gradients on the cellular polarity and axon guidance of rat hippocampal neurons [80]. In these systems, the generated concentration gradients are dependent on several factors, including the fluid flow rate, the fluid viscosity, and the mass-transport of solute species. Additionally, other factors such as microfluidic chamber dimensions and type of fluid-controlling devices, which can have a temporal resolution affecting the minimum response time for fluid flow control, need to be considered [81].

Using the same concept of concentration gradients but for tissue diagnostics, a microfluidic immunostaining device was utilized to incubate linearly graded concentrations of antibodies on a reference tissue sample [63]. This approach was developed for the quality assurance and the standardization of immunohistochemistry techniques among different laboratories and hospitals, aiming to standardize the staining intensity and verifying the quality of detection reagents. In this example, the microfluidic system consisted of nine physically separated microfluidic channels that were sealed against a tissue sample. On the other hand, there have been several reports [64,65,68,82–86] that have adopted the distribution channel network design for building a tissue diagnostic platform. Here, the chip design includes a large microfluidic chamber without any physically separated channels and was utilized to distribute the bioreagents uniformly above the thin tissue incubated inside the microfluidic system. This design is used to ultimately ensure that all relevant antigen epitopes on the tissue are exposed equally to the detection reagents, enhancing signal contrast and leading to consistent results while avoiding false or biased diagnosis or prognosis.

1.2 Physics of microfluidic flow

1.2.1 Introduction

The fundamental physics and forces governing fluid flow and fluid-solid interaction can exhibit significant and rapid changes when the system size scale is reduced, as in the case of microfluidic

devices. A thorough understanding of fluid flow behavior in scaled-down systems is crucial for the accurate design and analysis of microfluidic devices. At a small scale, a wide range of physical phenomena can profoundly impact fluid flow. To aid in understanding these phenomena and their interplay within microfluidic systems, scientists have devised several dimensionless numbers as valuable guides for the understanding of physical phenomena. These dimensionless numbers include the Reynold number, Péclet number, Capillary number, Damköhler number, and others. In the following sections, we will delve into these dimensionless numbers and their associated physical phenomena, which are vital for microfluidic systems and, notably, for biochemical reactions and surface-based assays.

1.2.2 Reynolds number (Re)

The Reynolds number (R_e) describes the ratio between the inertial momentum forces to the viscous shear forces per unit volume of the fluid [87]. It is described by equation 1.1,

$$R_e = \frac{Inertial\ forces}{Viscous\ forces} = \frac{\rho U^2/L}{\mu U/L^2} = \frac{\rho UL}{\mu} \qquad 1.1$$

where ρ represents the fluid density (kg/m^3), U is the fluid velocity, L is the characteristic length dimensions (or hydraulic diameter in the case of a pipe of the duct), and μ is the fluid dynamic viscosity (Pa.s). At a small Reynolds number R_e values, viscous forces dominate, effectively keeping the fluid layers aligned, resulting in a laminar fluid flow regime. In contrast, at higher $R_e$values, inertial forces become more significant, leading to turbulent fluid flow. One of the key differences between laminar and turbulent fluid flow regimes is that in laminar flow, fluid particles move along straight paths parallel to the fluid flow direction, while in turbulent flow, fluid elements exhibit random and chaotic motion, leading to extensive fluid mixing. Microfluidic systems typically operate in the laminar flow regime due to their slow fluid velocities and small characteristic dimensions. This laminar flow is crucial as it affects the translocation of microparticles or reagents dispersed in a fluidic chamber and their interaction with their targets in the surrounding volume.

Figure 1.3 shows by numerical simulation an example of the implication of the low Reynolds number observed in microfluidic systems. The system consists of a common running channel with two inlets and two outlets, each with a size of 10×10 µm^2. One inlet is being supplied with a solution of 1 mol/m^3 concentration and the other inlet with 0 mol/m^3 (e.g., deionized (DI) water), both with an inlet flow rate of 7.5×10^{-15} m^3/s. The laminar fluid flow and transport of diluted species modules were used for the simulation. Figure 1.3b shows the concentration profile of the full system, with the limited mixing between the two side-by-side running fluids due to the domination of the viscous forces at low Reynold numbers and the limited mass-transport of the diluted species. As detailed later in this chapter for the passive micromixers, here it is worth noting that mixing is enhanced downstream of the channel, as seen by the cross-sectional concentration profiles. This means that longer channels can be used to achieve mixing between the running fluids but at the cost of the device size and microfluidic resistance. Figure 1.3c shows the concentration profile (top view) of the running fluids

but at different diffusion coefficients of the diluted molecule. As explained later for the microfluidic mixing technologies, one can see clearly that even with the same microfluidic chamber size, fluid flow rate, and same concentration, higher mixing within the running fluids is achieved for molecules with higher diffusion coefficients. This can be of vital importance for designing microfluidic systems used for biochemical applications and micro-reactors.

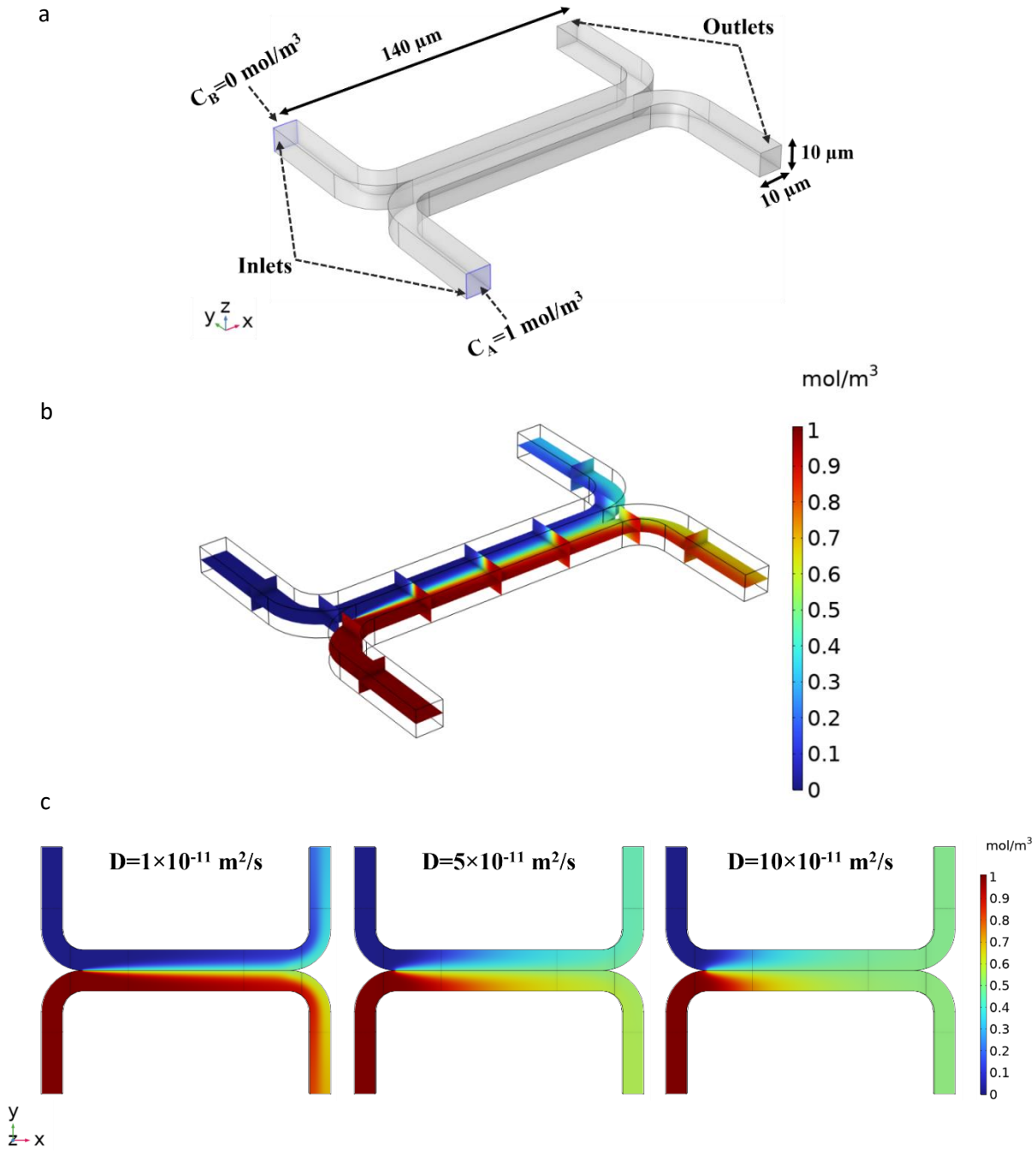

Figure 1.3 Two-inlets channel laminar flow. *(a) 2 channels (10×10 µm^2) with different inlet concentrations (C_A & C_B), merging in one channel then diverging into individual outlets, with inlet flow rate of 7.5×10^{-15} m^3/s. (b) The concentration (mol/m^3) profile showing the limited mixing between the two inlet concentrations. (c) The concentration profile (top view) at different diffusion coefficients of the diluted molecule (1 to 10×10^{-11} m^2/s)*

1.2.3 Péclet number

The Péclet number (P_e) measure the relative importance of the advective to diffusive transport [88,89], as shown in equation 1.2,

$$P_e = \frac{Advective\ transport}{Diffusive\ transport} = \frac{UC_0}{DC_0\ /\ L} = \frac{UL}{D} \qquad 1.2$$

where C_0 is the concentration of a species in the microfluidic chamber, and D is the species diffusion coefficient. Similar to the Reynolds number, microfluidic systems often operate with small fluid velocities and dimensions, resulting in low Péclet numbers. This implies that diffusive flux of species predominates, with species moving from regions of high to low concentration. In contrast, for large P_e values, advective flux becomes dominant. For a microchannel with a length of L=100 µm and diffusion coefficient of 10^{-9} m^2/s of molecules running through it and a flow speed of 1 mm/sec, the pellet number would be 1000. This means the channel length has to be 1000 times the channel height (10 cm length!) for two streams to mix efficiently. With bigger molecules and a slower diffusion coefficient, the channel length can be 10 and 100 times longer. An everyday example of advective and diffusive transport can be observed when adding sugar to a cup of tea. If a spoon is used to stir the tea, it causes bulk and vigorous advective motion, resulting in a homogeneous dispersion of sugar molecules throughout the cup. However, if sugar is added without stirring, the diffusive transport of sugar molecules becomes the dominant mechanism for their dispersion. It's worth mentioning that the diffusion coefficient (D) is inversely proportional to the size of the species molecules, as discussed in more detail later.

The relationship between species size and diffusion coefficient implies that larger species have smaller diffusion coefficients, resulting in longer times required for species to travel within microfluidic systems and interact with each other or their targets. This limitation is further reinforced by the laminar flow regime achieved at low Reynolds numbers, where high viscous forces ensure that fluid elements move in straight, parallel lines without perpendicular mixing to the fluid flow direction. Consequently, the predominance of diffusive transport in microfluidic systems has sparked significant research interest in developing various microfluidic mixing techniques, as discussed in detail later.

1.2.4 Damköhler number

The Damköhler number (D_a) can be utilized to establish a correlation between the reaction rate and the species diffusion rate in chemical reactions within microfluidic systems [90,91]. This is applicable to chemical reactions occurring within the volume of the microfluidic device or at a microfluidic/solid interface, such as in surface-based assays. An example of the latter is when surface-immobilized or mounted targets, such as cells, tissues, or affinity reagents, inside a microfluidic system, undergo a chemical reaction with the incubated detection reagents, such as antibodies or DNA

$$D_a = \frac{Reaction\ rate}{Diffusion\ rate} = \frac{k_{on} B_0 h}{D} \qquad 1.3$$

Equation 1.3 shows the Damköhler number (Da), where k_{on} is the association rate constant of the reacting species to their target, B_0 is the concentration of the surface target (e.g. the surface area density of the reacting target epitopes), and h is the microfluidic chamber height (or lateral dimensions).

When the Damköhler number (D_a) has small values, and the diffusion rate of the detection species (e.g. smaller molecules) is faster than the reaction rate. In such cases, the system is reaction-limited, meaning that increasing the mass-flux of the reagents to the target surface would not significantly enhance the chemical reaction. On the other hand, when the D_a value is large, the reaction rate is faster than the diffusion rate, and the system is limited by the mass transport of the detection reagents to the target surface [89]. Moreover, microfluidic systems can be designed with different chamber heights (h), and the Damköhler number scales accordingly. This means that systems with larger chamber heights are more diffusion-limited. Therefore, the Damköhler number can serve as a useful parameter to assess whether a given microfluidic system used for chemical reactions would benefit from microfluidic mixing techniques or not.

Finally, we believe that it is highly important to consider two subsequent and distinct steps for the surface-based assays with different mass-transport profiles of the detection reagents. The first step is the dispensing of the detection reagents over the reacting surface at a certain flow rate, which results in a strong concentration flux of the reagents to the target surface. This step is characterized by advective transport, where the flow rate plays a crucial role in determining the concentration of the detection reagents on the target surface. The kinetics of association and dissociation of the reagents also come into play during this step. The second step is the static incubation, where the chamber is filled and the reagents and the target surface undergo the chemical reaction. In this step, the reaction rate is determined by the interplay between the kinetics rates (association and dissociation of reagents) and the diffusion rate, as discussed before. This step is characterized by diffusive transport, where the concentration gradients drive the diffusion of the detection reagents toward the target surface. It is important to differentiate between these two steps during experimental analysis or numerical simulation modeling of microfluidic surface-based assays, as they have different mass-transport profiles and can significantly impact the overall performance of the assay. Proper consideration of these distinct steps can lead to a more accurate understanding of the assay dynamics and help in optimizing the assay performance in microfluidic systems.

1.3 Microfluidic mixing techniques

1.3.1 Introduction

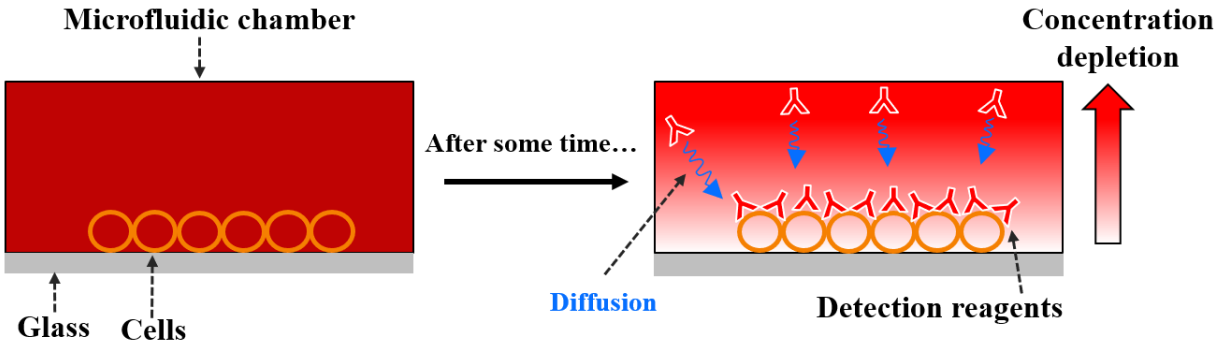

Figure 1.4 Schematic of formation of concentration depletion region. *Cells are mounted on a glass substrate and incubated inside a microfluidic chamber filled with the detection reagents. After some incubation time, the detection reagents are consumed and a concentration depletion region is formed with less reagents concentration close to the target samples (cells) on the glass slide.*

Due to the prevalent laminar fluid flow in microfluidic systems and the dominance of viscous forces over inertial forces, which results in the absence of fluid turbulence, surface-based assays can exhibit prolonged assay times or weak detection signals. Figure 1.4 presents a schematic of a microfluidic immunoassay, wherein target cells are incubated within a microfluidic chamber alongside detection reagents. Following an incubation period, the detection reagents are depleted in the vicinity of the target surface as a result of binding to the epitopes located close to the surface. Consequently, a region of low abundance of detection reagents, characterized by concentration depletion, forms above the reacting surface, restricting the binding reaction to the diffusion of the far-away incubated reagents.

It is crucial to acknowledge that the distance that detection species need to traverse to react with the surface target is not solely limited to the height of the microfluidic chamber. For instance, the reacting surface may be located at the center of the chamber, while the unused detection reagents are positioned far away, at the sides of the microfluidic chamber, at a distance of a few millimeters or centimeters. Considering the typical range of diffusion coefficients of biochemical reagents, which falls within 10^{-11} to 10^{-12} m^2/s [92,93], this can result in significant time additions to the assay duration, spanning hours or even days, to allow adequate time for the reagents to diffuse and react with the target surface. Furthermore, it would be advantageous for microfluidic systems to enable the utilization of lower concentrations of chemical reagents for cost-effective analysis. However, lower concentrations would also mean reduced availability of detection reagents that can participate in the chemical reaction and diffuse to the target surface, further complicating the assay process.

This represents one of the primary challenges in microfluidic systems, and researchers have extensively investigated various microfluidic mixing techniques [94,95]. Microfluidic mixing can significantly improve the contact rate between different reacting components, thereby enhancing the throughput of microfluidic systems, enabling the realization of smaller lab-on-a-chip systems, and reducing the concentration of reagents required. Microfluidic mixing techniques can be broadly

categorized based on their basic working concepts into passive mixers and active mixers, each of which will be elucidated in the following sections, accompanied by examples for each class.

1.3.2 Passive mixing

Passive mixing primarily relies on the flow provided by the pumping system and the fluid behavior, often taking advantage of specialized channel designs and geometries and/or by increasing the contact area and time [94,96]. The former can induce chaotic advection effects, while the latter can augment the surface contact area and time between fluid layers, both resulting in fluid mixing. One of the advantages of passive mixing systems is that they do not require external energy sources, thus reducing the system power requirements. Additionally, passive mixing systems do not include any moving parts, making them reliable for various applications.

Several types of passive mixing devices have been proposed including transverse diffusive mixing, lamination mixing, hydrodynamic focusing-based mixing, and embedded barriers or channels [94–97]. In transverse diffusive mixing for example, two channels can be designed in a T- or Y-shape [98–100] where the fluids are injected from the two inlets and then grouped in one channel as shown before in Figure 1.3. In the common flow-through channel, the fluids are mixed mainly by diffusion. The mixing can be enhanced by increasing the fluid flow rate to induce strong inertial forces, and by extending the length of the common channel to allow enough transversal mixing. The same concept can be further extended and enhanced by using lamination techniques [101,102]. For example, the inlet fluids can be split and then grouped into several small streams. This would then increase the contact area between the two fluids thus enhancing the mixing efficiency. If one would also split and re-combine the fluid streams several times, while manipulating the channel orientation in 3D [102,103], this can produce a stacking of multiple laminates with multiple interfacial and diffusion areas.

Another passive mixing technique is the hydrodynamic flow focusing [104–106], where a main central and two side channels are grouped into one main channel. The fluid from the middle channel is then running while being enveloped by the two sheath fluids from the side channels. The interplay between the fluid flow rates of the three channels can then define the mixing efficiency and the fluids mixing time. Finally, adding some geometrical surface structures to the microfluidic channels [107–109] (e.g. wells, ridges, or barriers) can cause disturbance to the fluid flow and the concentration profile, leading to stretching and folding of fluidic layers and thus mixing. Figure 1.5 shows an example by numerical simulation of a microfluidic passive mixer and how it can affect the concentration profile in the chamber. Figure 1.5a and Figure 1.5c show the microfluidic chamber design explained before (in Figure 1.3), except, in Figure 1.5c, geometrical structures in the form of tilted ridges were added at the bottom of the chamber. The laminar fluid flow and the transport of diluted species modules were used in the simulation (using COMSOL Multiphysics 6.1). Figure 1.5b and Figure 1.5c show the corresponding concentration profiles of the chamber, without and with the tilted ridges, respectively. As shown, without the ridges, the fluids run through the channel with a limited mixing due to the absence of any fluid turbulence and domination of viscous forces. However, adding ridges at the bottom of the chamber would induce several events of the fluidic layers folding and stretching, leading

to higher mixing within the fluid channel. This can be seen clearly when comparing the concentration profiles of the two designs close to the outlet ports.

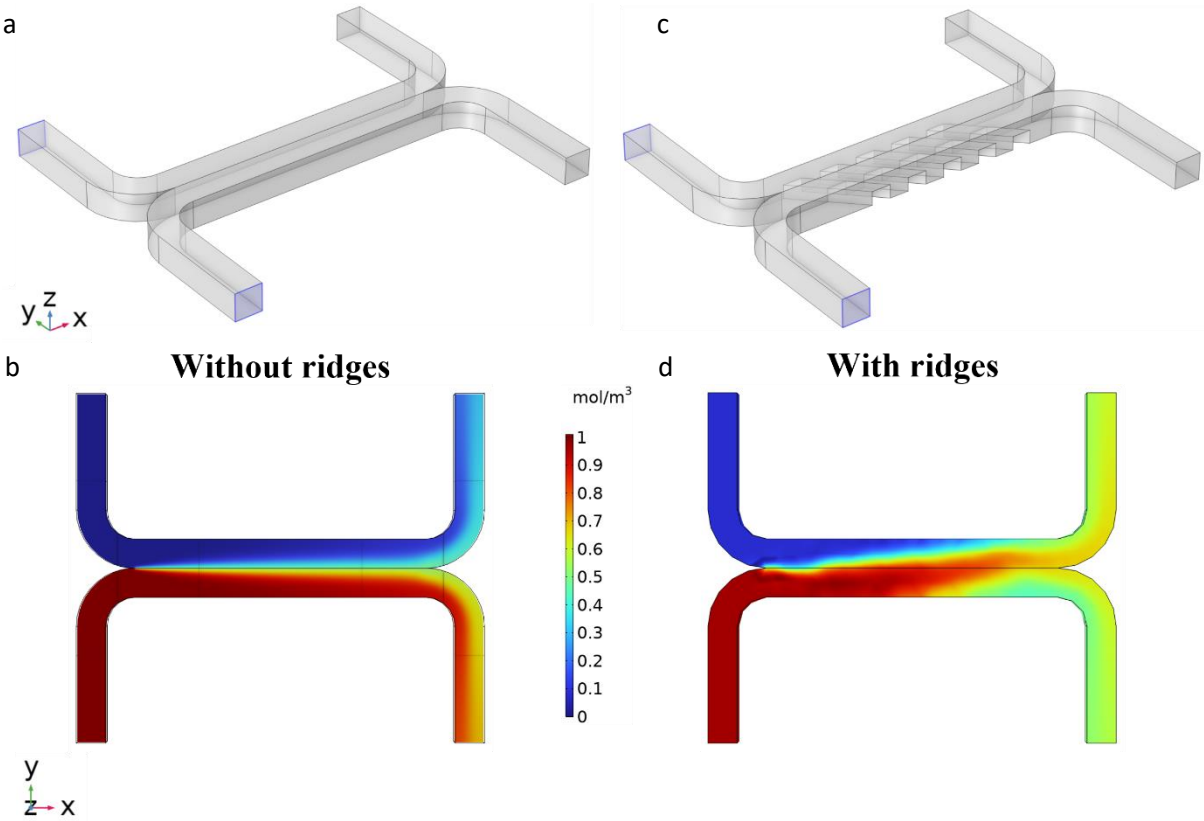

Figure 1.5 Passive micromixer. *(a) and (c) Microfluidic chamber with a 2-inlets/2-outlets design shown before in Figure 1.3, without and with tilted ridges located at the bottom of the chamber, respectively. The ridges (5 µm wide and 5 µm high, and with 5 µm gap between ridges) span across the channel width and are titled with an angle of 45°. The same flow rate (7.5×10^{-15} m^3/s) and the same concentrations at the inlets with diffusion coefficient of 1×10^{-11} m^2/s were used. (b) and (d) Concentration profile (top view) of the microfluidic designs, without and with the tilted ridges, respectively.*

Passive mixing techniques can be applied independently or in combination with other functionalities of the same microfluidic device to achieve homogeneous mixing. However, these techniques pose certain challenges when it comes to integration into different applications, particularly for surface-based assays. Some of the common challenges associated with passive micromixers include the need for microfluidic channel design modification, which requires microfabrication processes, and some techniques, such as flow splitting-recombining or the use of a 3D geometry with modified channel orientation can lead to complicated microfabrication procedures. Furthermore, some passive micro-mixing techniques may require long channels for complete mixing, which adds additional fluidic resistance to the channel and can hinder system down-scaling and portability. Techniques that rely on lowering the flow rate to increase the contact time between fluid layers, on the other hand, may decrease the throughput of microfluidic testing.

Moreover, in biomedical applications that require microscopic imaging to analyze the incubated sample, modifications such as channel ridges or barriers can hinder imaging accessibility throughout the system. Another challenge is that passive mixers with surface-machined structures, such as grooves or slanted wells, may experience high mechanical stress at these structures associated with

high pumping pressures. As a result, passive mixers relying on this technology need to be designed with sufficient device thickness to avoid failure or leakage at these structures.

1.3.3 Active mixing

Active mixers in microfluidic systems require an additional external energy source to induce chaotic advection and increase the contact area and time of the fluidic layers. Several types of active mixers have been reported, which rely on different energy sources such as magnetic fields, electric fields, sound fields, and pressure fields [94,95]. For example, magnetic fields can be used to manipulate magnetic particles or ferrofluids within a microfluidic channel, thus inducing mixing. Electric fields can be used to induce the electrokinetic or dielectrophoretic motion of charged particles or cells, leading to mixing. Sound fields, such as ultrasonic waves, can create acoustic microstreaming effects that cause fluid mixing. Pressure fields, such as micro-pumps or micro-valves, can be used to generate flow disturbances and induce mixing.

Active mixers can offer precise control over mixing dynamics and can be more efficient in achieving rapid and homogeneous mixing compared to passive mixers. However, they evidently require external energy sources, which may increase the complexity and power requirements of the microfluidic system. Careful consideration of the energy source, its associated complications, and the specific requirements of the assay or application is essential when choosing and implementing active mixing techniques in microfluidic systems.

1.3.3.1 Magnetic field-based mixing

Magnetic field-based micromixers usually rely on the manipulation of either magnetic micro-size particles or ferrofluids or magnetic micro-actuators using an external magnet. The magnetic micromixer systems have the advantage of remote non-invasive control from the outside of the microfluidic device. Moreover, the surface of magnetic particles can be used for biochemical functionalization for subsequent immunoassays [110] or microfluidic separation purposes (magnetophoresis) [111].

Magnetic microbeads can be dispensed inside microfluidic channels forming aggregates and bead chains which can be controlled externally by a strong magnet. With the simple rotation of the external magnet, the bead aggregates respond to the magnetic field by rotating while dragging and stirring the surrounding fluid leading to mixing. Ferromagnetic particles (3 µm) have been used in a microfluidic system and two Neodymium-Iron-Boron magnets (NdFeB) were attached to a rotor and used to rotate the formed magnetic rods or aggregates. A mixing efficiency of 96% was achieved in a short distance between two side-by-side running channels and with higher flow rates of 1.2–4.8 mm/s [112]. Larger size particles (7 µm) have been tested and were found to not rotate efficiently in the mixing chamber and some particles were trapped in the particle inlet channel, which can jeopardize the device's performance. Similarly, a suspension of magnetic particles was injected in a Y-shaped microchannel with a cross-section of 200× 200 $\mu m^{2,}$ and two soft iron plates were added close to the channel to

focus the external magnetic flux. A mixing efficiency of 95% was achieved over a mixing length of 400 µm and at flow rates of 5 mm/s [113]. Superparamagnetic iron-oxide microparticles (10 µm) were used to speed up a bioluminescent assay for the detection of CTX-2 (a marker for calcified cartilage degradation in body joints). The magnetic actuation of the microparticles induced a vortical flow mixing in the microfluidic chamber and lead to increasing the assay kinetics, which indeed reduces the time to sensor readout from 23 to 12.5 min [114].

Ferrofluids are a stable colloidal suspension of single-domain magnetic particles within the size range of 5-20 nm and dispersed in a fluid carrier that can be polar or nonpolar [115]. One major advantage of ferrofluids is they can re-assume a fluidic nature even after subjecting them to a strong magnetic field. A permanent magnet was mounted below a Y-shape microchannel and a ferro-nanofluid (Fe_3O_4 nanoparticles suspended in water) and water were injected at different flow rates. The presence of the magnet lead to the relatively uniform distribution of the ferro-nanofluid in the chamber and achieved a 90% mixing efficiency while the diffusion-limited flow was below 15% [116]. Another group achieved a 95% mixing efficiency within 2 sec between a water-based ferrofluid and water using an external electromagnet. After the application of the magnetic field, the ferrofluid shows significant uniform expansion towards the water [117]. However, the densely concentrated ferrofluids can hinder the optical readout for microfluidic applications, and the effects of ferrofluids on chemical reactions are not fully understood [118].

Inspired by the biological flagella and their hair-like structure involved in the locomotion of the cells and their ability to generate fluid flow in low at low Reynolds number [119], research groups have investigated the creation of artificial magnetic cilia and flagella and their usage for microfluidic pumping [120] and mixing [121]. Artificial cilia are slim, hair-like, flexible filaments that can be grafted on the microfluidic chamber wall and can be actuated externally. The artificial cilia can be fabricated by several methods [122], with the most common method consisting of simply mixing magnetic microparticles (e.g. carbonyl iron powder) with a curable liquid carrier such as PDMS. The mixture can be then poured on a micromachined or lithographically prepared mold and then cured, leading to the formation of the magnetic artificial cilia pillars. For example, neodymium-iron-boron magnetic particles (5 µm) were mixed with PDMS and cured in an acrylic mold that resulted in 50 µm diameter and 300 µm high artificial cilia attached at the wall of the microfluidic chamber [121]. The artificial cilia were actuated with an external magnetic coil system and the cilia structures were moved in different trajectory patterns leading to 85% fluid mixing within 5 sec. Similarly, the same magnetic particles were mixed with PDMS and cured inside micro-drilled holes with 50 µm diameter and 400 µm height [123]. Different beating motions of the cilia were investigated with a range of traveled transverse distance of 85 to 108 µm along the microchannel width, resulting in a mixing efficiency of up to 90%. Moreover, researchers have reported the implementation of magnetic artificial cilia to induce fluid flow and mixing and enhanced the microalgae growth by ten times [124].

To the best of our knowledge, the integration of magnetic-based mixers, such as ferrofluids, magnetic beads, and artificial cilia, for surface-based immunoassays has been relatively limited in the literature. One challenge is the need for a magnet actuator in close proximity to the microfluidic system, which can limit the scalability and portability of the device. This may require additional space and

considerations for the magnet actuator, which can be a limitation in miniaturized systems or point-of-care applications. Moreover, some magnetic mixers may still require microfabrication steps, which can add time and cost to the implementation process. Microfabrication techniques, such as lithography or etching, may be needed to pattern channels or structures for efficient manipulation of magnetic particles or ferrofluids, which may not be feasible or cost-effective for all applications.

Additionally, the presence of magnetic beads or the usage of non-transparent ferrofluids can limit optical imaging accessibility in the microfluidic system. This can hinder the analysis of the assay components or interfere with the biochemical reactions being studied [125], which may be a limitation in certain assays or applications where optical imaging is critical for analysis. It is important to carefully consider the specific requirements of the assay or application when choosing to implement magnetic-based mixers in microfluidic systems, taking into account factors such as scalability, portability, microfabrication steps, and imaging accessibility. Further research and development in this area may be needed to overcome these limitations and enable wider utilization of magnetic-based mixers in microfluidic systems for surface-based immunoassays.

1.3.3.2 Electrical field-based mixing: use of AC electrokinetics

The integration of microelectrode structures with microfluidic systems has become a promising and innovative approach in the field of micro and nanofabrication. This integration has enabled various microfluidic applications, such as fluid mixing, pumping, particle concentration, and trapping, as well as electrochemical and electromechanical analysis. The miniaturized lab-on-a-chip systems that result from these advancements have found practical applications in various fields. One application of microelectrode-integrated microfluidic systems is the monitoring of pH (potential of hydrogen) levels inside microfluidic devices. The pH level can affect the functions of biological cells [126], and real-time monitoring of pH can be crucial in many biological and biomedical applications. In addition, microelectrode-integrated microfluidic systems have been used for *in situ* and continuous biosensing of biomarkers in organ-on-a-chip devices. This allows for real-time monitoring of biomarkers, which can provide valuable information for drug testing, disease diagnosis, and personalized medicine [127].

Electrochemical sensing of enzymatic activity and glucose concentration is another application of microelectrode-integrated microfluidic systems [128]. These systems can provide precise and sensitive measurements of enzymatic activity or glucose concentration in small volumes of samples, which is useful in clinical diagnostics, biomedical research, and point-of-care testing. Microscale chemical synthesis [129] and environmental monitoring [130] have been also facilitated by microelectrode-integrated microfluidic systems. These systems can enable, in the former, the precise control of reaction parameters such as temperature and concentration, and in the latter, rapid and sensitive detection of environmental pollutants or contaminants.

These applications frequently rely on the electrical actuation or/and the electrical monitoring of the integrated electrodes. At the same time, different technologies were developed, using the same concept of electrically actuating the embedded electrodes, to induce several forms of fluid and particle manipulation at the micro and nanoscale. These applications have been collectively investigated and

optimized by numerous research groups under the generic name of AC electrokinetics [131–133]. In general, three common AC electrokinetic techniques that are extensively investigated and used for microfluidic applications are AC electroosmosis (ACEO), Dielectrophoresis (DEP), and AC electrothermal flow (ACET), each with its own physical concept and working mechanism.

1.3.3.2.A AC electroosmosis (ACEO)

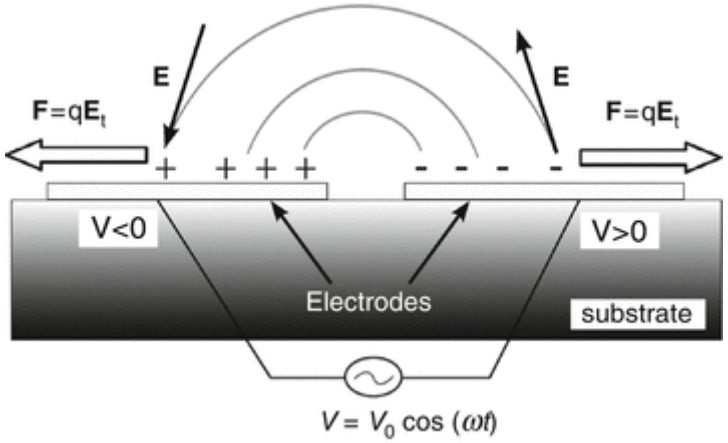

Figure 1.6 The concept of AC electroosmosis. *Charges accumulated in the electrical double layer above the electrodes biased with an AC signal, will migrate in response to the tangential component of the electric field. This gives rise to a surface fluid velocity and a corresponding bulk motion of the fluid due to viscosity. This figure was adapted [1] for dissertation writing purposes.*

When a relatively low-frequency signal is applied to co-planar electrodes that are in contact with an electrolyte, it induces charges or ions to accumulate at the electrolyte-electrode interface, forming what is known as the electrical double layer (EDL). These induced charges have a sign opposite to that of the electrode charge. When the frequency of the applied electric field and the medium charge relaxation time are in a comparable range, the electrode surface is not fully screened by the counter-ions [134], and the inner portions of the double layer on the electrodes charge more rapidly than the outer regions. As shown in Figure 1.6, this uneven charging of the electrical double layer leads to a tangential force due to the electric field, also known as electrostatic force, acting from the screened region (close to the electrodes gap) towards the unscreened outer regions, since the fluid resistance close to the co-planar electrodes gap is less than elsewhere and the electric field intensity is maximum [135–137]. This will lead to the charges` migration, and due to the viscosity and cohesive nature of water molecules in the electrolyte [132], this will result in a fluidic motion in the surrounding bulk fluid. The changes in the electric field direction and the polarities of the induced charges with the AC electric field are simultaneous, and therefore the fluid flow direction is independent of the sign of the applied voltage. This means that regardless of the polarity of the applied voltage, fluid flow will occur in a consistent direction and the time-averaged force will be non-zero.

AC electroosmosis has been integrated for several microfluidic applications such as fluid pumping by breaking the symmetry of the microelectrode design [138], or by creating a 3D geometry for enhanced Ac electroosmosis pumping [139] or similarly using a 3D stepped electrode array [140]. This has been also achieved by using a traveling wave electric potential where a phase shift of 90° is imposed between the neighboring electrodes leading to a net flow in the direction of the traveling wave [141,142]. AC

electroosmosis has been also used for microfluidic mixing [143,144], for analyte transport for enhanced and more sensitive immunoassays [145], and to increase the hybridization rate and limit-of-detection of target DNA molecules for electrochemical impedance spectroscopy [146].

AC electroosmosis can be highly affected by the applied AC signal frequency and the fluid electrical conductivity. At low frequencies, there is enough time for the charges to respond to the electric field and thus most of the applied voltage is dropped over the double layer and the AC electroosmosis velocity tends to approach zero. Similarly, the AC electroosmosis velocity is negligible when a high frequency is applied since there is not enough time for the ions to screen the electrode surface and thus the majority of the electric field is dropped over the bulk fluid medium [147]. This voltage-drop over a fluid, if potentially applied to a relatively high electrical conductivity fluid, can lead to the AC electrothermal motion as explained later [148]. Moreover, the thickness of the electrical double layer at the electrode-electrolyte interface is inversely proportional to the fluid electrical conductivity [136], and thus with high electrically conductive fluids, the AC electroosmosis tends to be weaker. In addition to that, with increasing fluid electrical conductivities and at an applied frequency range that suppresses the AC electroosmosis effect, the joule heating of the fluid leads to increasing fluid temperatures and stronger AC electrothermal effects. Therefore, AC electroosmosis can be suitable for certain experimental conditions that satisfy the above-mentioned limitations of the applied AC signal frequency and the fluid`s electrical conductivity.

1.3.3.2.B Dielectrophoresis (DEP)

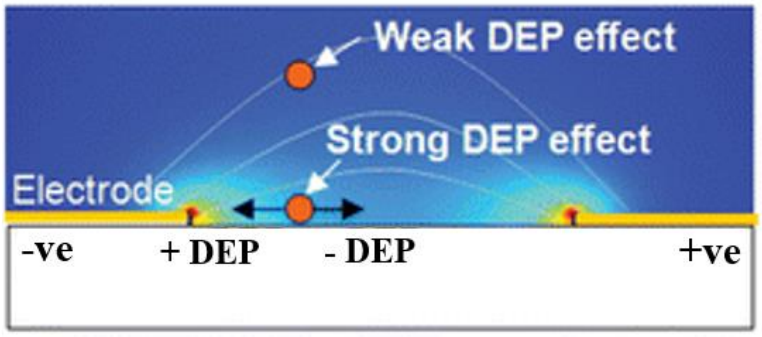

Figure 1.7 The concept of dielectrophoresis (DEP). *Particles (orange) in a microfluidic chamber and under a non-uniform electric field will experience a net force either in the direction of higher electric field strength (+DEP) or towards the area of lower electric field strength (-DEP). The DEP motion and direction depend on several factors inducing the electrical conductivities and permittivities of fluid and particle, particle size, and both the frequency and strength of the electric field. This figure was adapted [1] for dissertation writing purposes.*

When a polarizable dielectric object is placed under the effect of an electric field, the charges in the object will temporarily redistribute to respond to the induced dipoles. The positive charges will experience a pulling force toward the region of a higher electric field, while the negative charges will experience a pushing force away from the region of a higher electric field. In a uniform electric field, where the electric field is the same in all directions, the Coulomb forces on the positive and negative charges will cancel each other out, resulting in no net DEP effect. However, in a non-uniform electric field, where the electric field is stronger on one side of the object than the other, the charge distribution on the object will not be equal. As a result, there will be a non-zero Coulomb force acting

on the object, leading to a net DEP effect [131–133]. This force can therefore lead to the motion of a polarizable object under the effect of a non-inform electric field as applied to a couple of electrodes (or more).

As shown in Figure 1.7, DEP can lead to either the attraction of the polarizable objects to the area of high electric field intensity closer to the electrodes` edge (positive DEP) or repelling them far away from the high electric field intensity region (negative DEP). The polarizable objects will experience either a positive or negative DEP based on several factors, including the effective polarization between the objects and the medium and the frequency of the applied signal. The time-averaged DEP force $\langle F_{dep} \rangle$ acting on a spherical particle with radius (r) and electrical permittivity ε_P suspended in a fluid medium with electrical permittivity of ε_m is shown by equation (1.4)

$$\langle F_{dep} \rangle = 2\pi r^3 \varepsilon_m \, Re[f_{cm}] \nabla |E_{rms}|^2 \qquad 1.4$$

Where f_{cm} is the Clausius–Mossotti factor and is defined with equation (1.5)

$$f_{cm} = \frac{\varepsilon_P^* - \varepsilon_m^*}{\varepsilon_p^* + 2\varepsilon_m^*} \qquad 1.5$$

The complex permittivity ε^* can be calculated using equation (1.6)

$$\varepsilon^* = \varepsilon + \frac{\sigma}{j\omega} \qquad 1.6$$

Where $j = \sqrt{-1}$, ε is the permittivity, σ is the electrical conductivity, and ω is the angular frequency. *Re[..]* means taking the real part of the expression within *[..]*. The direction of the DEP force is determined by the sign of the real part of the Clausius–Mossotti factor shown in equation (1.5), where an object with higher polarizability than the surrounding medium will experience a positive DEP (getting attracted to the area of high electrical field intensity ~ electrodes edge), and if the object has less polarizability than the surrounding medium, it will experience a negative DEP (pushed away from electrodes edge) [149,150]. The application of DEP on biological cells is more complex than the basic assumption of imagining them as spherical uniform particles since the cells contain several materials and inhomogeneous structures (such as cell membrane and cytoplasm and nuclei) where each material has different electrical properties. This leads to a more complex and frequency-dependent permittivity and thus each cell will show a different dielectric response and DEP spectra. There have been several efforts for investigating the DEP responses of different molecules, such as the dielectric response of red blood cells and *E. coli* bacteria in different conductive conditions [151], and the friend murine DS19 and yeast and plant protoplast rapeseed cells [152] at different frequencies.

DEP has been adopted by several research groups for various microfluidic applications. It has been used based on a quadruple electrode geometry to position DNA molecules and bovine serum albumin (BSA) proteins and nanoparticles at well-defined positions on a chip [153]. Another group has utilized the nanopipette design (nanopipette with an internal diameter of a tip in the range of 100–150 nm) to create a high electric field and large DEP forces to achieve reversible trapping and concentrating (of

at least a factor of 300) of protein G and immunoglobulin G (IgG) [154]. Other groups have applied DEP for the non-labeled separation of biological cells [155], and others have shown a preliminary investigation of the DEP chromatography concept where several protein molecules and DNA oligonucleotides would experience different DEP forces and thus exhibit a longer elution time [156,157]. In addition to that, DEP has been used for enhanced and sensitive biosensing applications. Positive DEP was used to trap antibody-coated peptide nanotubes between two gold electrodes and subsequently used for the label-free detection of low concentrations of the herpes virus type 2 [158]. DEP has been additionally used in conjugation with AC electroosmosis for label-free attomolar biosensing of prostate-specific antigen (prostate cancer biomarker) with an increase of 10^4 in the assay sensitivity compared to an only-diffusion controlled device [159]. Finally, DEP has been employed for molecular patterning where individual cells can be placed at specific locations and several subsequent investigations can be carried out such as single-cell physiology studies, cell-cell interactions, and in vitro studies of the interactions between stem cells and surrounding niche cells that can affect their division [133,160,161].

It can be noted from equation (1.4) that the DEP force scales with the gradient of the electric field square and the cube of the microparticle radius, which can impose several challenges and limitations that need to be considered. This means that the DEP force will decay rapidly with an increasing distance from the electrodes. Additionally, the utilization of the DEP to manipulate sub-micrometer and molecular-size objects would require very high electric field intensity to provide enough DEP forces acting on these small-size objects, and to reach those far away from the electrodes` edge and throughout the fluidic chamber. Moreover, at this scale, the DEP forces can be on the same order of magnitude as other forces that can act on the suspended objects, such as electrohydrodynamic forces and sedimentation forces, and Brownian motion [132]. In parallel to that, applying DEP to high electrically conductive buffers, such as present with many biological experiments (to sustain the pH level and the osmotic balance) would mean that high AC electrothermal forces and high temperatures (Joule heating) are expected. Ramos et al.[132] have estimated an expression (equation 1.7) that shows the relative magnitudes of the DEP and the electrothermal velocity of a particle with a radius (r) located at a distance (x) far from the gap of two parallel electrodes and with an actuation voltage (V),

$$\frac{v_{electrothermal}}{v_{dep}} \, \alpha \, \frac{\sigma V^2 x^2}{r^2} \qquad 1.7$$

It shows clearly that with increasing fluid conductivity and decreasing particles` sizes, the fluid flow due to the electrothermal effects will be higher, while the DEP effects can be more dominant and limited to the area closer to the edge of the electrode. This domination of AC electrothermal forces over the DEP forces at high frequencies and high conductive fluids has been investigated and validated by several numerical and experimental methods [162–165].

1.3.3.2.C AC electrothermal flow (ACET)

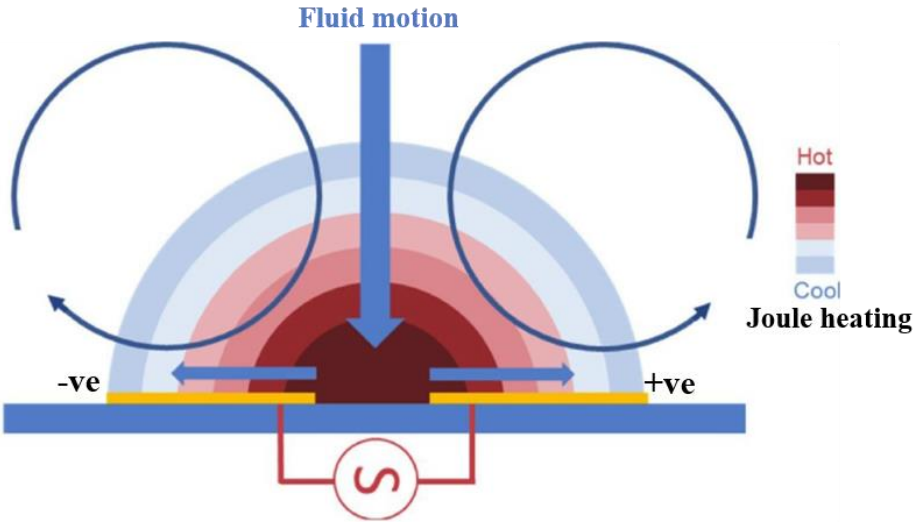

Figure 1.8 The concept of AC electrothermal flow (ACET). *The application of an AC signal to electrodes in a conductive fluid would lead to the Joule heating effect with higher temperature close to the electrodes gap versus far away distances. This temperature gradient would induce a charge density gradient, which would respond to the non-homogenous electric field and leading to fluid flow vortices. This figure was adapted [1] for dissertation writing purposes.*

When a non-homogeneous electric field is applied to a conductive fluid, such as a water-based sample with a high ionic concentration commonly found in biological assays, temperature gradients can be generated due to the Joule heating effect. Joule heating occurs when an electric current passes through a conductive medium, and it leads to local heating due to the resistance of the medium to the flow of electric current. This can result in localized temperature variations within the fluid, as shown in Figure 1.8. The source of temperature gradients can also come from external sources, such as strong illumination, which can also induce localized heating in the fluid [166]. These temperature gradients can, in turn, lead to local variations in the electrical conductivity and permittivity of the fluid, creating charge density gradients. The non-homogeneous electric field then acts on these charge gradients, generating local fluid vortices or flow patterns above the electrodes and throughout the fluid chamber. This phenomenon is known as AC electrothermal flow (ACET) or electrothermal convection. ACET has been found to be suitable for biological fluid manipulation, as it can be stronger in higher electrically conductive fluids compared to other electrokinetic phenomena, such as AC electroosmosis, which relies on the electrical double layer near the electrode surface. ACET is also not spatially limited to a certain distance above the electrodes, as in the case of dielectrophoresis, where the manipulation of particles or cells is typically confined to a narrow region near the electrodes.

ACET has been extensively applied in several microfluidic applications such as mixing, pumping, trapping, and particle manipulation. For example, it has been integrated into a small portable diagnostic device for the enhanced detection of bacterial pathogen infection (MAP) with 10 times acceleration in the detection time [167]. Additionally, ACET mixing has been implemented for enhancing the immuno-diagnostic assay for the detection of myeloperoxidase, which is an inflammatory marker released by the immune system, as a defense against pathogenic infection [168]. The detection time was successfully reduced from about 210 min to 30 min. Other groups have optimized ACET while taking

into consideration the potential of having DEP effects on the bioreagents, to reduce false positive results [169]. They have achieved a 30-fold acceleration of the immunoassay time as compared to the diffusion-limited assay. Similarly, ACET has been used for micro-pumping applications as an alternative to micromechanical pumps which might require a more complicated fabrication and includes moving parts. It has been applied on different asymmetric-electrodes designs (electrodes with different widths, or T-shape design) and could generate a directional fluid pumping in fluids with high conductivity (0.754 S⁄m) with a fluid flow of more than 85 µm/sec [170]. Later, the same group [171] has shown a further improvement of the ACET micro pumping, by superimposing a small DC signal to the AC signal applied to the same electrodes to achieve electrical potential asymmetry, and could achieve pumping velocities up to 2500 µm /sec. However, no clear indication of the solution conductivity was found. Another group [172] followed a different approach where they applied a two-phase AC signal to asymmetric electrodes and could achieve up to 50% faster fluid pumping rates than the single-phase actuation system. This approach can help reduce or eliminate the possible side effects with higher voltages or DC biasing such as the glass bubbles formation and electrodes` dissolution. ACET has been also applied in conjugation with DEP to trap and concentrate *E. coli* [173] or circulating cell-free DNA [174] for enhanced detection, or continuous particle trapping and sorting and switching to certain regions of interest [175].

1.3.3.3 Sound field-based mixing: acoustofluidics

Acoustofluidics is a field that involves the fusion of acoustics and fluids, and it has been extensively investigated and utilized for the manipulation of fluids and particles in microfluidic systems [176]. The field of acoustofluidics has gained significant interest in academic research in recent decades. However, the use of acoustics for manipulating fluids and particles can be traced back to the famous Kundt's tube experiment in 1866 [177]. Kundt's tube experiment involved a metallic rod resonator placed at the end of a tube that was filled with small particles dispersed in a fluid. When the resonator was vibrated, it generated standing waves in the fluid inside the tube, and over time, the particles accumulated at the vibration nodes of the standing waves. This experiment demonstrated the ability of acoustic waves to manipulate particles in a fluid medium and laid the foundation for the field of acoustofluidics. Subsequently, Dvorak reported a similar phenomenon of acoustic manipulation of air [178], and the first theoretical model of acoustic manipulation was proposed by Rayleigh in 1884 [179]. Further developments in the field of acoustofluidics were made by Schlichting and Westervelt, as well as Nyborg, among others [180,181]. These early studies paved the way for the current research and applications of acoustofluidics in diverse fields, including biotechnology, chemistry, and physics, where it has found numerous applications for fluid and particle manipulation in microscale systems.

Acoustofluidic devices are typically categorized into two main types based on the working concepts: bulk acoustic wave- (BAW) and surface acoustic wave- (SAW) devices. In the case of BAW, an AC signal is applied to a piezoelectric transducer, the piezoelectric material vibrates due to the piezoelectric effect, which then generates bulk acoustic compressional waves that can propagate through the solid material of the microfluidic device and leading to fluid and particle motion [182]. On the other hand, SAW can be realized by microfabrication of metallic interdigital transducers (IDTs) on the surface of a

piezoelectric substrate [183], such as made of quartz, lithium niobate ($LiNbO_3$), or lithium tantalate ($LiTaO_3$). RF signals applied to the IDTs excite the piezoelectric material, generating acoustic waves that propagate along the surface of the material, hence the name "surface acoustic waves". The microfluidic device is typically built on top of the SAW substrate, and the SAWs can propagate along the solid-fluid or solid-air interface. When the SAWs come into contact with the microfluidic device, they propagate and leak into the fluid domain in the form of leaky waves, leading to fluidic and particle motion [184].

Both BAW and SAW-based acoustofluidic devices have their advantages and are used in different applications depending on the requirements of the specific manipulation tasks, such as the type of particles being manipulated, the desired fluid flow patterns, and the overall system design.

For example, SAW devices offer advantages in terms of wider and higher operating frequencies, as well as more precise and controllable manipulation of fluids and particles. However, the fabrication of IDTs on the piezoelectric substrate can be more complex and costly compared to the realization of BAW devices [184]. SAW devices also do not require fluidic channels to be made of specific materials with specific acoustic characteristics, as is frequently the case with BAW devices. On the other hand, BAW devices rely on cheap piezoelectric transducers (down to 0.5 USD) that can be placed at a distance from the microfluidic chambers, providing a cost-effective and flexible approach for integration and testing [185].

Due to the interaction between the acoustic waves and fluids, channel walls, and dispersed particles, several phenomena such as scattering, absorption, reflection, and dampening can occur, resulting in a change in the gradient of the intensity of the propagating acoustic waves [186]. The manipulation of fluids and particles with acoustic waves can be generally governed by two forces: acoustic radiation forces and acoustic streaming. In a standing wave (superposition of two acoustic waves), the primary acoustic radiation forces can act on particles (such as cells, beads, and bubbles) suspended in a fluid, leading to their movement toward the acoustic pressure nodes or antinodes [187]. Equation (1.8) describes the primary acoustic radiation force (F_R) acting upon a compressible spherical object in a standing wave [183,187].

$$F_R = -\left(\frac{\pi p_0^2 V_p}{2\lambda} R_f\right) \phi(\beta,\rho)\, sin\left(\frac{4\pi x}{\lambda}\right) \qquad 1.8$$

where ϕ is the acoustic contrast factor and is defined by equation (1.9),

$$\phi(\beta,\rho) = \frac{5\rho_p - 2\rho_f}{2\rho_p + \rho_f} - \frac{\beta_p}{\beta_f} \qquad 1.9$$

and $p_0\ and\ V_p$ are the acoustic pressure amplitude and the particle volume. The parameters β_p, ρ_p, β_f, and ρ_f are the compressibility and density associated with the fluid and the particle, respectively (subscript f and p represent the fluid and particle, respectively). The parameters β, ρ, λ, and x are the compressibility, density, wavelength of acoustic waves, and distance of a particle from the pressure node, respectively. Particles with different compressibility, density, and size will be affected

differently by the acoustic radiation forces, and this forms the basis of the field of acoustofluidic separation or acoustophoresis [182,188]. The sign of the acoustic contrast factor ϕ defines the equilibrium position of the particles in the acoustic pressure field. A positive ϕ means that particles will be directed to the pressure nodes (low-pressure zone) while a negative ϕ means that particles will move to the pressure antinodes (high acoustic pressure regions) [189].

The other force involved in the manipulation of fluids and particles with acoustic waves is the acoustic streaming force, which arises from the attenuation of the acoustic waves in the viscous fluid, forming gradients in the time-averaged acoustic momentum flux in the fluid. This leads to the net displacement of fluid particles and the formation of streaming flows. There are two common classes of acoustic streaming, namely boundary-driven streaming (inner boundary Schlichting streaming and outer boundary Rayleigh streaming), and bulk-driven streaming (Eckart streaming or quartz wind) [190]. The streaming force that moves spherical particles with radius (r) can be approximated by the Stokes drag forces (F_{drag}) [182]

$$F_{drag} = 6\pi\mu r v \qquad 1.10$$

Where μ, r, and v are the dynamic viscosity of the liquid medium, the radius of particles, and the relative velocity of the particle with respect to the medium, respectively.

Acoustofluidic technologies have been used for microfluidic applications such as fluid mixing [191] and pumping [192], particles separation, sorting, focusing, and patterning [183], and also for nebulization [193], single cells and organisms rotation [194], and cell lysis [195]. One class of the proposed acoustofluidic mixers relies on the oscillation of the sharp edges fabricated inside the microfluidic chamber under the actuation of the piezoelectric transducer. This oscillation creates a pair of counter-rotating vortices around their tips leading to acoustic streaming flows in the vicinity and which are effective for fluid mixing. A low frequency (4~5 kHz) sharp-edge microfluidic mixer has been proposed and was capable of effective fluid mixing at different fluid flow rates and with mixing time down to ~180 msec [196]. Another group reported the characterization of sharp edges fabricated with different angles and could achieve up to 73 mm/s acoustic streaming velocity [197]. The same concept of sharp-edge acoustofluidic mixers has been integrated for fast fluidic mixing, and on-chip quantitative detection of IL-6 protein biomarker (immune and inflammatory protein) using a continuous flow ELISA (enzyme-linked immunosorbent assay) platform [198].

Another class of acoustofluidic mixers relies on bubble-induced acoustic streaming, also called cavitation streaming. This technique relies on the trapping of gas bubbles inside microfabricated grooves in the chamber, and the subsequent oscillation of the bubble surface (vibrating membrane) under the effect of the acoustic actuation [190,199]. This oscillation generates frictional forces at the gas/liquid interface and induces a bulk streaming motion around the bubble. One group reported the formation of air pockets at the walls of a microfluidic chamber that is glued above a piezoelectric transducer [200]. The actuation of the bubbles leads to a strong microstreaming effect that could reduce the time required for efficient mixing of a dye-water mixture from 6 hours to 35 sec. Moreover, an alternative setup with air pockets at the top of the chamber was able to enhance the immunomagnetic

cell capture of bacterial cells (*E. coli* K12) suspended in blood by 71% as compared to the diffusion-limited experiments without acoustic mixing. The same group reported the application of bubble microstreaming for mixing to enhance DNA hybridization in a DNA microarray [201]. They reported up to 5-fold enhancement in the hybridization signal and similarly in the hybridization kinetics. Another group reported the usage of two bubble microfluidic chamber for the immunoassay detection of PSA (prostate-specific antigen) [202]. The device was capable of reducing the assay detection time of PSA by 2.3 and 3.1 times for the high and low PSA concentrations, respectively.

Similarly, SAW devices have been implemented for acoustofluidic mixing, where the surface propagating waves can radiate and leak their energy in the fluid upon their contact, generating pressure waves in the fluid that cause acoustic streaming [203]. A SAW mixer has been integrated with a low-cost disposable chip for the enhanced immunoassay detection of interferon-γ (biomarker used in the diagnosis of tuberculosis) while reducing the non-specific binding [204]. Another group reported the integration of SAW mixing for enhancing the surface plasmon resonance (SPR) biosensing of biomolecules, where the device comprised the SPR detection surface and the SAW substrate at the two opposite sides of the chamber [205]. The SAW microstreaming was capable to double the SPR signal as compared to the static non-mixing condition while increasing the biomolecules' binding rate. Taking advantage of the same concept of the SAW mixing-SPR coupled biochemical assay while integrating the SPR sensing surface and the SAW electrodes on the same substrate ($LiNbO_3$), another team reported approximately 5-time enhancement in the reaction kinetics with the SAW mixing [206]. Interestingly for surface-based assays, several groups have reported the application of SAW, not for microfluidic mixing, but to enhance the sensitivity and specificity of the bioassay by removing the nonspecifically bound reagents and reducing the biofouling [207–210].

Other simpler approaches were adopted by other groups aimed for acoustofluidic mixing. For example, locating an open-well chamber between two audio speakers could achieve efficient mixing in the chamber due to the strong acoustic streaming effects [211]. Similarly, 2×2 open-wells were mounted on a custom-made acoustic mixer and used for enhancing an ELISA readout. The acoustic mixer generated a dipole flow pattern that circulated the fluids within the open well and increased the initial rate of antibody-antigen binding by over 80 % while reducing the assay time from 45 min (without mixing) to 9 min [212].

Some industrial companies have implemented acoustofluidic technologies for real-life applications. For example, the USEPAT company [213] offers the Soniccatch device that can trap in 3D and against a running fluid, different sizes of particles (1-100 µm) creating agglomerates at the probe end for the subsequent analysis. The Acousort Company [214] provides different acoustofluidic-based devices for the microfluidic isolation and enrichment of particles (exosomes and cells) and for particles` separation, such as plasma separation from blood samples and cell washing. Finally, the Thermofisher company provides the Attune Flow Cytometer [215] which is claimed to possess a faster and more efficient cytometry analysis due to the acoustic-assisted hydrodynamic focusing of the cells.

1.4 Thesis outline

Chapter	Technology	Simulation	Experiments	Graphical abstract
2	AC electrothermal flow	✓	✓	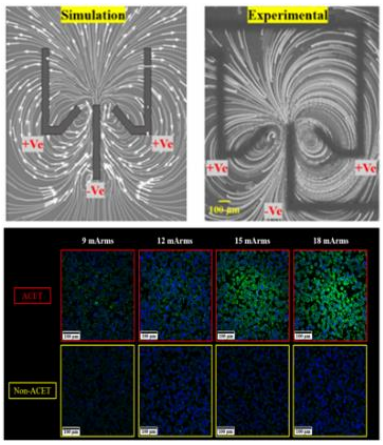
3	AC electrothermal flow	✓	limited	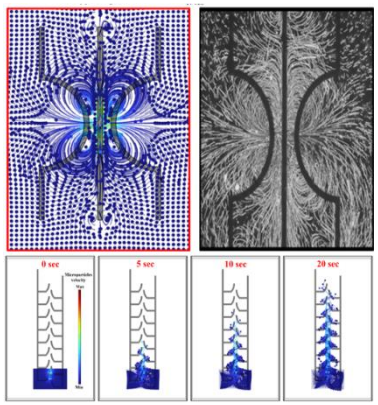
4	Acoustofluidics	✓	✓	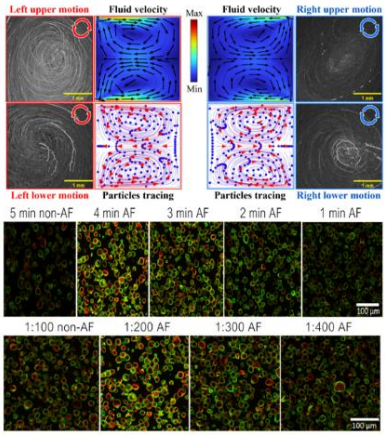

Table 1-3 Thesis outline

In the current thesis, our focus is on investigating two different microfluidic mixing technologies, namely AC electrothermal flow-based and acoustofluidic mixing, and their applications for enhancing microfluidic immunoassays and spatial proteomic analysis.

In the second chapter, we illustrate how the concentration of the detection reagents and their reaction kinetics can affect the surface-based assays. Then, we propose a new design for AC electrothermal flow (ACET) that can generate ACET in-plane motion, and validate it through both numerical simulation and experiments, and we compare it to the traditional ACET design with parallel electrodes. After that, we take advantage of the design and its enhanced performance and apply it to enhance the immunoassay detection of cancer biomarkers on cell pellet sections. Furthermore, we demonstrate the scalability of the design and provide thermal characterization, as well as investigate the relationship between immunoassay signal enhancement and the spatial location of the design in relation to the target sample. We also explore how this scaling-up approach can facilitate fluid mixing over larger areas, thereby reducing incubation time and enhancing immunostaining of the cell pellet sections.

In the third chapter, we further characterize the newly proposed ACET design using numerical simulation and investigate possible interference from negative DEP effects at similar experimental conditions. Building on the concept of the new ACET design, we propose additional in-plane ACET microfluidic mixing designs, with experimental verification of one of the designs. We subsequently conducted a preliminary investigation of ACET microfluidic motion and fluid flow analysis using an array of in-plane ACET designs. Finally, we explain how this design array can be utilized for microfluidic pumping, capitalizing on the in-plane nature of the fluid motion achieved with the new designs.

The fourth chapter of the thesis delves into several factors that can affect spatial proteomic analysis on large-scale tissues, including fluid flow rate, the concentration of detection reagents, and incubation time with the target sample. Additionally, we investigate the integration of acoustofluidic technology for large-scale microfluidic mixing. Through numerical simulation and experimental validation, we demonstrate the effect of piezoelectric actuation on inducing microfluidic mixing motion. We also study the impact of fluid flow rate on the homogeneity of immunostaining of the target tissue and how acoustofluidic mixing can be utilized to achieve spatially homogeneous signals. Furthermore, we show how reducing incubation time or concentration of detection reagents for the purpose of improving analysis time and cost can potentially compromise immunoassay performance. Finally, we demonstrate the effect of integrating acoustofluidic mixing on achieving higher signals with shorter incubation times and lower concentrations of reagents.

49

2 Efficient AC electrothermal flow (ACET) on-chip for enhanced immunoassays

This chapter is an adapted version of the following publication:

- **Muaz S. Draz (M.D.)**, Kevin Uning (K.U.), Diego Dupouy (D.D.), and Martin A. M. Gijs (M.G.), "Efficient AC electrothermal flow (ACET) on-chip for enhanced immunoassays". Lab Chip, 2023,23, 1637-1648. Creative Common license: https://creativecommons.org/licenses/by-nc/3.0/. Authors contribution: Conceptualization: M.D., D.D., M.G., Simulation: M.D., K.U., Experimental Investigation: **M.D.**, Data Curation: **M.D.**, K.U., Visualization: **M.D.**, Writing original draft: **M.D.**, Editing: **M.D.**, K.U., D.D., M.G., Supervision: D.D., M.G. This project has received funding from the European Union's Horizon 2020 research and innovation program under the Marie Skłodowska-Curie grant agreement No. 754354.
- "Patent application EP 22207056.7 filed the 11.11.2022, not published yet, results are confidential"

Biochemical reaction rates in microfluidic systems are known to be limited by the diffusional transport of reagents, leading often to lowered sensitivity and/or longer detection times in immunoassays. Several methods, including electrically powering electrodes to generate AC electrothermal flow (ACET) on-chip, have been adopted to enhance the mass transport of the reagents and improve microfluidic mixing. In this chapter, we report a novel ACET electrode design concept for generating in-plane microfluidic mixing vortices that act over a large volume close to the reaction surface of interest. This is different from the traditional ACET parallel electrode design that provides rather local vertical mixing vortices directly above the electrodes. Both numerical simulation and experimental studies were performed to validate the new design. Moreover, numerical simulation was carried out to show the effects of experimental factors such as the reaction kinetics (association constant) and the reagent concentration on the ACET-enhanced surface-based assays. As a proof of concept, the new design for the ACET-enhanced immunoassays was used to improve the immunostaining signal of the HER2 (Human epidermal growth factor receptor 2) cancer biomarker on breast cancer cells. Finally, the concept of scaling up the design has been validated by experiments (Immunoassays on breast cancer cells for different ACET power and different assay times). In particular, we show that larger ACET in-plane designs can agitate and mix the fluid over large microfluidic volumes, which further enhances the immunoassay's output.

2.1 Introduction

Since the early development of microfluidic systems, they have been used in a plethora of applications such as medical diagnostics and biosensors[216], chemical synthesis,[217] cell analysis,[218,219] drug discovery, transcriptomics[220,221], and many other applications. This is triggered by the numerous advantages that microfluidics can offer, as explained in the first chapter. In many surface-based assay techniques, such as Surface Plasmon Resonance Sensing (SPR),[52] Immunohistochemistry (IHC),[68] and Fluorescence In-Situ Hybridization (FISH),[222] the bio-chemical reagents (DNA, antibodies, etc.) and the target sample (cells, tissues, etc. mounted on a substrate) are incubated inside a microfluidic chamber. During incubation, depending on the reaction kinetics rates, the reagents in the volumetric vicinity of the target sample are consumed, and a depletion region with a much lower concentration is formed over the sample.[90,223,224] Unless the kinetic rates are the limiting factor, the reaction rate becomes limited by the transport of the reagents to the target sample, leading to lengthy experiments. Furthermore, the time for the mass transport of the reagents would further increase if the reagents also need to diffuse across the in-plane dimensions (x and y direction) in addition to the vertical transport direction (z). This limitation is highly present in applications that require analyzing and incubating large-size samples (mm and cm range) in thin chambers, such as the applications of microfluidics for tissue diagnostics.[82,225–227] Tissue diagnostics using IHC and FISH are considered the golden standards for breast cancer diagnosis, one of the most deadly cancers in women, and have been approved by the United States Food and Drug Administration (FDA) for the assessment of protein level expression or gene copy counting respectively.[228] Therefore, any improvement in the cost and time, and efficiency of these diagnostic techniques can be valuable. A wide range of theoretical and experimental methods have been investigated to enhance the microfluidic mixing and overcome the limited mass transport, such as the use of electro-hydrodynamics,[229] electro-kinetics,[230] magnetic stirring,[231] vibrating membranes,[232] acoustofluidic bubble cavitation,[233] and pressure field modulation.[234] Each of the different mixing technologies has its merits and each can be more adapted to a particular application. For example, acoustic vibrating structures can offer high mixing efficiency but require a complicated and lengthy micro-fabrication process and would typically require the resonance frequency matching of the attached piezoelectric device with the vibrating structure. Acoustic bubble cavitation similarly requires efficient bubble formation and trapping. Moreover, acoustic mixing may require high-voltage and high-frequency generators [94]. Magnetic stirring can provide microfluidic mixing using magnetic beads or rods dispensed into the chamber, but would require a closely attached magnetic actuator, and might rely on the formation of bead chains [112] while hindering the optical readout if not interfering with the bio-chemical assays [125].

AC electrothermal flow (ACET) is a technique from the AC electro-kinetics family that has been studied extensively and utilized for microfluidic mixing,[90,163,235,236] pumping[170–172], trapping, [173,237], and particle manipulation.[238,239] ACET can be suitable for biological assays since the latter are usually done in electrically conductive buffers. Thus higher ACET effects can be obtained in a more conductive fluid, but, on the other hand, the maximum allowable temperature is limited: a high temperature can lead not only to electrolysis and bubbles formation that can affect the experiments and lead to the

electrodes` deterioration, but can also affect the bioreagents' stability and functionality.[163,240–242] On the contrary, some applications might benefit directly from the coupled effects of microfluidic mixing and the high temperature generated, such as thermal cycling for DNA amplification for PCR applications.[243] Another disadvantage might be that the microelectrodes required for the ACET actuation can hinder the optical readout for different assays, but an alternative solution would be the usage of transparent conductors such as Indium tin oxide (ITO). [244]

Most of the reported ACET flow literature work relied on the parallel electrode concept, where a pair of electrodes (or an array of electrode pairs) is pulsed by an AC electric field.[167,236,245–247] Doing so generates two counter-rotating vertical vortices above the electrodes, which can be used to replenish the bulk fluid above the target reaction surface. The ability of the rotating vortices to drag fresh reagents from regions away from the electrodes and thus replenishing more volumes is limited by the maximum electric field that can be applied in order not to increase excessively the generated temperature. The high-temperature region is usually localized in a small volume close to the electrode gap, where the electrical field strength is maximum and can cause several limitations as explained later. In addition, the parallel electrode design generates temperature along the full parallel length which leads to a local high average temperature. As an alternative, previous research efforts [166,248] have shown a rotational in-plane fluid flow profile, but the system design had four large coplanar electrodes actuated with a four-phase AC signal to generate a rotating electric field thus increasing the complexity of the system.

To address these issues with ACET, we introduce a novel concept of electrode design that relies on having two tilted electrodes biased against a middle electrode with a singly-phased AC signal. This generates a three-dimensional fluidic motion with two in-plane counter-rotating vortices combined with vertical flow profiles. The in-plane motion is capable of increasingly refreshing the fluid over the reaction area from a large volume in the microfluidic chamber. Moreover, the new design, due to its increasing gap between the electrodes, possesses a lower average temperature as compared to the parallel design at the same voltage. We suggest that the reported work can serve as a basis for more efficient microfluidic mixing systems and their potential applications. We show the flow patterns using both numerical simulation and experiments with fluorescent micro- and nanoparticles. The numerical simulation also allows us to point out the importance of mass transport in regard to the reaction kinetics (association constant) and the reagent concentration, and the possible improvements enabled by microfluidic mixing. We then demonstrate the feasibility of the new ACET technique for the improved immunostaining of the HER2 tumor marker (human epidermal growth factor receptor2, also known as ERBB2) on cancer tissue slices. HER2 is overexpressed in 15–20% of breast cancer cases, causing rapid progression and poor prognosis of the disease [82]. To the best of our knowledge, this is the first research that demonstrates ACET mixing for IHC-based diagnostics. Finally, we demonstrate the advantageous scaling of the proposed design, going for a larger mixing coverage area when using longer electrodes and a bigger gap between the electrodes, and demonstrate improved immunostaining of cancer cells thanks to the ACET-based microfluidic mixing.

2.2 Experimental setup

Our system relies on the use of a thin and wide microfluidic chamber that has been used before for studying cancer biomarkers on biological samples [64,68,222,225]. The system uses a polymer chip (Figure 2.1.a) that provides fluidic accessibility to the chamber through multiple inlet holes (small white circles), and an imaging window in the middle of the chamber. The window is made of a glass coverslip on which the electrodes' microstructures are fabricated and face the inside of the fluidic chamber. Our novel in-plane vortex design has two electrodes tilted and biased against the middle electrode. The electrodes are interfaced with insulated electrical wires to a high voltage amplifier (WMA-300, Falco-system) that is connected to a function generator (AFG3021B, Tektronix), and the signal over the electrodes is monitored by an oscilloscope (54602B, HP). A rubber O-ring (Figure 2.1.b) is used to seal the area around the center window and prevent any fluid leakage. The polymer microfluidic chip is mounted inside the integrated system (Figure 2.1.c) and clamped against the lower sample part. The lower part of the system hosts the sample slide (glass microscopy slide carrying a thin section of biomaterial), which is located above the temperature-controlling system. Figure 2.1.d shows the core geometry of the setup that is used for the simulation, which consists of a microfluidic chamber (15×15×0.05 mm^3) sandwiched between a glass coverslip with the electrode's microstructure and a bottom sample glass slide. All fluid handling and flow rates were controlled by an integrated pressure

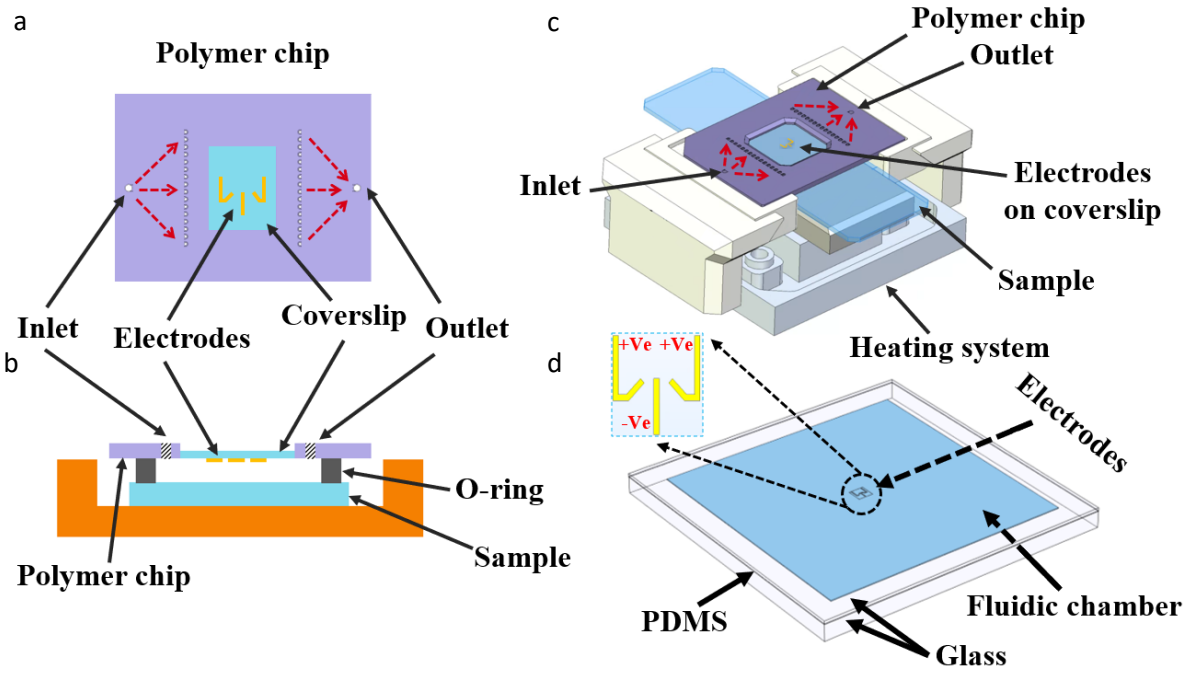

***Figure 2.1 Experimental setup**. (a) Top schematic view of the polymer chip used with the fluidic access holes (a larger white inlet hole diverging into multiple fluidic paths represented by red-dashed arrows to dispense the liquid into the chamber through the small white holes, similar for the outlet) and the microfabricated electrodes design on the glass coverslip (the design size is enlarged just for visual clarity). (b) Cross-sectional schematic side view of the experimental setup showing the polymer chip clamped against the sample slide with an O-ring that seals the microfluidic chamber (15×15x0.05 mm^3) (c) 3D design of the integrated experimental setup with the polymer chip clamped against the sample (generally a glass microscope slide carrying a thin tissue section). The lower part of the setup has a heating system that controls the temperature of the setup. (d) Geometry of the 15×15×0.05 mm^3 microfluidic chamber (blue) that is used into the simulation, which has an upper glass coverslip with the electrodes (black), a lower 1 mm-thick sample glass slide (white), and a PDMS spacer slab between both glass slides. The inset figure shows the newly introduced ACET electrodes design concept.*

pumping system. All details of the immunoassay and fluorescence imaging and microfabrication protocols are described in the Methods & protocols section 2.6 of the chapter.

2.3 Numerical simulation

Here we show the numerical simulation of the AC electrothermal including the electrostatics and heat transfer and the resulting fluid flow. Moreover, we explain the model followed for the numerical simulation of the transport of the reagents inside a fluidic chamber, its reaction with a surface-based assay, and how the ACET can affect such a surface reaction.

2.3.1 AC electrothermal flow

The ACET flow originates from the temperature gradients in the bulk fluid, which are generated by the joule heating as a result of the electrical field applied to the electrically high conductive solution, as calculated by the energy balance equation (2.1),[163]

$$k\nabla^2 T + \sigma E^2 = 0 \qquad 2.1$$

where E is the electric field magnitude, T is the temperature, k, and σ are the fluid thermal and electrical conductivities, respectively. The fluid electrical permittivity (ε) and conductivity (σ) are dependent on the temperature according to equations (2.2) and (2.3),[166,249]

$$\frac{\nabla\varepsilon}{\varepsilon} = \frac{1}{\varepsilon}\frac{\partial\varepsilon}{\partial T}\nabla T = -0.004\nabla T \qquad 2.2$$

$$\frac{\nabla\sigma}{\sigma} = \frac{1}{\sigma}\frac{\partial\sigma}{\partial T}\nabla T = 0.02\nabla T \qquad 2.3$$

The electrothermal flow is then formed due to the interaction of the conductivity and permittivity gradients with the electric field. The local electrical charge distribution, described by Gauss`s law and charge conservation[250] (equation 2.4 and 2.5, respectively), responds to the electric field and exerts momentum on the surrounding fluid.

$$\rho_E = \nabla \cdot (\varepsilon E) \qquad 2.4$$

$$\frac{\partial\rho_E}{\partial t} + \nabla \cdot (\sigma E) \qquad 2.5$$

Where ρ_E is the space charge density. The electrical force applied to the charge density is shown in equation (2.6),

$$f_E = \rho_E E - \frac{1}{2}E^2\nabla\varepsilon \qquad 2.6$$

where the first term $\rho_E E$ denotes the Coulomb force and the second term $½\, E^2 \nabla\varepsilon$ denotes the dielectric force. As the charges move under the effect of the electric field, they drag the fluid. The Coulomb force dominates at low frequencies and the dielectric force dominates at high frequencies. For highly conductive solutions (e.g. 1 S/m), the cross-over frequency between the coulomb and dielectric forces is close to the range of 200 MHz,[236] and thus the electrothermal force is dominated by the Coulomb forces in our current work (AC frequency=1 MHz, fluid conductivity=1.5 S/m).

The fluid motion can finally be obtained by solving the Navier-Stokes equation[132] for low Reynolds number systems (equation 2.7) together with the mass conservation (equation 2.8)

$$-\nabla p + \eta \nabla^2 v + F_E = 0 \qquad 2.7$$

$$\nabla \cdot v = 0 \qquad 2.8$$

The time-averaged electrothermal force per unit volume can be calculated by equation (2.9),[90,163,236]

$$F_{ACET} = -\frac{1}{2}\left[\left(\frac{\nabla\sigma}{\sigma} - \frac{\nabla\varepsilon}{\varepsilon}\right) \cdot E \frac{\varepsilon E}{1+(\omega\tau)^2} + \frac{1}{2}|E|^2 \nabla\varepsilon\right] \qquad 2.9$$

where $\tau = \varepsilon/\sigma$ is the charge relaxation time, and ω is the angular frequency of the applied electric field E.

2.3.2 Surface-based reaction rate and analyte transport

The reaction between the immobilized target on the surface and the diffusing analyte is assumed to follow a first-order Langmuir adsorption model.[251] The molar concentration of the analyte-target complex $[AB]$ being formed over the reaction time is related to the analyte concentration at the reaction surface $A_{surface}$, and to the target concentration B_0 by the following equation (2.10),[90]

$$\frac{\partial[AB]}{\partial t} = k_{on}[A]_{surface}\,\{[B_0] - [AB]\} - k_d[AB] \qquad 2.10$$

where k_{on}, k_d are the association and dissociation rate constants respectively. The initial target concentration used is $B_0 = 3.3 \times 10^{-8}$[mol/m²] and the dissociation constant $k_d = 10^{-2}$[1/s], and the association constant k_{on} was simulated for the range of $k_{on} = 10^3 \sim 10^5$[m³/(s.mol)]. The initial bulk analyte concentration available at the surface for reaction $A_{surface}$ was simulated for the range of $10^{-6} \sim 10^{-11}$[mol/m³]. This analyte concentration and the bulk fluid are replenished by the fluid flux according to Fick's second law of diffusion, as shown in equation (2.11),[90]

$$\frac{\partial[A]}{\partial t} + U \cdot \nabla[A] = D\,\nabla^2[A] + R \qquad 2.11$$

where A is the concentration of the analyte in the bulk fluid, U is the fluid velocity, D is the diffusion coefficient of the analyte, and R is the reaction rate, which equals zero in the bulk fluid, as no reaction takes place in the fluid. Full details of the numerical simulation strategy (Figure 2.16) and the variables`

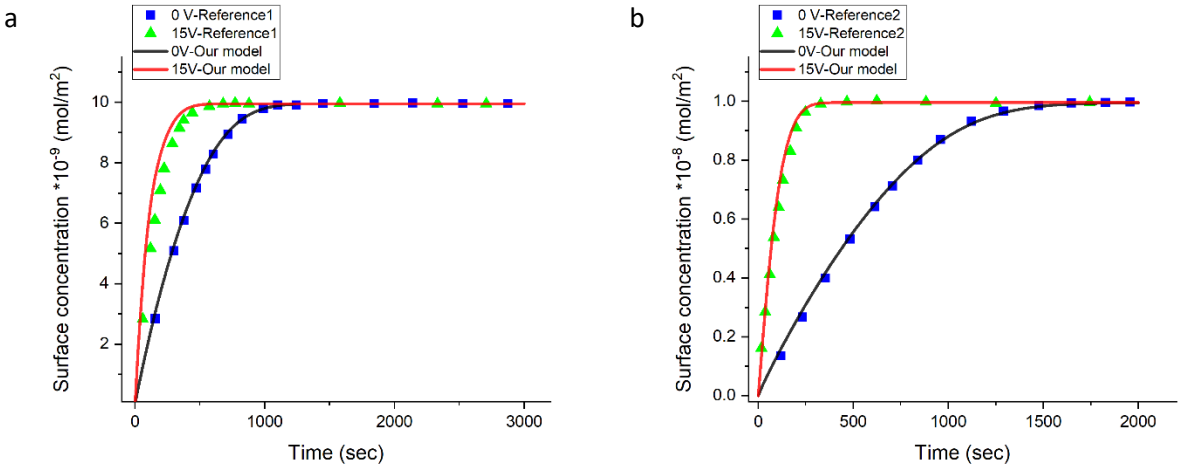

Figure 2.2 Benchmarking of the numerical simulation model used in the current work with simulations from the published literature. *(a) and (b) show the theoretical enhancement of the surface reactions with the AC electrothermal microfluidic mixing using our model and compared with the results of the listed literature.*

values (Table 2-1) and the boundary conditions (Table 2-2) are explained in the Methods & protocols section 2.6. Moreover, our numerical model for the surface-based assays has been benchmarked and validated with known numerical simulations and experimental results from the literature. Here in Figure 2.2, we validated our ACET simulation model against the results published by two groups. Figure 2.2a shows the validation of our model against the system design of Huang K.R. et al. [252] with an electrodes length of 100 µm. Figure 2.2b shows the validation against the system design of Yang C.K. et al.[253] with the reacting surface located at (x=281 µm and y=133 µm) within the 2D simulation. In both cases, we were able to replicate their results with a large agreement between their published work and our model results

Here in Figure 2.3, we validated our simulation model for the surface binding reaction against the experiment done by Berthier J. et al.,[254] in which they monitored the fluorescent signal of different DNA strands hybridizing to surface-immobilized and complementary DNA sequences. The flow is turned on for 50 minutes, then it is stopped for 310 minutes, and it is again turned on for the rest of

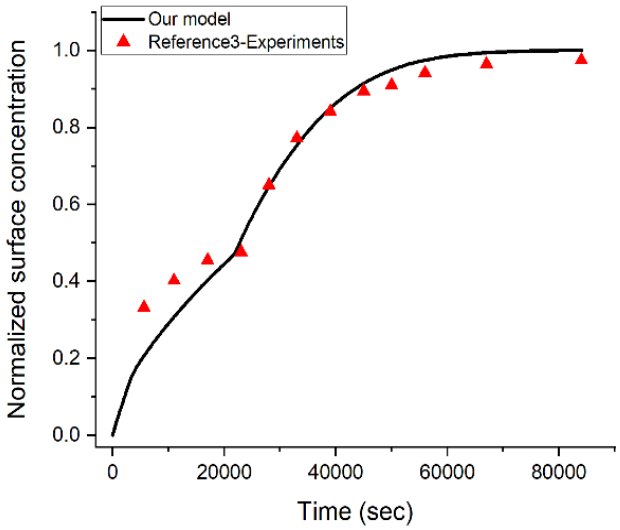

Figure 2.3 Validation of our simulation model for the surface-based reaction against the published experimental results of DNA fluorescent hybridization.

the experimental time which explains the curve shape after 21600 seconds. The average flow velocity is 1 mm/s (10 µl/min) and the dimensions of the microchamber are 10 × 10 × 1 mm^3. The results show a large agreement between the experiment and the simulation modeling results for the surface-based immunoassays. This indicates the accuracy of our numerical simulation, allowing us to fit also other parameters of the surface-based immunoassay experiments, such as reagents concentrations, and association constants.

2.4 Results and discussion

2.4.1 ACET in-plane design flow vortex pattern

Here, we show our results for the numerical simulation and experimental verification of the new in-plane vortex design. Figure 2.4.a shows the numerical simulation of the fluidic streamlines generated by the ACET actuation of the in-plane design. The design has two side electrodes biased and titled (45°) against the middle electrode, which creates localized mixing spots, as shown later. The in-plane motion pulls the fluid from the two sides of the design and pushes it to the center, where the two incoming directed fluid fluxes oppose each other and lead to an upward (top of design) directional motion. A closer look at the cross-section side view of the chamber in Figure 2.4.b shows straight lateral lines between each side electrode and the middle electrode, indicating the in-plane lateral motion. Further clarification of fluidic streamlines of the in-plane and vertical vortex design is shown in Figure 2.15. The streamlines obtained by the new in-plane vortex design are different from the traditional design of parallel electrodes which provides mainly two counter-rotating vertical vortices above the biased electrodes. Figure 2.4.c shows the experimental verification of the fluidic motion

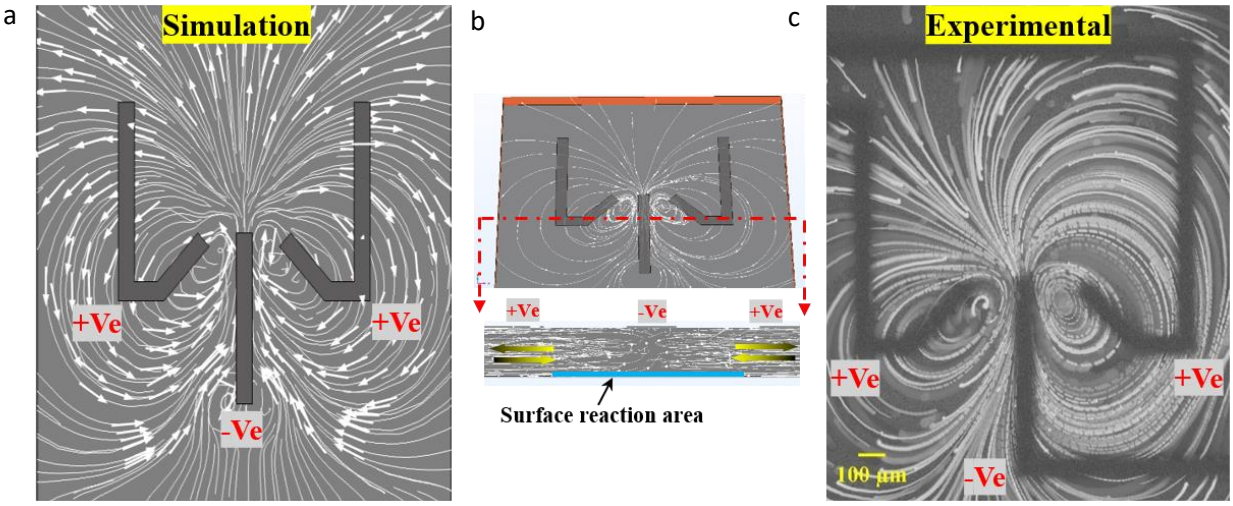

Figure 2.4 Simulation and experimental results of in-plane vortex fluidic motion. *(a) ACET fluidic streamlines obtained by the numerical simulation of the new electrode design, showing two large-area counter-rotating in-plane vortices. (b) Top-tilted and cross-sectional view of the fluidic streamlines at the design`s centre. Arrows indicate the direction of the simulated flow streams. The blue rectangle at the bottom of chamber represents the surface reaction area (represented thicker for visual clarification, but in the simulation, it is a 2D surface) (c) Fluidic streamlines obtained in an experimental verification of the new design. The figure shows superimposed images of a time sequence of 1 µm fluorescent microparticles moving along with the ACET in-plane vortices.*

generated by the new design. The superimposed tracing images of 1 µm-diameter fluorescent microparticles overlap with the simulation results, both in the vortices shape and the direction of fluid motion. Moreover, we also carried out a numerical simulation to validate how small nanoparticles (20 nm) move under the influence of the ACET in-plane motion, in resemblance to small-size reagent molecules. The simulation considers the (i) effect of the fluid drag forces on the particles by using the Stokes drag law, (ii) the effect of the temperature on the Brownian motion and the fluid dynamic viscosity, and finally (iii) gravitational forces.

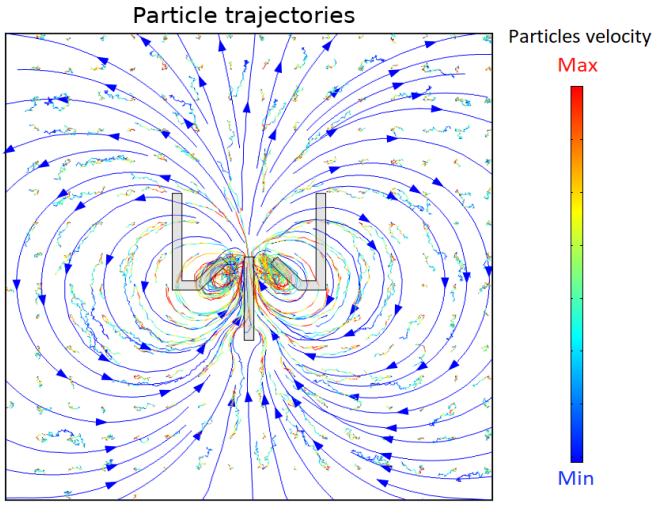

Figure 2.5 Simulation of particles tracing. *20 nm nanoparticles' trajectories are shown in response to the ACET fluid motion (blue lines with arrows) after 60 seconds of applying the ACET voltage.*

Here in Figure 2.5, we show how nanoparticles (20 nm radius), in resemblance to the small biochemical reagents, would react to the ACET fluid motion. These simulations consider the effect of the fluid drag forces on the microparticles by using the Stokes drag law, the effect of the temperature on the Brownian motion and the fluid dynamic viscosity, and finally the gravitational forces. It is clear from the particle's traces in Figure 2.5 that the microparticles inside the chamber follow the same direction as the fluid motion (blue lines/arrows) in response to the applied ACET voltage. Moreover, it can be seen from the concentrated (yellow to red) tracing lines at the center, that the microparticles located at that location will experience the largest ACET forces. This can be explained by the high electric field intensity and thus the maximum fluid velocity at that location.

2.4.2 ACET enhanced surface reaction (kinetics effect)

We have investigated the possibility of using the new in-plane vortex design for enhancing surface-based immunoassays (i.e., surface adsorption reactions) and studying the effects of experimental conditions, such as the association kinetic constant and the analyte concentration. At the beginning of the reaction during static incubation (low Péclet values), antigens in the target area start to consume the reagents available in their volumetric vicinity. After some time and depending on several factors, including the reaction kinetic rates and the reagent concentration, a depletion region is formed around the target area with much lower availability of the analyte reagent (as shown later). At this point, the reaction rate becomes limited due to the scarcity of the detection reagents and their

diffusion-limited transport (large Damköhler values). There are a variety of detection reagents (RNA, DNA, antibodies, aptamers, etc.) that can be used in different assays, and their diffusion time depends mainly on their size. Equation (2.12) shows the Stokes-Einstein relation [255] between the diffusion coefficient (D) and the particle radius (r), where (T) is the absolute temperature, (η) is the solvent viscosity and (k) is the Boltzmann constant.

$$D = \frac{kT}{6\pi\eta r} \qquad 2.12$$

Equation (2.13) shows the Einstein–Smoluchowski relation for the mean-square displacement of a diffusing particle,

$$x^2 = 2Dt \qquad 2.13$$

where x is the mean distance that a molecule with diffusion coefficient D will diffuse over time t. Here, we can see clearly that larger molecules will have a smaller diffusion coefficient and, as a result, would need longer times to diffuse over a given distance x. For instance, biological molecules such as antibodies and DNA have diffusion coefficients in the range of 10^{-11} to 10^{-12} m^2/s [92,93] and thus would need a diffusion time in the range of a few minutes to hours to travel across a distance of 100 µm, leading to long-time experiments. Here, the fluidic motion generated by the ACET clearly facilitates the transport of the analyte reagents inside the chamber and thus, enhances the replenishment of the reagent in the vicinity of the reaction surface.

Figure 2.6.a shows the enhancement in the surface adsorbed species (mol/m^2) over a surface reaction area (circle with 100 µm radius) positioned at the center of the in-plane electrode design, as shown in Figure 2.4.b, for different applied voltages (V_{pp}) and different association constants K_{on} ($m^3/(s.mol)$ and

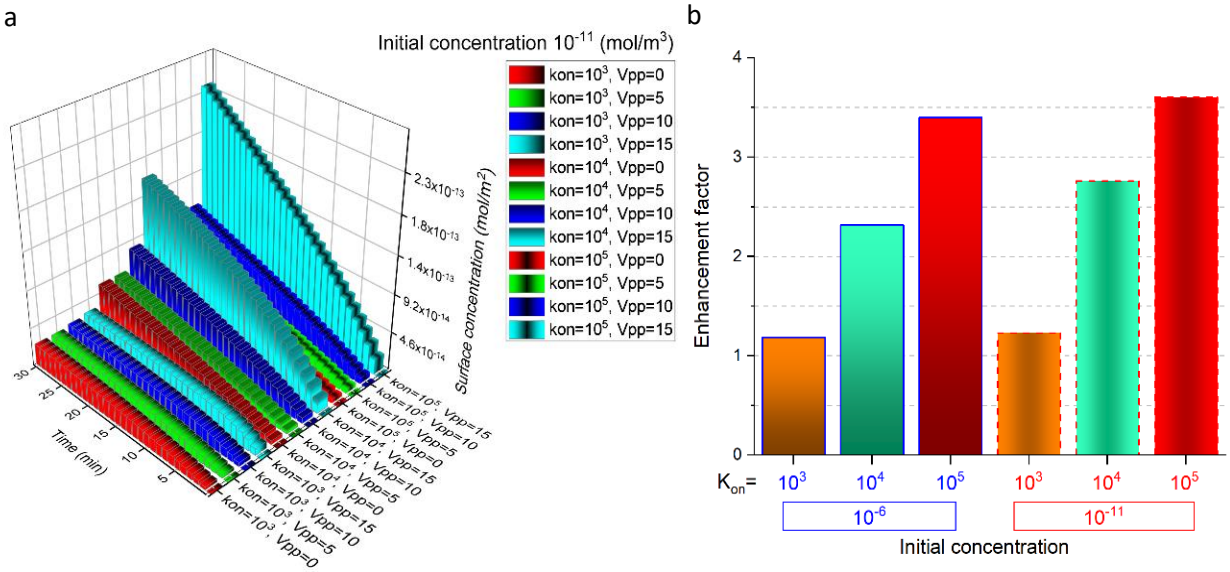

Figure 2.6 Simulation of surface binding of reagents to the target antigens. *(a) Enhancement in the surface-bound species (mol/m^2) as a result of the ACET flow over a surface reaction area (circle of 100 µm radius centred at the tips of the 3 electrodes) at for different applied voltages (0, 5, 10, 15 V_{pp})) and different association constants Kon (10^3, 10^4, and 10^5 ($m^3/(s.mol)$) at an initial analyte concentration inside the chamber of 10^{-11} (mol/m^3). (b) Enhancement factor for t= 30 minutes of the surface-bound species (15 V_{pp}/0 V_{pp}) at the different association constants, and at an initial analyte concentration inside the chamber of 10^{-11} and 10^{-6} (mol/m^3).*

after a reaction time of 30 (minutes). It is clear that for a given association constant and with higher voltages (for example 15 V_{pp} vs 0 V_{pp}), the concentration of surface-bound reagent species is higher. This is mainly due to the increase in velocity of the generated ACET fluid motion and thus, faster replenishment of the analyte in the vicinity of the surface reaction area. Additionally, it shows that the ACET mixing effect at higher voltages can shorten the reaction time needed for immunoassays while obtaining higher detection signals. Moreover, it shows that for a given voltage (for example 15 V_{pp}, Cyan color), the enhancement in the surface-bound concentration is lower for lower association constants, as the kinetic rate of the reaction, in this case, is the limiting factor. Therefore, there is a small room for improvement by mixing in the surface adsorbed species concentration (i.e., fluorescent detection signal) of biochemical reactions that have slow kinetic rates (i.e., small association constants). Figure 2.6.b shows the enhancement factor defined by the enhanced surface concentration mol/m^2 obtained at 15 V_{pp} over a surface concentration obtained at 0 V_{pp} (without ACET mixing), for an initial analyte concentration inside the chamber of 10^{-6} and 10^{-11} (mol/m^3) at 30 minutes, respectively. This shows that the enhancement is higher for the lower (10^{-11} mol/m^3) analyte concentration. This is mainly due to the scarcity of the analyte in the vicinity of the immobilized target, rendering the ACET microfluidic mixing more helpful in the replenishment of the analyte. In contrast to that, with high analyte concentration (10^{-6} mol/m^3), there is an abundance of the analyte and thus, the ACET mixing enhancement is limited.

2.4.3 Comparison of in-plane versus vertical vortex design (simulation)

The ACET technique has been studied in the past using the parallel electrodes configuration, where a pair of electrodes (or an array of electrode pairs) with specific width and an interspacing gap is located at the top/bottom of a microfluidic channel.[90,163,167,172,235,236,247,256–258] The actuation of the electrodes

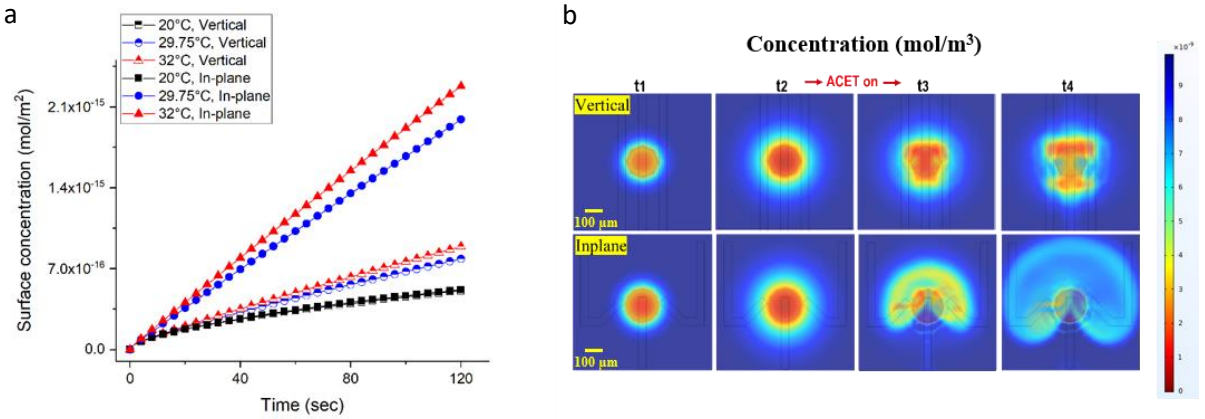

Figure 2.7 Comparison of the in-plane versus the vertical vortex design for enhancing surface-based assays. *(a) Surface-bound species (mol/m^2) as a function of reaction time as a result of the ACET flow for the in-plane and the vertical vortex design at three different temperatures (20 °C, 29.75 °C, and 32 .0 °C). The association constant is 10^4 (m^3/(s.mol) and the initial analyte concentration inside the chamber is 10^{-8} (mol/m^3). (b) Development of the depletion region during the reaction. The depletion region was allowed to form until time (t2=24.983 min), and the ACET actuation was only applied at time (t3=25.183 min) to show how both designs would mix and replenish the analyte concentration above the central region (t4=25.683 min).*

with the AC electric field generates counter-rotating fluidic vortices in the z-direction above the electrodes' surface. This can help enhance the surface-based reaction by stirring the fresh analyte concentration and replenishing the depletion region formed over the target sample. The ability of the parallel electrode design to mix and thus enhance the surface reaction is limited by the temperature that can be generated not to degrade the biomolecules. Also, a high electric field can lead to electrolysis and the formation of bubbles.[163] It has been reported that high ACET voltages applied to a 0.5 S/m conductive solution (1/3 of buffer conductivity used in the current work) would indeed lead to electrolysis and bubbles.[240] Moreover, the stability and functionality of the bioreagents can be sensitive to high temperatures.[241,242] Here we show the ability of the new in-plane vortex design to enhance the analyte concentration replenishment by obtaining a large in-plane volumetric mixing. We have carried out a comparison of the performance of the in-plane design versus the vertical vortex design. As previously discussed in the theoretical section, the ACET-induced flow and thus the mixing enhancement is defined by the electric field and the resulting temperature profile. Both variables are highly dependent on the microelectrodes' design and operation. Therefore, to highlight the role of ACET-induced transport when comparing the in-plane and the vertical designs, the generated average temperature in the volume centered around the electrode gaps was kept the same for both designs. Our in-plane vortex design has 50 µm wide electrodes with the two side electrodes spaced 85 µm and tilted 45° against the middle electrode. Similarly, our classical vertical vortex design has 50 µm wide electrodes spaced 85 µm against the middle electrode at a 90° angle. A full comparison of the fluidic streamline vortices of the in-plane and vertical designs is shown in Figure 2.15. Figure 2.7a shows the simulation results of the enhancement of the surface adsorbed species by the in-plane and vertical vortex electrode designs at the same volumetric average temperature. This shows that the in-plane vortex design enhances the surface reaction better than the vertical vortex design. This is further confirmed by Figure 2.7b, which shows a time series of bulk analyte concentrations obtained by mixing using the two designs. The depletion region over the reaction surface located at the bottom of the chamber (Figure 2.4.b) is allowed to form initially (t1 to t2), and thereafter the ACET actuation was applied (t3). The period (t3 to t4) shows how both designs can replenish and direct the fresh analyte molecules to the reaction surface. Additionally, it shows that the semi-circular in-plane vortices resulting from the new in-plane electrode design result in a larger mixing area (meaning a higher surface reaction) as compared to the parallel vertical design. A similar extent of the in-plane fluid mixing is observed by experiments (Figure 2.4.c).

2.4.4 ACET-enhanced immunoassays (experimental)

Experimental verification was carried out to compare the two designs using the immunoassay protocol described in the Methods & protocols section 2.6. Briefly, BT-474 cancer cell pellet sections were incubated with rabbit primary anti-HER2 antibodies and then anti-rabbit secondary antibodies conjugated with biotin molecules. Then, the sections were incubated with streptavidin molecules conjugated with 647 fluorescent dyes. ACET was applied only during the primary and secondary antibodies incubation. Finally, the sections were mounted and imaged using an automatic fluorescent scanning system. The signal (S) and background (B) values of the ACET (area located below the ACET

electrodes) and non-ACET (far away from the electrodes) cell fluorescent spots were measured and analyzed, as explained in the Methods & protocols section 2.6. The average (n=3) enhancement factor due to the ACET mixing over static reaction (non-ACET) was calculated using the following equation (2.14), where τ is the exposure time of the fluorescence excitation signal used in the experiment:

$$\boldsymbol{Enhancement\ factor} = \frac{\left((S-B)/\tau\right)_{\boldsymbol{ACET}}}{\left((S-B)/\tau\right)_{\boldsymbol{non-ACET}}} \qquad 2.14$$

A schematic of the corresponding locations of the ACET and non-ACET spots within the microfluidic chamber and in relation to the ACET electrode`s design is shown in detail in Figure 2.8.

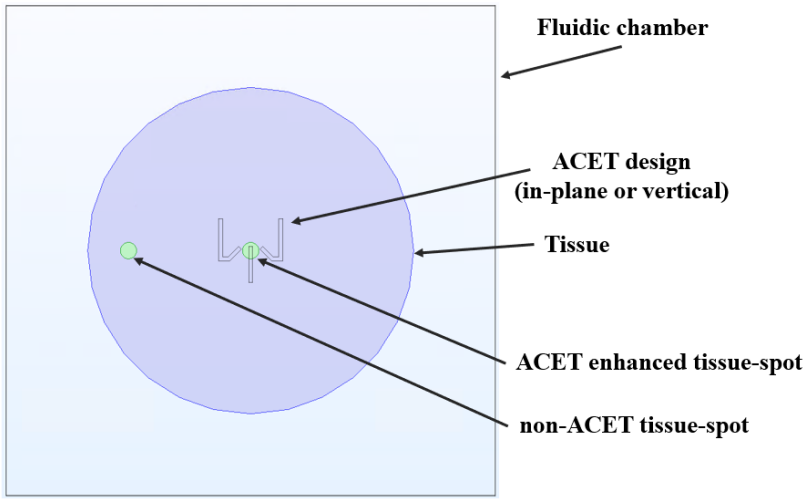

Figure 2.8 Schematic representation of the microfluidic chamber with the cell pellet or tissue section and ACET mixing design used for the experimental validation of the ACET-enhanced immunostaining. *The ACET mixing design (shown here is the in-plane design, but similarly a vertical electrode design can be imagined) with the BT-474 breast cancer cell pellet (tissue) located at the bottom of the chamber. Two spots were considered for the subsequent analysis, namely a ACET-enhanced tissue spot for the area located below the ACET designs, and another spot (non-ACET tissue spot) located at least 1~2 mm far away.*

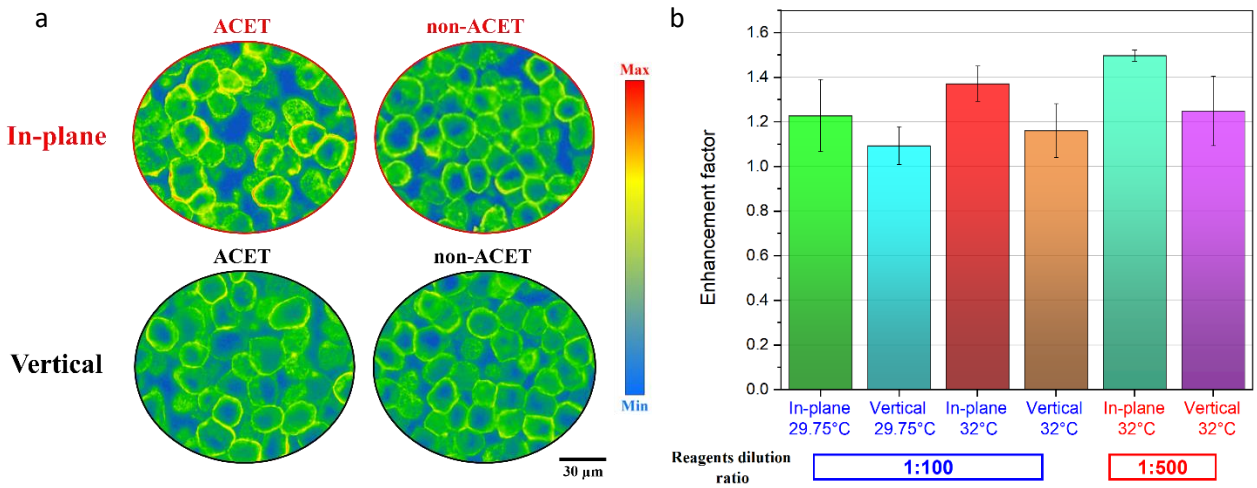

Figure 2.9 Experimental validation for the ACET immunostaining enhancement using the in-plane and vertical vortex designs. *(a) Gradient map images of the in-plane and vertical vortex enhanced fluorescent immunostaining on BT-474 cells. (b) Enhancement in the HER2 staining signal using the in-plane and vertical designs at two different average volumetric temperatures of 29.75 °C (1:100 dilution of primary and secondary antibodies) and 32.0 °C with (1:500 dilution of primary and secondary antibodies).*

Figure 2.9.a shows representative gradient map images of the BT-474 cells' immunostaining signal for the in-plane and vertical vortex ACET-enhanced mixing versus the unenhanced (non-ACET) images. Here, the HER2 signal is enhanced in the ACET versus the non-ACET images and is more prominent in the cellular membrane. Figure 2.9.b shows the average enhancement of immunofluorescent staining at the ACET mixing location over the normal non-ACET incubation. It shows that both designs, tested at two different temperatures, enhance the immunofluorescent reaction by replenishing the analyte concentration, especially when using higher voltages, as explained before. Furthermore, it shows that the in-plane vortex design can further enhance the immunoreaction due to its improved mixing ability. In parallel to that and as shown by simulation (Figure 2.6.b), with a higher dilution of the reagents, there is more scarcity of the analyte in the vicinity of the immobilized target, and thus the ACET mixing can be more effective for enhancing the immunoreaction. This is shown by the results (Figure 2.9.b) of the ACET mixing using the two designs with 1:500 dilution of primary and secondary antibodies. The in-plane and vertical design improved the immunostaining by 49.7% and 24.8%, respectively, which is higher than the performance of the same designs at the reagent's dilution ratio of 1:100. This shows the potential of using the new in-plane design for enhancing the outcome of chemical and bioassays.

2.4.5 Improved in-plane design: scaling-up

After validating the in-plane concept of design, and while it was seen that the in-plane design is capable of mixing the fluid over a larger area, we further investigated the concept of scaling up the design. The strategy was to enable the fluid agitation by the ACET motion over a larger area and thus enhance the fluid flow over the sectioned cells' surface. In case the parallel electrodes` design is used, additional parallel electrodes would be required to mix over a larger area, possibly compromising

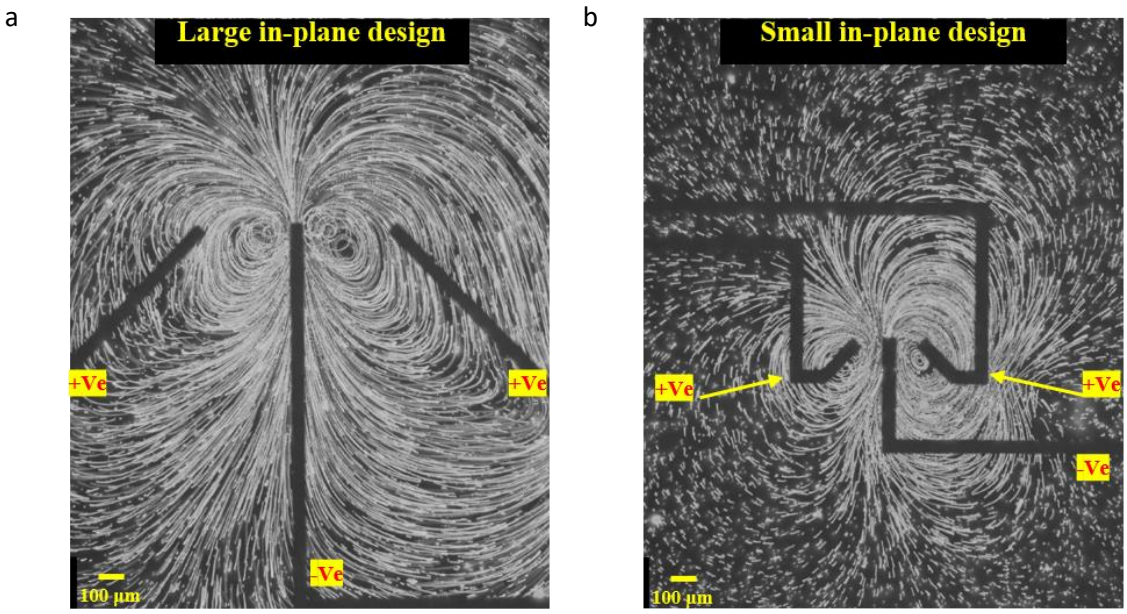

Figure 2.10 The in-plane ACET motion obtained by the large (a) and small (a) in-plane designs*. The figures show the superimposed images of a time sequence of fluorescent microparticles moving along with the ACET in-plane vortices. A similar number of frames (300 frames) were used to generate the images.*

imaging accessibility. So, here we scaled up the in-plane design by extending the two side electrodes (200 µm to 1000 µm) and the middle electrode (450 µm to 1500 µm) and increased the gap between the electrodes from 85 µm to 340 µm. Here in Figure 2.10, we show the different ACET mixing coverage areas by the large (Figure 2.10a) and small (Figure 2.10b) in-plane designs, obtained after superimposing a similar number of frames and while actuating both designs with the maximum possible ACET power (that at which, it was still safer to avoid bubbles and electrolysis). It shows clearly that the large design can induce ACET in-plane fluid motion over a larger area.

Additionally, Figure 2.11 shows the maximum temperature obtained by the small and large in-plane designs at 30 Vpp and with fluid conductivity of 1.5 S/m. The large design shows a lower maximum

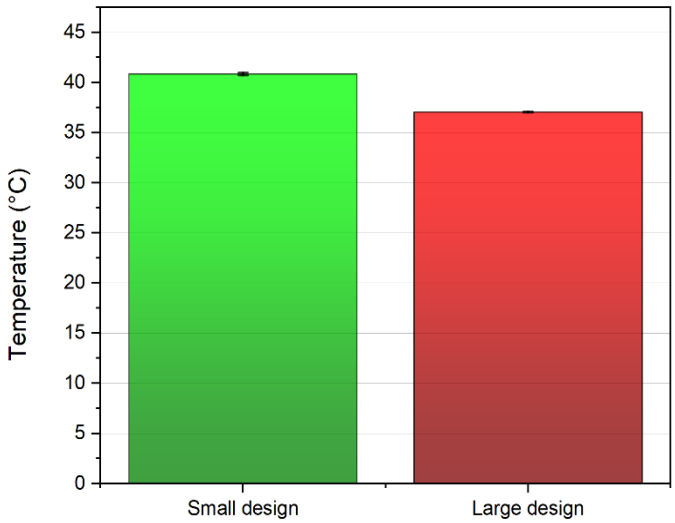

Figure 2.11 The maximum temperature measured by the thermal IR camera during the ACET actuation of the small and large in-plane designs at 30 Vpp and 1 MHz. *Error bars represent the standard deviation (n=4).*

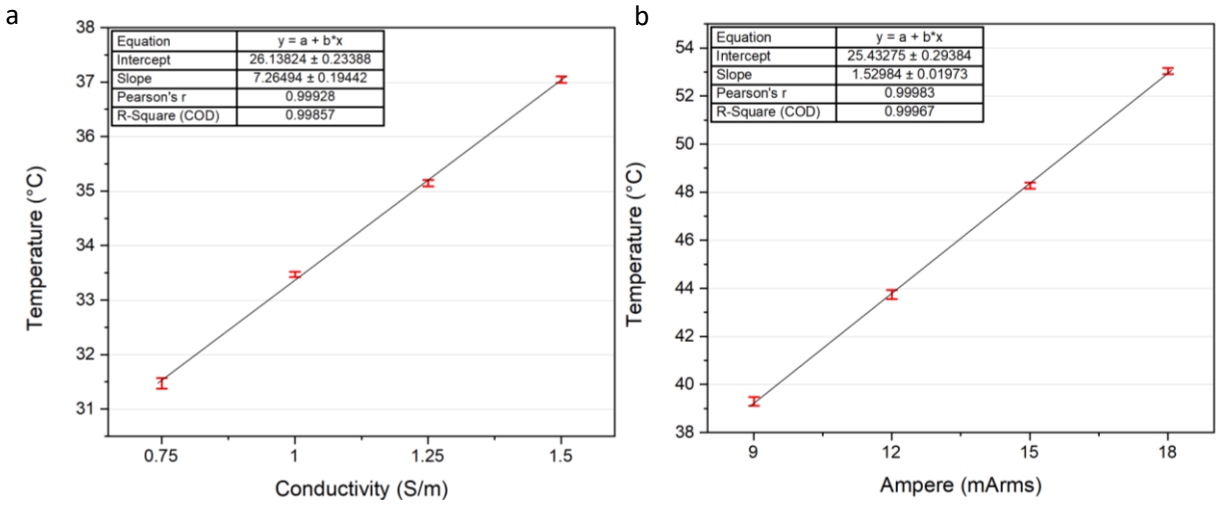

Figure 2.12 The maximum temperature measured by the thermal IR camera *during the ACET actuation of the large in-plane design for (a) different fluid conductivities (S/m) at 30 Vpp 1MHz and (b) different ACET power (electrical current (mArms)) using a fluid conductivity of 1.5 S/m. Error bars represent the standard deviation (n=4).*

temperature than the small design. This is partially due to the increased gap between the two side and middle electrodes (340 µm vs 85 µm for the small in-plane design). Moreover, the large in-plane ACET actuation was tested with several fluids with different electrical conductivities (0.75 to 1.5 s/m) at 30 V_{pp} 1 MHz. The results (Figure 2.12a) show a linear correlation between the temperature and the conductivity (Pearson's product-moment correlation coefficient= 0.99). Moreover, the maximum obtainable temperature was measured as a function of ACET actuation current (9 to 18 mArms) using the large in-plane design (Figure 2.12b). The design shows a linear relationship between the ACET current and the achieved temperature (Pearson's product-moment correlation coefficient =0.99). In general, increasing the conductivity of the solution or the current (power) would lead to an increase in the generated ACET forces and the resulting microfluidic mixing. Higher currents than those reported here would then lead to too high temperatures, leading to the generation of bubbles and possibly electrolysis.

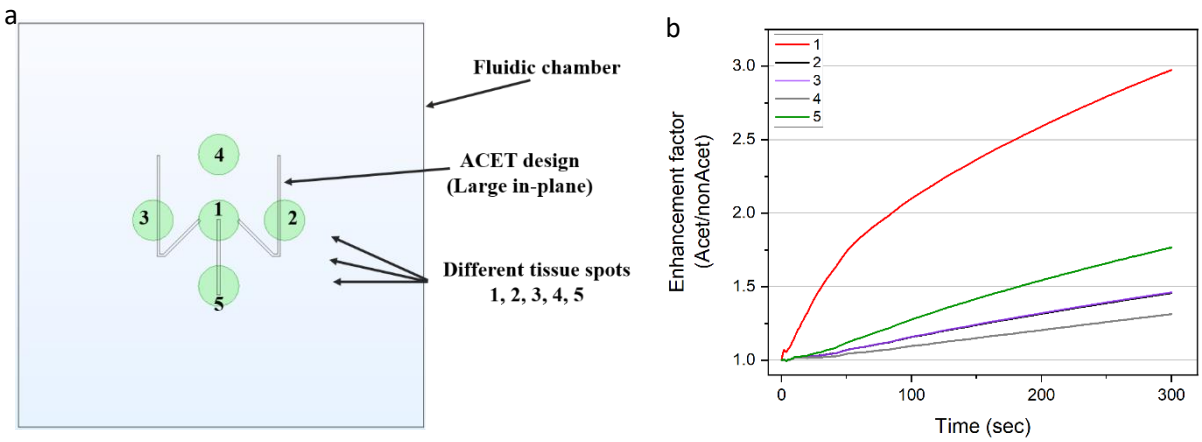

Figure 2.13 Schematic representation of the microfluidic chamber with the large in-plane design and theoretical simulation of the position-dependent ACET- enhanced surface reaction. *(a) The large in-plane electrode design located within a microfluidic chamber and locations used for calculating the ACET-enhanced surface reaction (1: centre, 2: right, 3: left, 4: top, 5: bottom of the design). (b) Enhancement factor for t= 5 minutes of the surface-bound species (25 Vpp/0 Vpp) for the different surface reaction spots indicated in Figure 2.13.a.*

In addition to that, we have simulated how the location of the surface reaction spots in relation to the in-plane design can be affected by the ACET enhancement to different extents, as compared to the static non-ACET incubation, as shown in Figure 2.13. It was found that the areas located close to the design center experience the highest enhancement in the surface reaction. This is mainly due to the close gap between the electrodes at that location and thus the strongest ACET forces. This is further supported by the dense microparticle trajectories located at the design center as seen in the experiment (Figure 2.4). The bottom spot (5) shows a higher enhancement than the right (2) and left (3) and top (4) spots, probably due to the ability of the design to drag and push the fluid from the bottom stronger than from the other locations, resulting in a higher enhancement.

After validating and characterizing the large in-plane design, we have investigated the application of the design for further enhancing the immunoassay performance. Figure 2.14a shows the

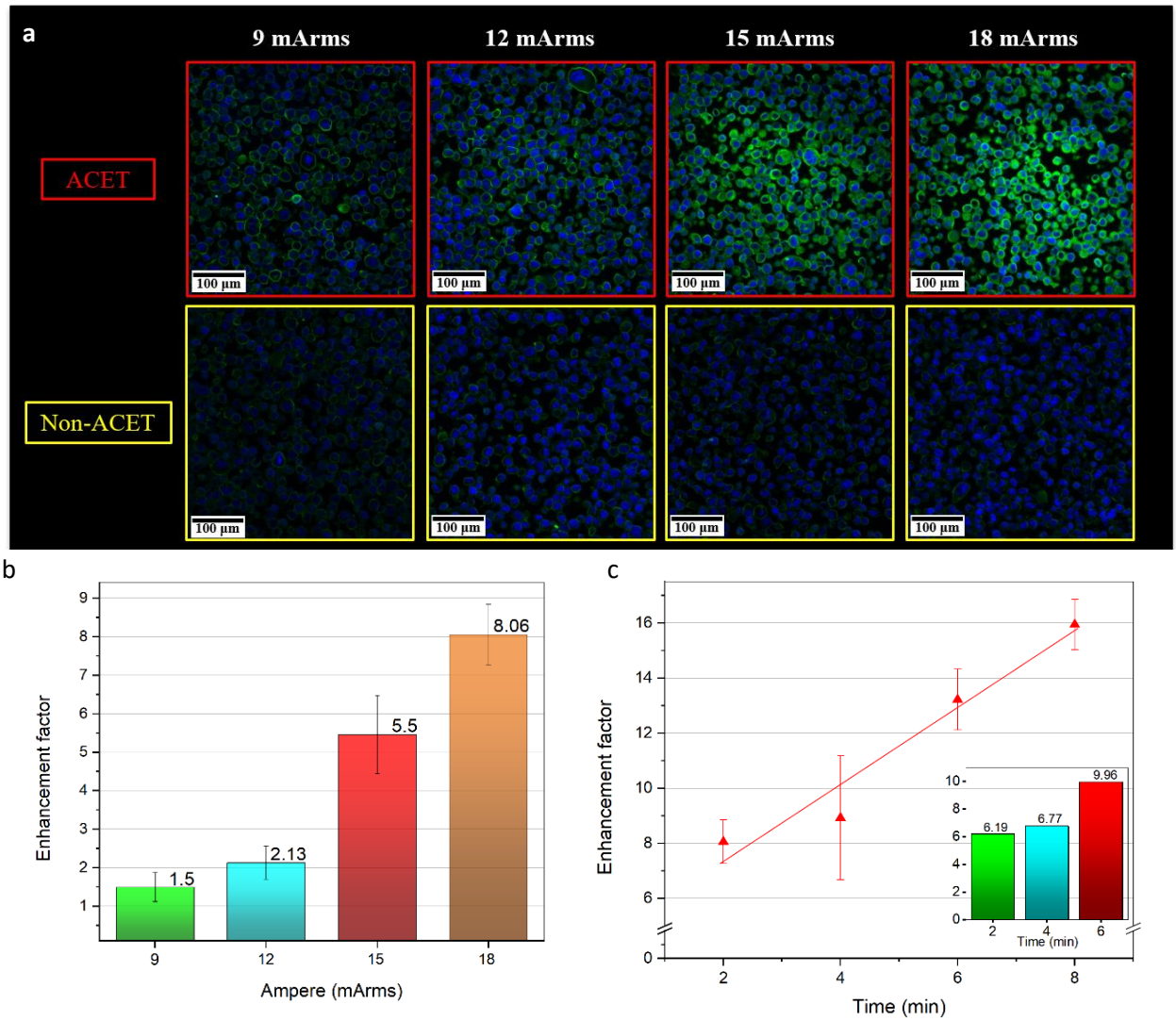

Figure 2.14 The ACET immunostaining enhancement using the up-scaled in-plane design. *(a) Representative images of the ACET enhanced and the non-ACET (static incubation) immunostaining of BT-474 cancel cells using the up-scaled in-plane design at different ACET power (electrical current 9 to 18 mArms). Blue colour is the cell nuclei counterstaining (DAPI) and the green colour is the HER2 signal. (b) Enhancement in the HER2 staining signal using the up-scaled in-plane design at different ACET power for 2 minutes. (c) Enhancement in the HER2 staining signal using the up-scaled in-plane design for different incubation times (2 to 8 minutes) at an ACET power of 18 mArms. The inset plot of figure (2.14.c) shows the enhancement of the HER2 signal with 2, 4, and 6 minutes of ACET mixing over the non-ACET (static incubation) staining with 8 minutes. Error bars represent the standard deviation (n=3).*

enhancement in the BT-474 cells immunostaining at different ACET power. It shows an increased HER2 signal (green color) with the increasing ACET power due to the increased fluid mixing and the larger volumes being replenished over the assay's reactive surface. The images shown in Figure 2.14a are the spots with the highest observed enhancement in the HER2 signal, which is usually the area located below the center of the electrodes' design. Figure 2.14.b shows the analysis of the immunostaining enhancement factor as described before and using equation (2.14) at different ACET power from 9 to 18 mArms. It shows enhancement factors of up to 5.5 and 8 can be achieved with 15 and 18 mArms respectively, while even the lowest power used (9 mArms) can still achieve a higher signal than the non-ACET reactive surface (static incubation). Moreover, with higher ACET power, the area affected by the enhanced ACET mixing is larger due to the stronger ACET forces and thus the fluid is agitated over larger areas. We believe that this would be practically useful for applications with large microfluidic chamber sizes and large samples, and in case maximum microscopic imaging accessibility is desired. It is worth noting that when higher ACET power (in the range of 18~20 mArms) was used, bubbles were generated due to the high temperatures and possibly electrolysis. Figure 2.14.c shows the analysis of the HER2 immunostaining enhancement factor for different incubation times, ranging from 2 to 8 minutes. It shows that enhancement factors of up to 13.2 and 15.9 can be achieved with 6 and 8 minutes of incubation respectively. Thus, with longer ACET actuation times, a further enhancement can be achieved. The inset plot of Figure 2.14.c shows the enhancement obtained with the ACET actuation for 2, 4, and 6 minutes over the static incubation (non-ACET) obtained after 8 minutes $[(S\text{-}B)_{ACET\ (2,\ 4,\ 6\ min)}/(S\text{-}B)_{non\text{-}ACET\ (8\ min)}]$. It shows that the incubation times can be shortened from 8 minutes down to 2 minutes (75% reduction in time) while still achieving a 6 times higher signal. This can be valuable for reducing the experimental assay times and having faster diagnostics.

2.5 Conclusion

In conclusion, this chapter presents a novel concept for improving biochemical reaction rates in microfluidic systems through AC electrothermal flow (ACET) using a new electrode design for generating an in-plane microfluidic mixing vortex. Unlike traditional ACET parallel electrode designs that provide local vertical mixing vortices, the proposed design generates vortices that act over a large volume close to the reaction surface of interest, as validated through numerical simulations and experimental studies. The effects of experimental factors such as reaction kinetics and reagent concentration on ACET-enhanced surface-based assays were also investigated through numerical simulations. The proof-of-concept experiments demonstrated the improved immunostaining signal of the HER2 cancer biomarker on breast cancer cells using the new ACET-enhanced immunoassay design. Furthermore, scaling up the design was validated through experiments with different ACET power and assay times, showing that larger in-plane ACET designs can effectively agitate and mix the fluid over large microfluidic volumes, resulting in enhanced immunoassay outputs. These findings highlight the potential of the proposed ACET electrode design concept for addressing the limitations of diffusional transport in microfluidic systems and improving the performance of immunoassays for various applications.

2.6 Methods & protocols

2.6.1 Supporting results

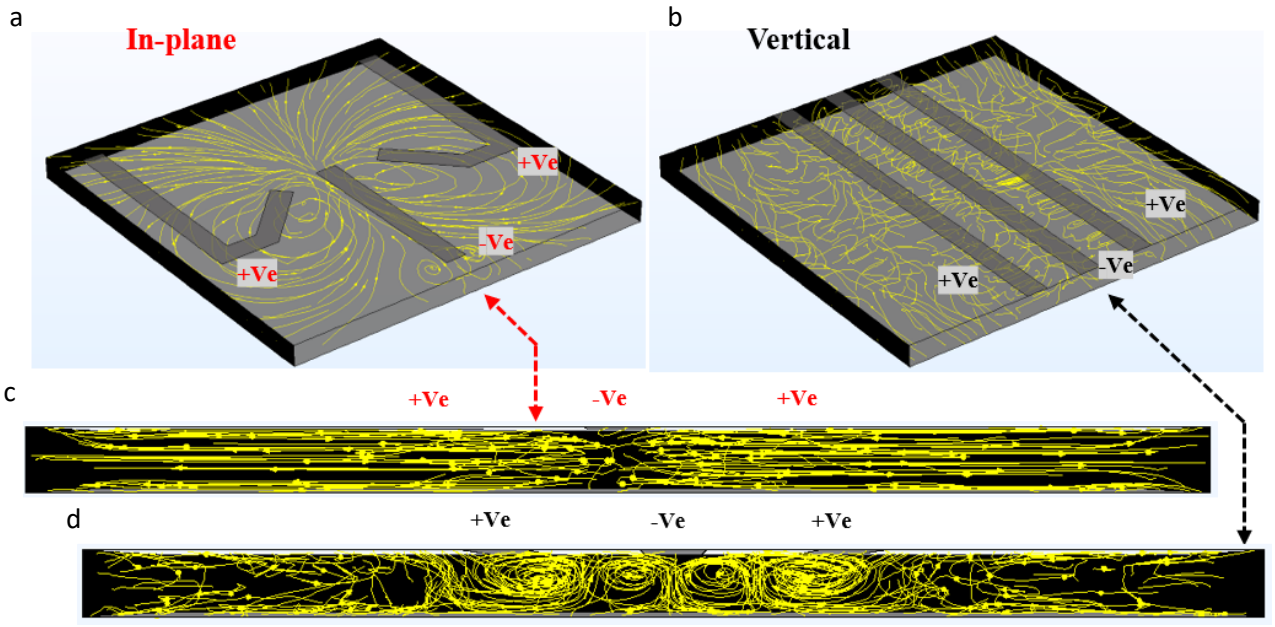

Figure 2.15 Numerical simulation comparison of the fluidic streamlines of the in-plane and vertical vortices designs. *(a) 3D view and (c) the corresponding side view of the fluidic streamlines generated by the ACET actuation of the in-plane vortex design. (b) 3D view and (d) the corresponding side view of the fluidic streamlines generated by the ACET actuation of the vertical vortex design. Both designs have 50 µm wide electrodes and 85 µm interspacing gap between each of the two side electrodes and the middle electrode.*

Here in Figure 2.15, we show how the ACET actuation of the in-plane (Figure 2.15.a) and vertical (Figure 2.15.b) vortex designs generate different fluidic streamlines. The in-plane design vortex generates in-plane fluidic motion, while the traditional vertical design with parallel electrodes generates a local vertical vortex fluidic motion. This is further confirmed by Figure 2.15.c and Figure 2.15.d, which show the fluidic streamlines from the corresponding side view of the microfluidic chamber for the in-plane and vertical vortex design, respectively. It can be seen clearly that the in-plane design is capable of inducing a large-scale fluidic motion across the width of the chamber. The vertical design shows two vertical vortices mainly localized at the center of the chamber between each of the two side electrodes and the middle electrode.

2.6.2 Numerical simulation protocol

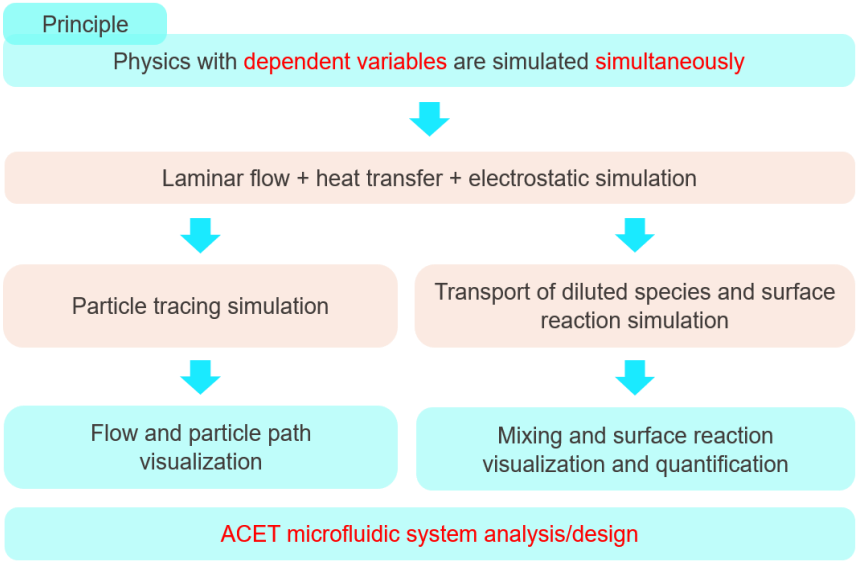

Figure 2.16 Pipeline of the numerical simulation strategy for solving the laminar flow, heat transfer, electrostatics, particle tracing, transport of diluted species, and surface reaction problems.

Table 2-1 Values of the numerical simulation variables

Variable	Value	Description
ω	2*π*1e6 [Hz]	Angular frequency of the AC signal
V0_rms	Vpp/(2*sqrt(2))	V_{RMS} (Volt root mean square) of the V_{pp} (Volt peak to peak)
T_0	293.15 [K]	Reference ambient temperature
$\frac{1}{\varepsilon}\frac{\partial \varepsilon}{\partial T}$	-0.004 [1/K]	Permittivity ratio change per Kelvin
$\frac{1}{\sigma}\frac{\partial \sigma}{\partial T}$	0.02 [1/K]	Electrical conductivity ratio change per Kelvin
σ	1.5 [S/m]	Solution electrical conductivity
length	15 [mm]	Microfluidic chamber length
width	15 [mm]	Microfluidic chamber width
width_el	50 [um]	Electrode width
gap_el	85 [um]	Gap between electrodes
r_particle	20 [nm]	Particle radius used in the particle tracing study
c_0	1e-6 to 1e-11 [mol/m^3]	Initial analyte concentration
kon	1e3 to 1e5 [m^3/mol/s]	Association reaction constant
Kd	1e-2 [1/s]	Dissociation reaction constant
B0	3.3e-8 [mol/m^2]	Surface target (bioreagent) density

Table 2-2 Boundary conditions for the numerical simulations

Boundary	Electrical boundary condition	Thermal boundary condition	Fluidic boundary condition	Transport of diluted species (tds) boundary condition	Surface reaction (sr) boundary condition
Top surface	Zero charge[1]	Natural convection[2]	–	–	–
Side walls	Zero charge[1]	Side-wall natural convection[2]	–	–	–
Bottom surface	Zero charge[1]	T_0	–	–	–
Electrode surface	$V_{0,RMS}$	–	Wall, no slip[3]	No flux[5]	–
Counter electrode surface	$-V_{0,RMS}$	–	Wall, no slip[3]	No flux[5]	–
Chamber top surface	–	–	Wall, no slip[3]	No flux[5]	–
Chamber side walls	–	–	Open boundary[4]	Open boundary[6]	–
Chamber bottom surface	–	–	Wall, no slip[3]	No flux[5]	–
Reacting surface	–	–	Wall, no slip[3]	Outward flux due to surface reaction[7]	Surface reaction[8]

1 $\hat{n} \cdot \vec{D} = 0$

2 $q_0 = h(T - T_0)$, *where* T *and* T_0 *are the temperature and the reference ambient temperature*

3 $\vec{u} = \vec{0}$, *where* u *is the fluid velocity*

4 $p = 0$, *where* p *is the pressure*

5 $-\hat{n} \cdot (\vec{J} + \vec{u}c) = 0$

6 $\begin{cases} -\hat{n} \cdot \vec{J} = 0, & if\ \hat{n} \cdot \vec{u} \geq 0 \\ c = c_0, & if\ \hat{n} \cdot \vec{u} < 0 \end{cases}$, *where* c *is the reagent concentration*

7 $\frac{\partial [A]}{\partial t} = -\left(k_{on}[A]_{surface}\{[B_0] - [AB]\} - k_d[AB]\right)$

8 $\frac{\partial [AB]}{\partial t} = k_{on}[A]_{surface}\{[B_0] - [AB]\} - k_d[AB]$

2.6.3 Immunoassay protocols

Preparation and blocking:

A BT-474 FFPE cell pellet block (Amsbio) was sectioned into 5 µm thick slices and loaded on Superfrost Plus adhesion microscopic slides (Epredia). Before the immunostaining, the cell pellet sections were dewaxed and deparaffinized using the PT module (Epredia) for 1 hour into the Dewax and HIER Buffer H (PH 9) at 102 °C. After that, the slides were kept in TBST (Tris-buffer saline with 0.005% tween-20) until the blocking step. The slides were then quenched for 2 minutes with Quenching buffer 1x (BU08-L, Lunaphore) diluted into TBS buffer (Tris-buffer saline). The slides were then washed thoroughly with TBST and then incubated for 5 minutes with bovine serum albumin (3%, AURION BSA-c, diluted in staining buffer). Finally, the slides were washed thoroughly with TBST and used for the endogenous biotin-blocking step. A streptavidin/biotin blocking step was carried out to reduce any nonspecific signal coming from endogenous biotin or streptavidin binding sites present in the cells. The cell sections were incubated with a streptavidin-blocking solution for 15 minutes, then washed with TBS for 3 minutes, and then incubated with the biotin-blocking solution for 15 minutes, followed by 9 minutes of washing with TBS. The streptavidin blocking step would block the endogenous biotin, while the biotin blocking step would block the free binding sites available on the streptavidin molecule. Finally, the slides were kept in TBS till the immunostaining step.

Immunostaining:

The slides were then loaded into the microfluidic system shown in Figure 2.1 and the following bioassay protocol was used for all the slides. The BT474 cell sections were first incubated with a Her2/Neu (EP3) rabbit monoclonal primary antibody (237R-25-ASR, Cell marque) diluted into TBST for 2 minutes. The slides were then washed thoroughly with TBST and subsequently incubated for 2 minutes with a Goat anti-rabbit IgG (H+L) Highly Cross-Adsorbed secondary antibody-Biotin (A16114, Thermofisher). The primary and the secondary antibodies were diluted 1:100 into a 1.5 S/m multi-staining buffer, and the ACET actuation was applied during their incubation. Dapi (62248, Thermofisher) was diluted to 1:1000 with the secondary antibody and used for nuclear counterstaining. All the reagents handling (dispensing into the microfluidic chamber and fluid aspiration) and flow rate control were done with an automatic pressure pumping system integrated with the experimental setup. After washing thoroughly with TBST, the biotin conjugation on the secondary antibody allowed for the final step of binding the streptavidin molecules conjugated with the Alexa Fluor™ 647 label (S32357, Thermofisher). The Streptavidin-Alexa Fluor™ 647 label was diluted 1:200 into TBST and incubated for 2 minutes without applying any ACET actuation with the small in-plane design and with ACET actuation for the large in-plane design. The slides were then washed thoroughly with TBST and unloaded from the microfluidic stainer system.

Fluorescence microscopic imaging and analysis:

Finally, the slides were mounted with coverslips using the SlowFade Gold mounting medium (S36936, Invitrogen) for microscopic imaging. The slides were imaged using the PANNORAMIC MIDI II automatic slide scanner (3DHISTECH) with SOLA Light illumination engine (Lumencor). The focal level was adjusted for each imaging tile, and the whole cell-pellet section was imaged using a 20x (NA 0.8) objective. The exposure time was adjusted for each slide to avoid over- or under-exposure of the cell sections, and the different exposure times were considered during the image analysis. A similar region-of-interest (ROI) size for all the images was exported and analyzed using a CellProfiler (4.2.1) pipeline. Briefly, an adaptive Otsu thresholding was used to classify the her2 signal for each cell and assigned it as Signal (S), and the inverse of the mask was used as Background (B) to account for any fluorescent signal coming from outside the cells. For the visualization of ACET fluidic streamlines, TetraSpeck Microspheres 1.0 µm (T7282, Thermofisher) were diluted in TBST and used for observing the ACET fluidic motion.

Infrared thermal imaging:

An infrared thermal camera (PI 640i, Optris), was used for the thermal monitoring at a frequency of 31 Hz during the ACET experiments and for the large ACET in-plane design characterization at different fluid electrical conductivities and different ACET power.

Fabrication of the micro-electrodes:

Preparation and resist coating:

High-precision 1.5H (18×18 mm^2) microscopic coverslips (LH22.1, Carl Roth) were used for the electrode's lift-off microfabrication process. The coverslips were first cleaned for 10 minutes into IPA (isopropyl alcohol) and dried using nitrogen air. After that, the coverslips were put on a hotplate at 100 C° for 3 minutes to have a dry surface. The coverslips were then coated with LOR-5A (Kayakuam) as a sacrificial resist at 2500 rpm and baked at 170 °C for 4:10 minutes. Later, the coverslips were coated with AZ-1512 HS (Microchemicals) at 2250 rpm and baked at 100 °C for 1.30 minutes. The slides were then left for 15 minutes in a humidity-controlled environment.

Laser exposure and resist development:

The coverslips were then exposed using the Maskless Aligner MLA 150 (Heidelberg Instruments) with 80 mJ/cm^2 using an h-line (405 nm) laser source. The coated coverslips were then developed using AZ-726 MIF (Microchemicals) for 1:10 minutes and thoroughly washed with deionized water.

Lift-off evaporation and resist stripping:

The coverslips were then plasma-cleaned with a Tepla 300 system (PVA TePla AG) for 30 seconds at 200 watts. We found this step to be essential to remove any contaminants left on the patterned surface that otherwise can lead to an unsuccessful lift-off process. Then, the metal evaporation was done by loading the coverslips on copper thermal plates to avoid temperature rise. Hereafter, the coverslips were coated with 30 nm of chromium (adhesion layer) followed by 200 nm of platinum.

After that, the resist stripping process was done by sonicating the coverslips for 5 minutes into 1165 Remover (Microresist) and then sonicating for 10 minutes into IPA. The electrodes are 50 µm wide with an 85 µm gap distance gap. Finally, the coverslips were mounted on the staining chip (Figure 2.1) using UV curable glue and wired as explained.

3 Systematic study of the in-plane AC electrothermal flow

- "Patent application EP 22207056.7 filed the 11.11.2022, not published yet, results are confidential"

Here, we show further investigations on the concept of the AC electrothermal flow using the new proposed in-plane design. We show how the variation of the design characteristics (the angle between the electrodes) can alter the generated in-plane microfluidic streaming. Moreover, we extend the concept of the tilted electrodes design used in the previous chapter, to investigate new designs that can generate different forms and coverage areas of the in-plane motion. In addition to that, the ability of the designs to generate four in-plane vortices has been investigated by numerical simulation and experiments. Finally, a new ACET design has been proposed and investigated for the potential microfluidic pumping applications where the fluid can be pumped over long distances without any hydraulic components or mechanically moving parts.

3.1 Numerical study of the in-plane ACET design

Here we elaborate further on the working concept of the new in-plane AC electrothermal flow designs. Figure 3.1 shows the parallel electrodes design (Figure 3.1a, 3.1b) leading to the vertical ACET fluidic motion above the electrodes, and the tilted electrodes design (Figure 3.1c, 3.1d) leading to the in-

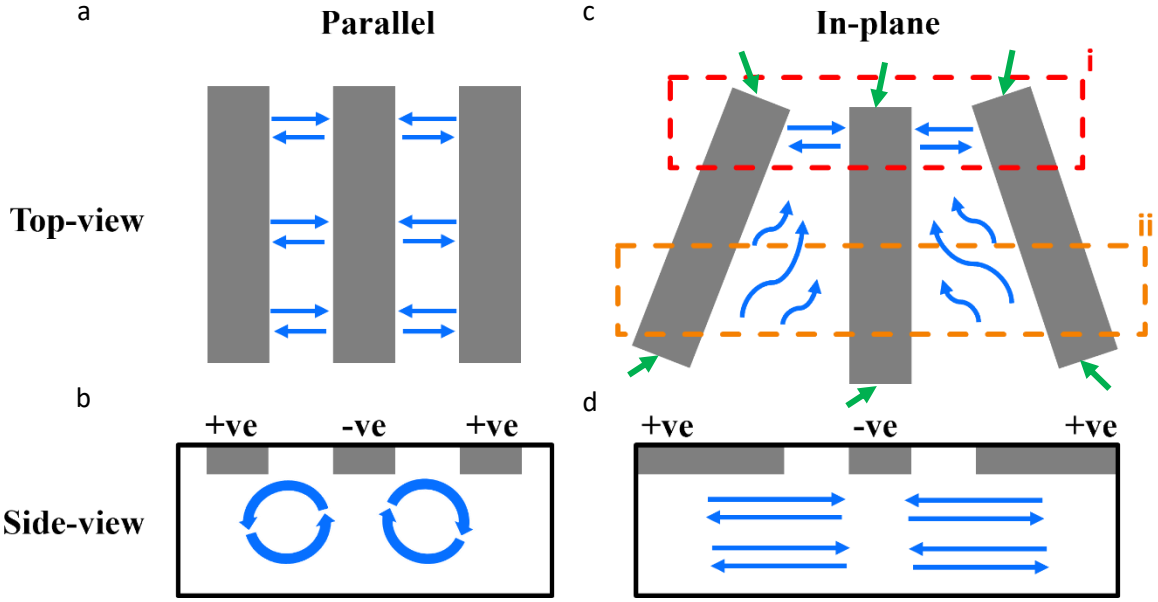

Figure 3.1 Schematics of electrode patterns giving rise to vertical and in-plane motion. *Parallel (a, b) and tilted (c, d) electrodes designs leading to the top-view (a, c) and side-view (b, d) of the fluidic motion under the actuation of the AC electrothermal flow. The electrodes are depicted in grey and are actuated by an AC voltage signal, they are located at the top of the microfluidic chamber. Dashed-line boxes (figure 3.ci and ii) represent locations inside the chamber, where there is predominantly vertical and parallel fluid motion in the chamber, respectively.*

plane ACET fluidic motion. The electrodes are located at the top of the fluidic chamber, as indicated in the previous chapter. The side view of the parallel electrode design (Figure 3.1b) shows vertical fluidic vortices above and between the oppositely-biased electrodes. This vertical fluid motion is the same along the electrode's length in the top-view (Figure 3.1a), except at the electrodes` ends. However, if we induce an angle between the electrodes, we create a different type of ACET-based flow pattern. Figure 3.1c shows the tilted electrodes design where area (i) would have a higher ACET effect than area (ii). This is mainly due to the smaller gap between the actuated electrodes in zone (i) versus the increasing gap between the electrodes towards zone (ii). Smaller gaps mean higher electric field intensities indeed and thus gives rise to higher ACET effects. The fluid in zone (i) would be agitated strongly in both the vertical and in-plane direction, and due to the fluid continuity, the fluid has to be supplied to that strong ACET spot. At the same time, zone (ii), despite having weaker ACET effects than zone (i), still experiences higher ACET effects than other locations far away from the actuating electrodes. The result is a pulling of the fluid from the sides of the design and pushing it towards the design centre, with predominance in the direction of the strongest ACET spots where there is the smallest gap between the electrodes. This behaviour would generate an in-plane vortex motion with the tilted electrodes design. Moreover, the non-parallel orientation between the top edges (short boundaries indicated by the green arrows in Figure 3.1b) of the side electrodes with their counterparts of the middle electrode, and the high electric field intensity at that position, can induce different propagation pathways for the electric field and the electric field charges responding to it. Finally, the high temperature generated and localized at the electrodes area with the small gap (e.g. zone i) might

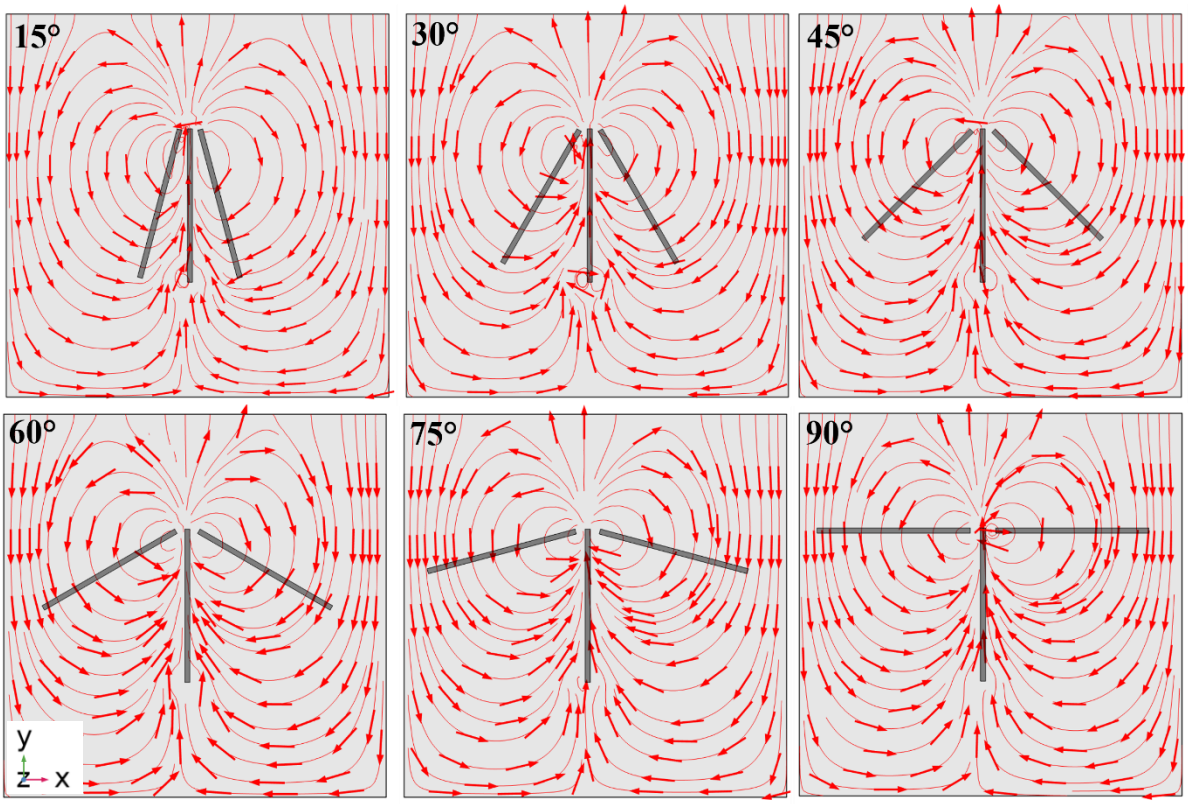

Figure 3.2 Tilted electrodes designs with different angels (from 15° to 90°) between the middle and two side and oppositely biased electrodes (top-view). *The electrodes are biased (two side electrodes vs the middle electrode) and the red streamlines show the resulting AC electrothermal fluidic motion and its direction, using numerical simulation. The fluidic chamber size is 3.8*3.8 mm² and the electrodes are 50 µm wide and 1.5 mm long.*

participate, in addition to the ACET mehancism of the distributed charges following the electrical field, in the fluid motion due to the thermal heat convection which can push the fluid from the warm to cold areas. However, it is important to note, that this thermal heat convection is not capable alone to agitate the fluid, without the ACET, as explaine later.

Our work in the previous chapter has shown the in-plane design with only a 45° angle between the middle and the two side electrodes. However, this angle can be varied while generating the reported in-plane motion, as shown in Figure 3.2. The numerical simulation approach, boundary conditions, variables, and the 3D geometry components from the previous chapter were adopted and used here. It can be seen, from Figure 3.2¸that starting from the smallest angle (15°), the system exhibits each time an in-plane direction of the fluidic motion under the actuation of the ACET. This motion is qualitatively similar for different angles between the electrodes, but with some different characteristics.

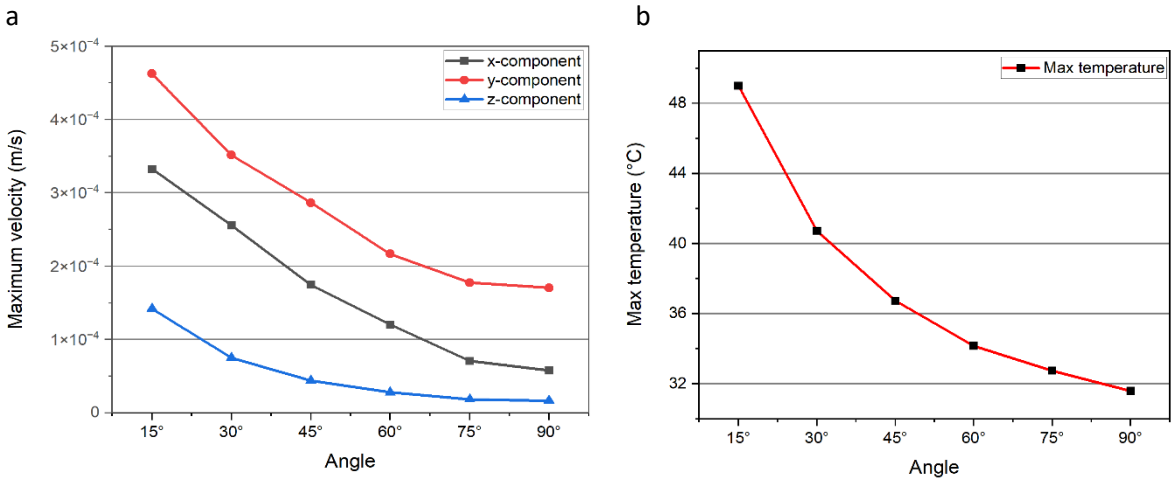

Figure 3.3 Maximum ACET velocity magnitude and the maximum temperatures for different angles between the middle and side electrodes. *(a) Maximum fluid velocity (m/s) in x, y, and z directions and (b) maximum temperature (°C) achieved under the ACET actuation at 20 Vpp – 1 MHz and for the different angles (15° to 90°).*

For example, increasing the angle between the electrodes would lead to a lower average electric field intensity, which means less strong ACET forces. This can be seen in Figure 3.3a, which shows the maximum ACET fluid velocity magnitude in the x, y (in-plane), and z (vertical) directions, for the different angles (15° to 90°) between the middle and side electrodes. The system shows lower fluid velocity magnitudes in all directions for an increasing angle. Moreover, the y component of the fluid velocity is sentimentally higher for the different angles followed by the x and z components. This indicated the domination of the in-plane direction of the fluid motion than the vertical direction. The associated electric field intensities are shown in Figure 3.3b, which shows lower maximum temperatures with larger angles. The applied electric field and the generated temperature due to the joule heating effect can be correlated using the energy balance equation (equation 2.1).

The temperature achieved can also be affected by other factors, including the thermal conductivity and the volume of the substrates and the fluid around the actuating electrodes. In addition to that, the electrodes` temperature can also play an important role in controlling the ACET fluid flow. Previous

research [259] has shown the concept of thermally biasing asymmetric opposite electrodes by connecting copper foils to the two bonding pads of the electrodes to induce hot and cold electrodes separately. This thermal biasing with the optimized implementation showed an enhancement in the ACET fluid velocities and was used for reversing the fluid flow direction. However, such induced thermal bias alone is not capable, without the ACET, to agitate and mix the fluid. In the current thesis, an in-plane design with the 45° angle was tested, where induced temperature boundaries were set on the electrodes to mimic the achieved temperature gradient from the ACET flow. The results showed a very small fluid velocity (3 orders of magnitude less than the ACET) in the fluid velocity directions of x, y, and z.

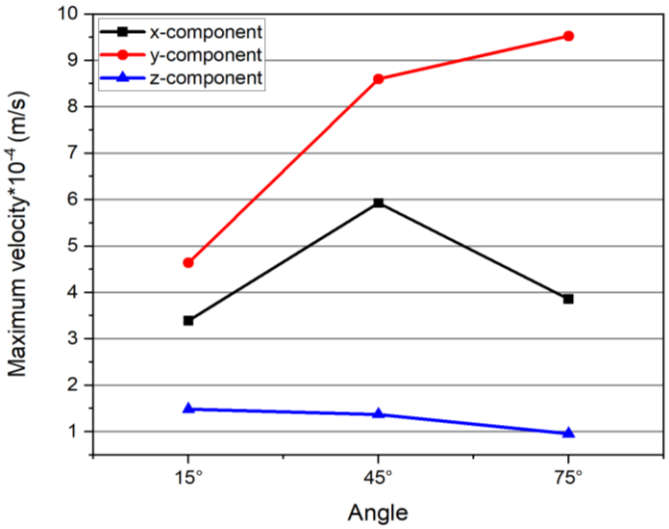

Figure 3.4 Maximum ACET velocity magnitude (m/s) in the in x, y, and z directions for 15°, 45°, and 75° angle between the middle and side electrodes at the same maximum temperature of 49°C.

One may note that higher voltages can be applied to the different designs, thus leading to higher fluid velocities. For example, Figure 3.4 shows the maximum velocity magnitude in x, y, and z directions for 15°, 45°, and 75° angles between the middle and side electrodes at the same generated maximum temperature of 49 °C. It can be seen clearly that the largest angle of 75° can achieve the highest fluid velocity followed by 45° and 15° angles, when actuating the system so that the average temperature is the same. This finding can be practical for inducing higher ACET motion effects without suffering from the excessive generated temperatures, by just tuning the microelectrodes design. Finally, the 15° angle design shows the highest maximum velocity in the z-direction of the fluid flow. This may be due to the top segment of the design having the small gap between the biased electrodes (e.g., zone (i) in figure 3.1), which can induce a relatively stronger ACET vertical fluid flow similar to the fully parallel electrode design.

3.2 Features of ACET versus dielectrophoresis for the in-plane flow design

As already explained in the first chapter, dielectrophoresis (DEP) can be achieved in similar experimental conditions as the ACET, where the DEP will be acting on the microparticles in a way that they either move to regions of high electrical field intensity (positive DEP) or move away from the latter (negative DEP). At the high electrical conductivity of the fluid used in the current studies (1.5 S/m) and the applied AC signal frequency (>=1 MHz), we would expect to have a negative DEP [259]. Having a negative DEP for the proposed in-plane design with the tilted electrodes would lead to pushing the dispersed nanoparticles away from the electrodes. This would mean that the design will act as a repulsion center for the nanoparticles, leading to their migration away from the electrodes in all directions. This is further confirmed by numerical simulation, by investigating the DEP effect into the nanoparticles' motion using the DEP force (equation 1.4). The ACET flow and its Stokes dragging force were tuned off, and instead, the DEP force inside the microparticle tracing module was used in the simulation, using the numerical simulation protocol shown before in Figure 2.16.

Figure 3.5 shows the nanoparticles (20 nm) tracing under the effect of the DEP forces using the newly proposed in-plane design with an AC signal of 20 V_{pp} at 1 MHz. One can see clearly that the

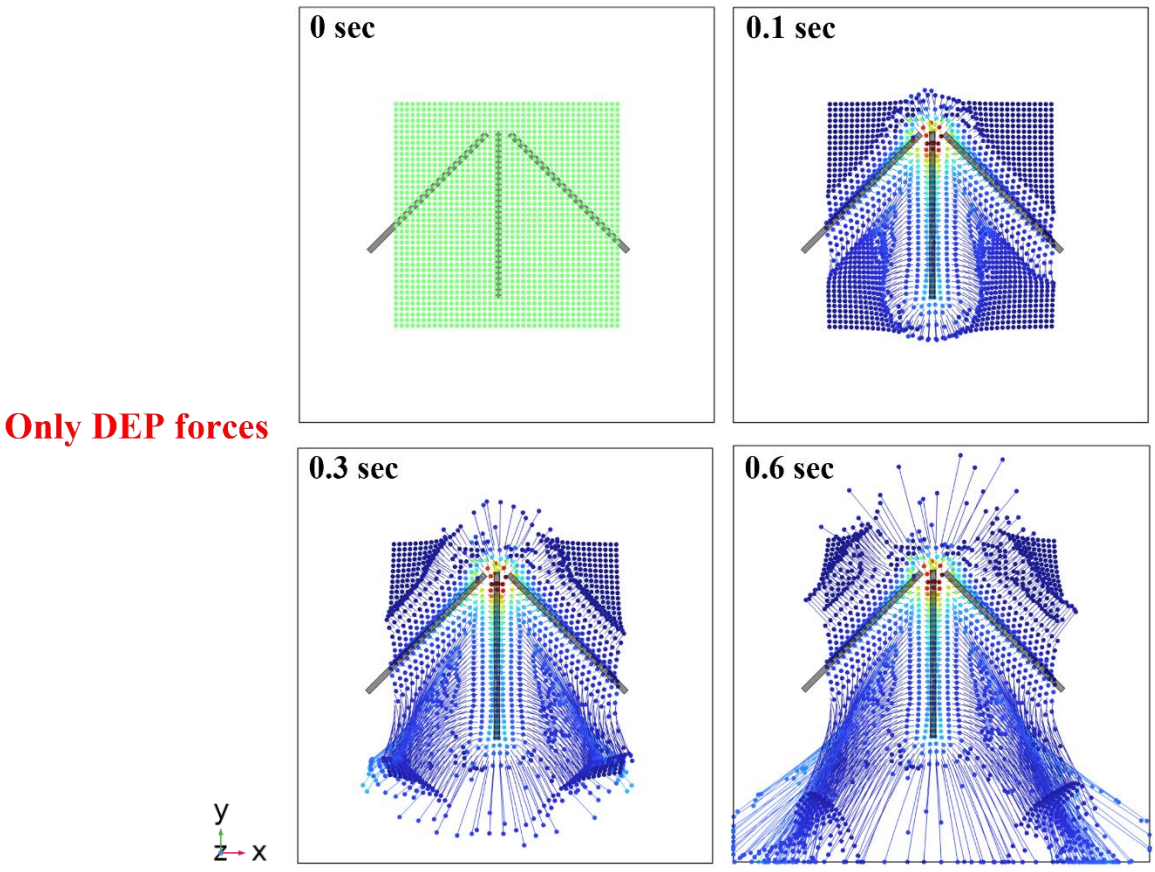

Figure 3.5 Nanoparticles` tracing in case of dielectrophoresis. *Time series images of the numerical simulation of nanoparticle (20 nm) motion due to DEP forces, with an AC signal (20 V_{pp}-1 MHz) applied to the in-plane design.*

nanoparticles are pushed far away from the centre of the in-plane design and in all directions. On the contrary to that, the in-plane design, as thoroughly investigated by numerical simulation and experimental verification in the previous chapter shows two in-plane vortices that push and drag the microparticles in a semi-circular motion around the design center.

Moreover, it is worth noting that using the scaling law analysis for the ACET (equation 2.9) and DEP (equation 1.4) forces, it is clear that the DEP force is proportional to $\nabla|E_{rms}|^2$, while the ACET force is proportional to $\nabla T|E_{rms}|^2$. The temperature gradient ∇T itself, is a function of $|E_{rms}|^2$ as given by the joule heating equation [132,162], thus leading to the ACET force being proportional to $|E_{rms}|^4$. This indicates that the ACET forces are more effective and more dominant than the DEP forces for increasing electrical voltages. Finally, we have carried out a numerical simulation for the in-plane design for the microparticles tracing, but with the integration of both the DEP forces and the ACET forces, using the same electrical conductivity of solution and voltages and on the same microparticles size. Both the drag forces as a result of the ACET and the dielectrophoretic forces that are experienced by the microparticles were calculated. The DEP forces were found to be on average 2~3 orders of magnitude less than the ACET forces, with the microparticles following the traces of the two in-plane vortices previously seen with the ACET flow (e.g., in Figure 3.2). This indeed means that DEP can still have some small effects on the achieved ACET motion even if it may be negligible most of the time. Therefore, careful investigation and characterization of each experiment has to be done to elucidate these effects and their interplay.

3.3 Further electrode designs leading to in-plane fluidic motion

The concept of inducing in-plane ACET can be extended to other designs rather than the tilted straight electrodes design. In addition to that, since the proposed in-plane designs can generate two counter-rotating in-plane vortices, having the same design duplicated and positioned front-to-front can lead to generating ACET flow with four in-plane counter-rotating vortices. Figure 3.6 shows such design concepts of the ACET flow, where the straight-tilted electrodes were replaced by arc electrodes, and the design was duplicated and placed front-to-front. The arc electrodes can be positioned such that they approach each other (what we called the face-in design in Figure 3.6a, 3.6c) or such that the centers of the arcs are away from each other (what we called the face-out design in Figure 3.6b, 3.6d). Both designs are capable of generating four ACET vortices with the following differences. The face-in design (Figure 3.6a) is relatively similar to the previously proposed tilted electrodes` design, except that it has arc-shaped electrodes. This generates similar two in-plane fluidic vortices (total 4 vortices for the shown duplicated design) where the fluid is dragged from the outside of the design to its center. This means that duplicating the tilted electrodes design can similarly generate four in-plane vortices. On the other hand, the face-out design (Figure 3.6b), shows some similarity with the traditional parallel electrodes design, where the top and bottom active parts of the design have parallel orientation between the electrodes, and thus can generate a vertical fluidic motion. Since the design is duplicated with a gap (arc area) between the top and bottom parts and since the fluid has to

be continuous in space and time to feed those active parts, the fluid is dragged to these locations. This collectively leads to the generation of the four ACET fluidic vortices.

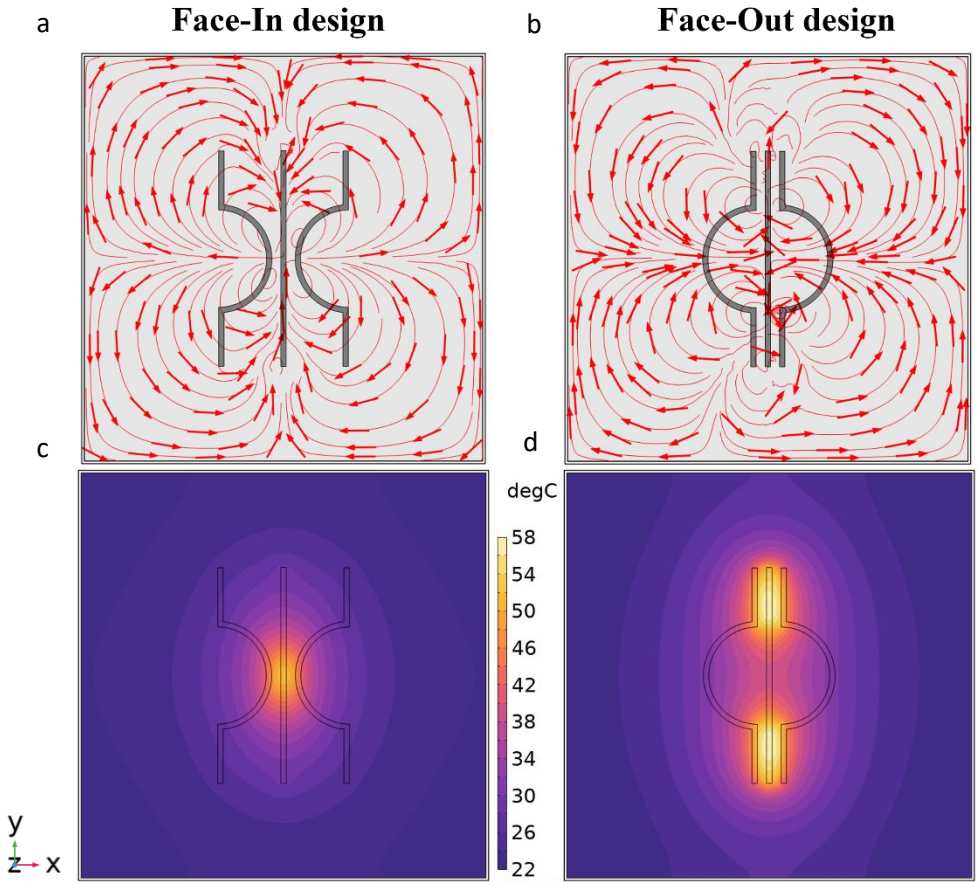

Figure 3.6 ACET microfluidic flow and temperature gradients for so-called face-in and face-out designs. *(a and b) show the ACET microfluidic streaming flow direction, and (c and d) show the temperature gradients, for the face-in and face-out designs, respectively. Middle electrode length is 2 mm and it is actuated with an AC signal (20 V_{pp}-1 MHz) against the two side electrodes with an arc diameter of 1 mm, and a minimum electrodes gap of 85 µm.*

The geometrical differences between the face-in and face-out designs, where the most active ACET parts are at the middle or the top and bottom parts of the design, respectively, lead to different temperature profiles. Figures 3.6c and 3.6d, show the temperature gradients of face-in and face-out designs, respectively. One can see that the high-temperature regions are superimposing with the active ACET fluid flow regions of both designs. Moreover, the face-out design shows a higher fluidic temperature than the face-in design. This is mainly due to the relatively long distance at the top and bottom active parts of the design, where there are parallel electrodes with a constant gap facing each other and thus actively generating high temperatures. This collectively increases the average temperature in the surrounding region. On the other hand, the face-in design has the active part consisting mainly of the arc profile having an increasing gap versus the middle electrode, and this imposes a decaying electric field intensity and temperature over the design length.

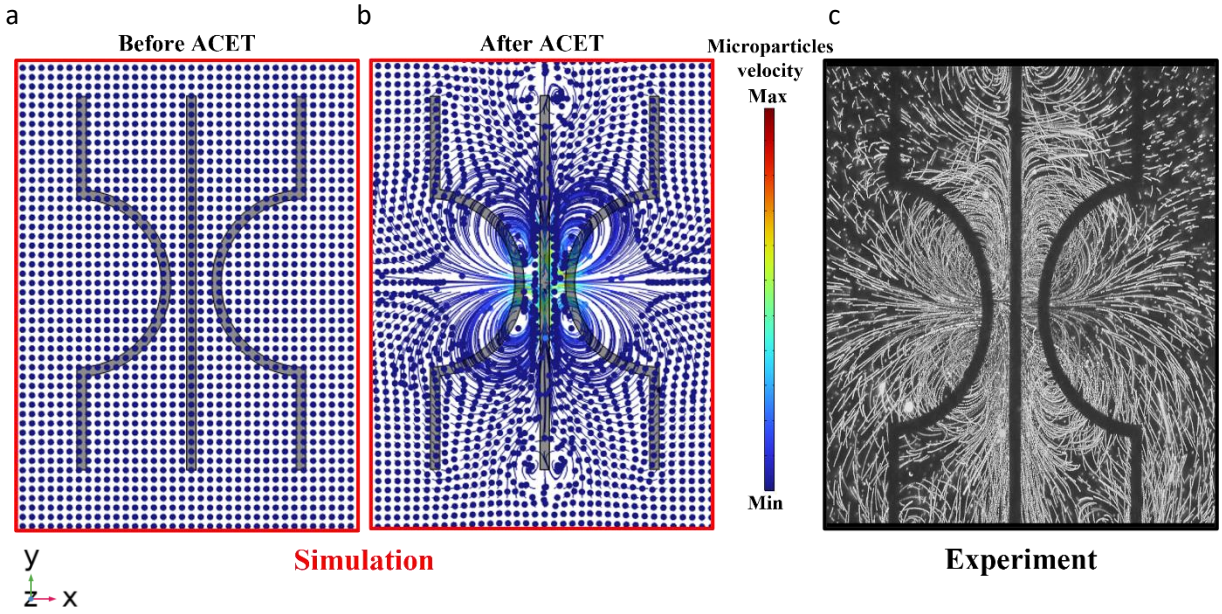

Figure 3.7 Microparticles tracing for the ACET face-in design by simulation and experiments. *(a and b) show the numerical simulation results of the ACET microparticles tracing using the face-in design, before and after the ACET actuation, respectively. (c) shows the experimental superimposed images of a time sequence of 5 µm fluorescent microparticles along the ACET fluidic streamlines of the face-in design.*

The face-in design has been further investigated by microparticle tracing, both using numerical simulation and experiments, to validate the proposed ACET fluidic streaming. Figure 3.7a,b show the microparticles' motion under the influence of the ACET fluidic motion due to the Stokes drag forces. Initially, the microparticles are dispersed homogeneously throughout the chamber (Figure 3.7a). However, under the effect of the ACET fluidic motion, the microparticles follow the fluidic streamlines in the motion direction, forming four in-plane vortices (Figure 3.7b). This design was experimentally realized and mounted for experimental validation following the protocols shown in the last chapter. Figure 3.7c shows the experimental superimposed images of fluorescent microparticles subjected to the face-in design ACET flow patterns. Similar to the simulation results, the microparticles follow the fluidic streamlines direction. The in-plane vortices from the top and bottom halves of the design push the fluid and drag the microparticles, thus leading to the net inward fluidic motion from the design lateral sides (right and left of Figure 3.7c) to its center, while completing the semi-circular four in-plane vortices.

3.4 Pumping using the in-plane ACET

ACET has been used already for possible microfluidic pumping applications. It has been investigated for fluidic pumping in highly conductive solutions [170,260], and further improved by superimposing DC and AC signals on the ACET electrodes to achieve faster fluidic pumping [171], or by inducing a thermal bias to the electrodes [259], or by applying a two-phase AC signal on ACET asymmetric electrodes [172]. Here we have investigated by simulation the possibility to use the new proposed ACET designs for microfluidic pumping. Our design with its dominant in-plane fluidic motion can be optimized for

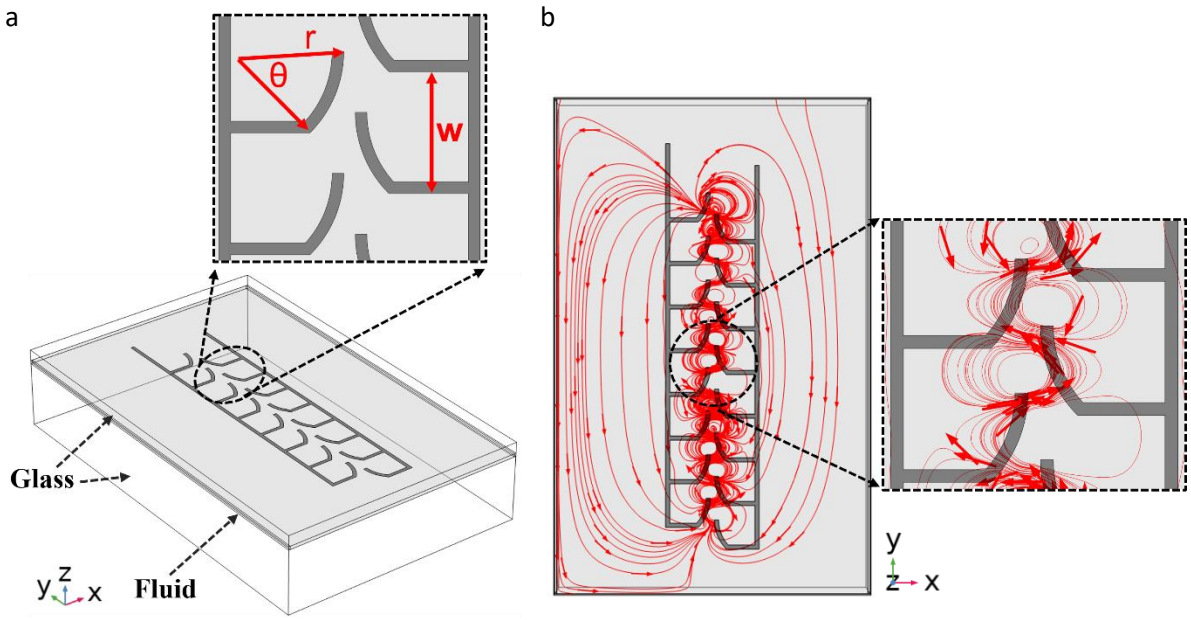

Figure 3.8 ACET microfluidic pumping using arc-type electrode design. *(a) shows the 3D geometry used for the numerical simulation analysis of the proposed arc design. Similar to the previously used setup, the top (170 µm thick) and bottom (1 mm thick) parts are glass slides, with the electrode array located at the bottom of the thin glass slide and facing the fluidic chamber (50 µm high). The zoom-in image shows an array of the shifted-up arc electrodes, with a central angle (θ=44.8°) and radius of 500 µm. The electrodes bottom to bottom vertical shift w is 260 µm. (b) shows the ACET microfluidic streaming resulting from the actuation of the right and the left electrodes array with an AC signal (1 MHz). The zoom-in image shows a detailed view of the fluidic streaming with the red arrows indicating the flow direction.*

unidirectional flow pumping indeed. Several designs such as the tilted electrode design with different tilting angles and the arc designs (face-in and face-out) have been tested.

Figure 3.8a shows the numerical simulation geometry and the proposed ACET pumping design with an array of arc electrodes (θ=44.8° and r=500 µm) facing each other and being actuated with an AC signal. The vertical distance between the bottom of each right and left electrode w is 260 µm, and the lateral gap is 50 µm. Figure 3.8b shows the ACET microfluidic streaming resulting from the AC actuation of the opposite electrodes, with the zoom-in image indicating the possible upward microfluidic pumping. Also, the other designs investigated for microfluidic pumping such as tilted and arc electrodes were capable of fluid pumping. However, the designs showed trapping and in-plane re-circulation of the microparticles resulting in non-efficient directional pumping. Moreover, we have found that the absence of the middle electrode and the alternative vertical shifting of the electrodes` positions enabled inducing a geometrical bias that resulted in the unidirectional microfluidic pumping while reducing the potential trapping. The lateral gap between the electrodes is mainly capable of controlling the microfluidic pumping velocity at a given voltage. However, a relatively large gap can result in a low fluid flow, leading to a less efficient microfluidic pump.

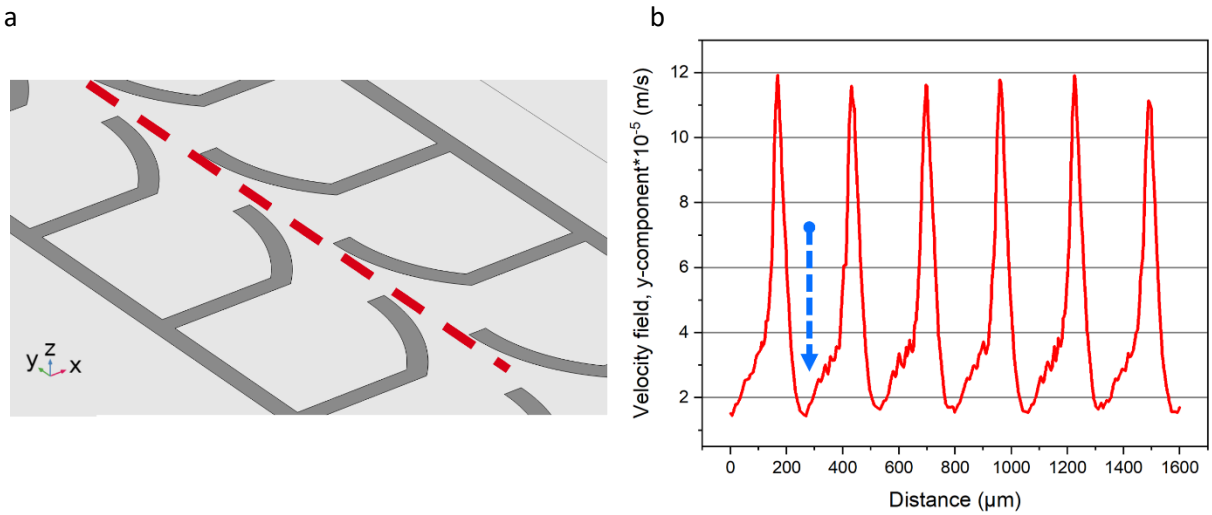

Figure 3.9 Microfluidic pumping analysis using the arc-type electrode design. *(a) shows a small section of the arc design used for the microfluidic pumping with the red dashed line at the centre of the electrodes gap (in the x direction) indicating the line of microfluidic velocity analysis. (b) shows the analysis of the ACET velocity in the y direction, located at the red dashed line in Figure 3.9.a, and the blue dashed arrow indicating the minimum velocity peak.*

In addition to that, the vertical distance w between the alternating up-shifted electrodes can be optimized taking into account several parameters (AC voltage, fluid conductivity, and thermal analysis of the setup), which control how far each side electrode can pump the fluid to reach the coverage range of the next electrode. Figure 3.9b shows the analysis of the microfluidic velocity field in the y direction from the bottom to the top of the design (taken at the red dashed line of Figure 3.9a). The high peaks correspond to the locations at the top end of each side electrode, while the low peaks (blue dashed arrow in Figure 3.9b) correspond to the middle distances in between the alternating side electrodes. These regions, due to their low velocities, can cause a delay in the trans-locational pumping of the fluid. Therefore, the efficiency of the microfluidic pumping system can be further optimized taking into account the vertical distance between the side electrodes, to ensure the maximum pumping velocity in the regions between the electrodes.

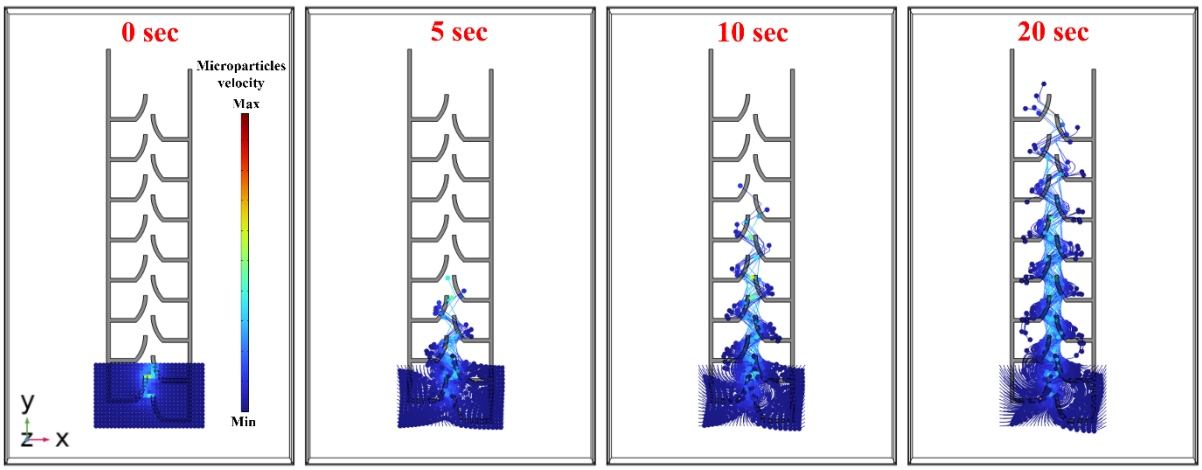

Figure 3.10 Microfluidic pumping revealed by the tracing of nanoparticles using the arc design. *Time series (5, 10, and 20 sec) of nanoparticles (20 nm) transported along the arc design array, with the nanoparticles initially present at the bottom of the design (0 sec).*

We have then investigated the ability of the proposed arc design to induce microfluidic pumping by tracing the motion of nanoparticles. Figure 3.10 shows a grid of nanoparticles initially dispersed and located at the bottom of the arc design array (0 sec). Due to the ACET microfluidic streaming, already shown in Figure 3.8, the nanoparticles are dragged from the sides to the centre of the design. Subsequently, the nanoparticles are pumped upward along the electrodes` array, while the color indicates that the maximum velocity is experienced with the nanoparticles located at the design center. After 20 sec, the nanoparticles were successfully transported to the top of the design. In parallel to that, few nanoparticles will experience in-plane re-circulation, which can impact the pumping efficiency. As explained before, this can be improved by optimizing the design characteristics, such as decreasing the distance *w*.

3.5 Conclusion

In this chapter, we have further investigated the concepts of AC electrothermal flow (ACET) using the newly proposed in-plane design. We explore how variations in design characteristics, such as the angle between the electrodes, can impact the generated in-plane microfluidic streaming. Additionally, we extend the concept of tilted electrode designs from previous chapters to investigate new designs that can generate different forms and coverage areas of in-plane motion. The ability of these designs to generate four in-plane vortices is examined through numerical simulations and experiments. Furthermore, a novel ACET design is proposed and investigated for potential microfluidic pumping applications, where fluid can be pumped over long distances without the need for hydraulic components or mechanically moving parts. This research contributes to the understanding of ACET and its potential for advanced microfluidic applications, showcasing the versatility and adaptability of the proposed in-plane designs for enhancing fluid motion and transport in microscale systems.

86

4 Acoustofluidic mixing for enhanced microfluidic immunoassays for spatial proteomic analysis

This chapter is an adapted version of the following publication that is accepted (not yet published) at Lab on a chip journal - Royal Society of Chemistry (May 2023):

- **Muaz S. Draz (M.D.)**, Diego Dupouy (D.D.), and Martin A. M. Gijs (M.G.), "Acoustofluidic large-scale mixing for enhanced microfluidic immunostaining for tissue diagnostics" Lab Chip, 2023,23, 3258-3271. Authors contribution: Conceptualization: **M.D.**, Simulation: **M.D.**, Experimental Investigation: **M.D.**, Data Curation: **M.D.**, Visualization: **M.D.**, Writing original draft: **M.D.**, Editing: **M.D.**, D.D., M.G., Supervision: D.D., M.G. This project has received funding from the European Union's Horizon 2020 research and innovation program under the Marie Skłodowska-Curie grant agreement No. 754354.
- "Patent application EP23176247.7 filed the 30.05.2023, not published yet, results are confidential"

The usage of microfluidics for automated and fast immunoassays has gained a lot of interest in the last decades. This integration comes with certain challenges, like the reconciliation of laminar flow patterns of micro-scale systems with diffusion-limited mass transport. Several methods have been investigated to enhance microfluidic mixing in microsystems, including acoustic-based fluidic streaming. Here, we report both by numerical simulation and experiments on the beneficiary effect of acoustic agitation on the uniformity of immunostaining in large-size and thin microfluidic chambers. Moreover, we investigate by numerical simulation the impact of reducing the incubation times and the concentrations of the biochemical detection reagents on the obtained immunoassay signal. Finally, acoustofluidic mixing was successfully used to reduce by 80% the incubation time of the Her2 (Human epidermal growth factor receptor 2) and CK (Cytokeratines) biomarkers for the spatial immunostaining of breast cancer cell pellets, or reducing their concentration by 66% and achieving a higher signal-to-background ratio than comparable spatially resolved immunoassays with static incubation.

4.1 Introduction

The application of microfluidics in the field of spatial molecular profiling of tumor tissues has gained a lot of interest in the last years[63,65,66,261]. The two most common techniques for tissue diagnostics are immunohistochemistry (IHC) and *in situ* hybridization (ISH)[67,262] as explained in the first chapter. Three important factors affect the performance and the quality of these diagnostic techniques using microfluidic systems, namely, the uniformity of the tissue staining, the used detection reagent concentration, and the incubation times onto the tissue. The uniform staining of the tissue plays an important role in the analysis since it ensures that all relevant target analytes on the tissue are exposed equally to the detection reagents, enhancing the signal contrast and leading to consistent results[263]. Non-uniform staining might jeopardize the analysis of the tumor section, leading to a false or biased diagnosis or prognosis[65,262,264]. There have been several reports on the adaption of a microfluidic tissue processor system (MTP) for tissue immunostaining[63,65,83–86,261,262,265], where the thin tissue section is mounted on a glass slide and incubated inside a chamber where a microfluidic distributing channel network is used to distribute the bioreagents uniformly above the tissue.

The same concept of the distribution channel network has been adopted for other research purposes, such as in the microfluidic concentration gradient generator[74–76,99], where the common characteristic of these designs is the possibility to generate a concentration gradient across the channel width and perpendicular to the flow direction. This concentration gradient can be beneficial for chemotaxis studies, in which chemicals need to be delivered to cells in a concentration-gradient form[77], and for optimized neural stem cells growth and differentiation[78], and for yeast gene expression under gradients of pheromones[79], or for gradient treatments of cells across the width of the microchannel[80]. However, these gradients can have the disadvantageous effect of the uneven staining of the tissue. Concentration gradients can be minimized in tissue staining, including by applying extremely high-pressure microfluidics to induce turbulent reagent streams, by lowering the distance between the neighboring streams in the microfluidic channel distribution network (which can be limited by the maximum pressure the system can withstand), or by prolonging the reagent's incubation time to allow for the reagents to diffuse. The use of high pressure in microfluidic systems would require high-pressure pumps, and the firm sealing of the fluidic chamber; otherwise, fluid leakage might happen during the experiments leading to non-proper functioning and possible safety concerns[262,266,267]. At the same time, high flow rates can lead to high frictional shear forces acting on the surface-mounted cells thus affecting their cellular function and biological responses[268,269], and can affect the tissue morphology and integrity. Moreover, high flow rates running through relatively small diameter inlet holes and along sharp edges can lead to cavitation microbubble[270,271], which, if trapped inside the chamber, can alter the flow dynamics and the exposure of the tissue sample to the detection reagents.

Secondly, reducing the incubation times of immune detection reagents with the tissue can be of vital benefit, since this can shorten the analysis time and thus provide faster results. Moreover, it can reduce the background signal due to nonspecific binding[262,264,272]. However, reducing the incubation time would mean shorter exposure periods are given to the detection reagents to interact with the

target tissue, reducing the immunostaining signal. In addition to that, during the static incubation time (low Péclet values), a depletion region with a low concentration of the reagents is formed above the reacting surface (tissue), whereafter the immuno-reaction starts to be diffusion-limited (large Damköhler values)[37,273]. Biological molecules having diffusion coefficients in the range of 10^{-11} to 10^{-12} m^2/s [274,275] would need longer incubation times to be able to diffuse throughout the chamber and interact with the tissue.

Finally, the concentration of the immunoreagents can have a great impact on the immunoassays since reducing the consumption of the bio-reagents can reduce the overall cost of the experimental and diagnostic tests. Additionally, high concentrations of antibodies used for immunohistochemistry can lead to false positives or excessive background staining[276,277], and it is frequently found that many antibody production companies suggest the reduction of the antibody concentration to reduce the nonspecific binding. On the other hand, reducing the concentration of the reagent would lower the amount of the available detection reagents above the tissue and thus reduce the immunodetection signal. The impact of the low concentration on the detection signal is larger when it is considered with the abovementioned depletion region formation and the limited diffusional mass transport of the bio-reagents.

Several technologies have been developed and integrated into microfluidics to induce a disruption between the fluid thin layers associated with the laminar flow regime by enhancing the fluidic mixing and thus helping to counteract the diffusion-limited transport of the bio-chemical reagents in microfluidic systems. For example, magnetic-based microfluidic mixing was investigated where a fluid of dispersed magnetic particles or rods inside the chamber is actuated by an external magnet[112,125], but this requires a closely attached magnetic actuator and the magnetic beads can interfere with the immunoassay performance while limiting the optical readout through the chamber. Moreover, acoustic actuation of vibrating structures[278,279] or trapped microbubbles[201,280] has been investigated for microfluidic mixing which can require a lengthy microfabrication process, and the efficient trapping of the microbubbles inside the chamber throughout the full experiment, and possibly the need for high-frequency matching and signal generators[281]. Furthermore, electro-kinetic techniques such as the AC-electrothermal technique have been used for enhancing the microfluidic mixing and immunoassays, but it requires the microfabrication of the actuating electrodes and, if not optimized, can generate relatively high temperatures and lead to electrolysis[273,282,283].

Here we introduce the integration of a low-frequency acoustofluidic mixing device for enhancing microfluidic immunoassays. Piezoelectric actuators are mounted with water-soluble glue on the exterior surface of a microfluidic staining system and the actuation of the piezoelectric elements leads to the generation of vortex-like patterns of acoustic streaming within the microfluidic chamber. The proposed idea has several advantages, including ease of integration, working at low frequencies thus omitting the need for advanced and accurate high-frequency devices, a low cost of the core element (our piezoelectric actuator costs less than 1 USD), the absence of any additional microfabrication steps, retaining the possibility of microscopic imaging over the complete thin chamber, and, finally, the absence of thermal interference with the conducted experiments.

We performed a numerical simulation to explain the working mechanism behind the reported work, including the investigation of the effect of the piezoelectric element actuation on the system vibration and more specifically on the surface reaction at the solid-fluid interface. The simulated acoustic pressure and mechanical stress are then coupled to the fluidic domain to investigate acoustic streaming and the associated microparticle motion. The presence of acoustofluidic vortex-like patterns was validated by the experimental tracing of fluorescence microparticles. Acoustofluidic mixing was investigated for its potential with respect to the immunoassay performance (elimination of non-uniform staining due to microfluidic gradients, reducing the reagents' incubation times, and enabling the use of lower reagent concentrations). Furthermore, numerical simulation was used to investigate the formation of the concentration depletion region above a reacting surface and the associated rapidly decaying reaction rate, and the effect of using lower reagent concentration on the surface reaction. Finally, we demonstrate the feasibility of using the acoustofluidic mixing to enhance the immunoassay staining of the Her2 tumor marker (human epidermal growth factor receptor2, also known as ERBB2) and CK (cytokeratins) on BT-474 cancer cell pellet sections. The Her2 gene is amplified in 18–20% of the primary breast cancer cases, leading to the overexpression of the associated protein, rapid tumor proliferation, and poor prognosis of the disease[284]. CK has been widely used in the histopathological evaluation of breast carcinoma to identify tumor epithelial cells and help in differentiating between the specific breast cancer subtypes[285]. To the best of our knowledge, this is the first research that demonstrates acoustofluidic mixing for spatial proteomic analysis on cell pellet sections. The experimental acoustofluidic mixing device was successfully used, and, in contrary to the results that might be anticipated based on the simulation of static incubation of surface reactions, succeeded to reduce the reagents incubation time by 80% and reducing the reagents consumption by 66%, while still obtaining higher signals than a static incubation.

4.2 Experimental setup

The experimental setup relies on a wide and thin microfluidic system that has been used before for tissue diagnostics[65,83–86,261,262,265]. The core element is a polymer chip (Figure 4.1a) which provides the fluidic connections to the chamber (through the small white inlet holes). The latter has a glass coverslip at its top, which allows for imaging accessibility. The staining chamber is realized by clamping the polymer chip against the substrate slide that carries a tissue or cell pellet slice and being in contact with a bottom temperature-controlling system (Figure 4.1b). An O-ring (Figure 4.1b) is used to ensure

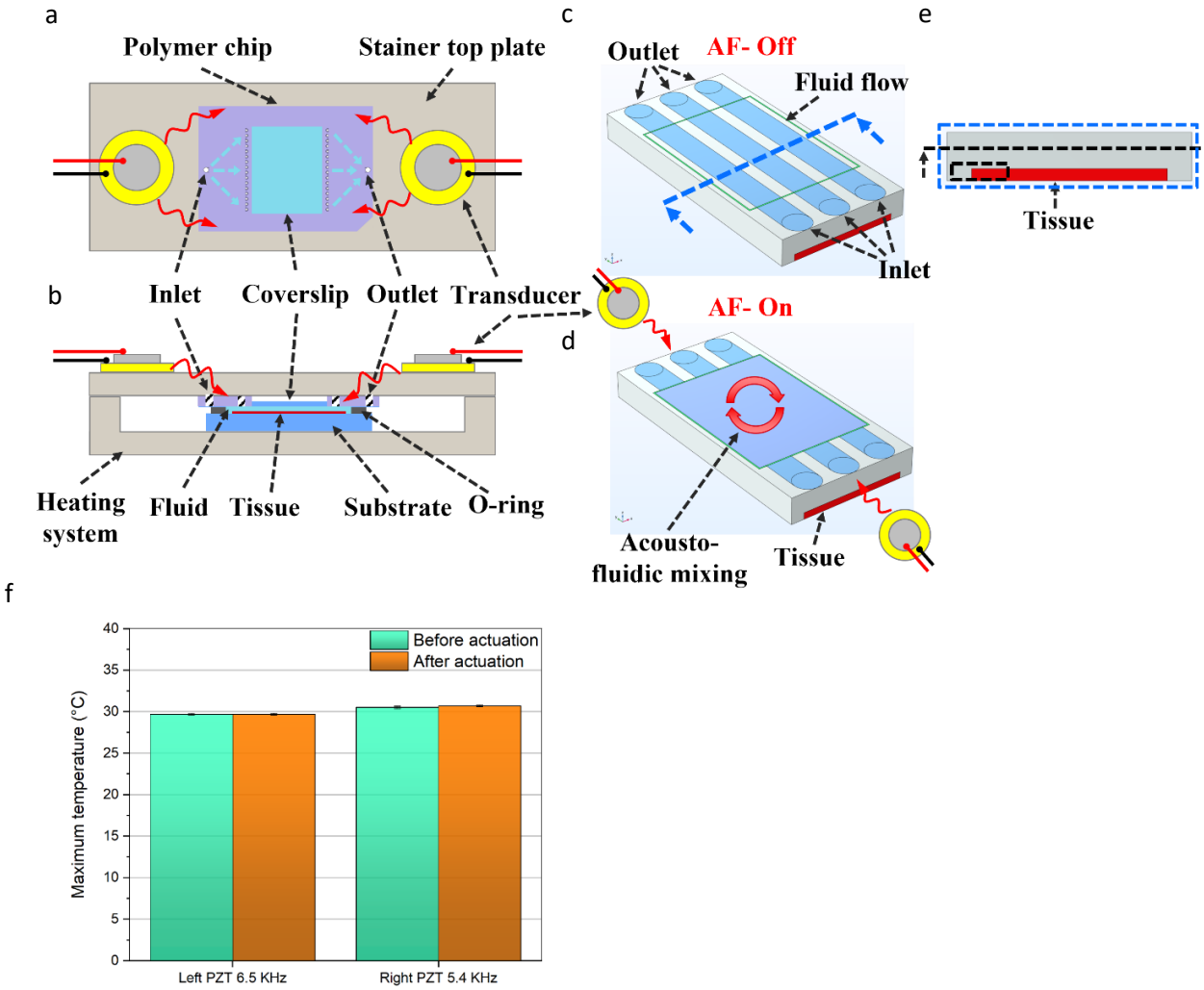

***Figure 4.1 Experimental setup**. (a) Top schematic view of the microfluidic setup with the piezoelectric transducers mounted on the two sides of the stainer top plate, and the polymer chip used with the distributed channel network design (the larger white inlet hole supplying the fluid into the multiple fluidic paths represented by the blue dashed arrows to dispense the liquid into the chamber through the small white holes, and similar for the outlet). A glass coverslip is located at the polymer chip centre which allows imaging accessibility from the top. (b) Cross-sectional schematic side view of the closed system setup showing the polymer chip clamped against the substrate holding the sample (e.g., a tissue) with an O-ring that seals the microfluidic chamber (15×15x0.05 mm³). A heating system is used to control the temperature of the setup. (c, d) Simplified schematic of the acoustofluidic mixing within a part of the microfluidic chamber, showing three inlet/outlet ports, and a thin tissue located at the chamber bottom, before (c) and after (d) actuating the piezoelectric transducers. (e) Front view image of the chamber (at the cross-section line of Figure 4.1c), with the thin tissue located at the bottom, and a cross-sectional dash-line and dash-line box showing the region considered for further analysis in Figures 4.4 to 4.7. (f) The maximum temperature monitored on the piezoelectric transducers located at the left or the right of the microfluidic chamber, before and after the actuation of each transducer at the corresponding frequency and at a power of 35 mArms.*

chamber sealing and prevent fluidic leakage. Two piezoelectric transducers (RND 430-00018) (Figure 4.1a) are glued on the exterior face of the stainer top plate and aligned horizontally with the microfluidic chamber. A water-based glue (Tensive conductive adhesive gel), was used which allows the easy positioning and re-application of the transducers. The piezoelectric transducers are actuated with a function generator (AFG3021B, Tektronix), and the signal is amplified with a high voltage amplifier (WMA-300, Falco-system) and monitored by an oscilloscope (54602B, HP). The transducer located to the left of the chamber is actuated at 6.5 kHz and 18 mArms, while the transducer located to the right of the chamber is actuated at 5.4 kHz and 18 mArms throughout the whole presented work. For each experiment with acoustofluidic mixing, the experiment duration was divided into four-time slots, and the two transducers were actuated sequentially (e.g., for the 4 minutes experiments, the 1st minute: right PZT-on and left PZT-off, then for the 2nd minute: right PZT-off and left PZT-on, …etc). All fluid handling and flow rates were controlled by an integrated pressure pumping system. Figure 4.1c shows a simplified schematic of the microfluidic chamber (showing here only 3 inlet/outlet ports) that allows dispensing laminar flow streams of the reagents from the small holes over the thin tissue located at the bottom of the chamber. Figure 4.1d shows a simplified schematic of the acoustofluidic mixing patterns generated after the actuation of the piezoelectric transducers located at the sides of the chamber. The actuation of the transducer at the corresponding frequencies used throughout the current research and at a power of 35 mArms (higher than what is used for the research work), shows no increase in the maximum temperature (Figure 4.1f), as observed on the transducers by an IR thermal camera. Similarly, the temperature inside the chamber and far away from the transducer shows no change at all. All details of the immunoassay and fluorescence imaging are described in the Methods & protocols section 4.6

4.3 Numerical simulation

4.3.1 Surface-based reaction and microfluidic analyte transport

It is presumed that the reaction between the diffusing reagent analyte and the surface-immobilized target (tissue) will proceed according to a first-order Langmuir adsorption model [286]. Equation (4.1) relates the target density B_0 to the reagent analyte concentration at the reaction surface $A_{surface}$ and the molar concentration of the analyte-target complex $[AB]$ being generated over the reaction time,[273]

$$\frac{\partial [AB]}{\partial t} = k_{on}[A]_{surface}\{[B_0] - [AB]\} - k_d[AB] \qquad 4.1$$

where k_{on}, k_d are the association and dissociation rate constants respectively. The initial target density used is $B_0 = 3.3 \times 10^{-8}[\mathrm{mol/m^2}]$, and the reagent dissociation constant $k_d = 10^{-2}[1/\mathrm{s}]$, and the reagent association constant k_{on} was simulated for the value of $k_{on} = 10^{6}[\mathrm{m^3/(s.mol)}]$, all simulations were done by COMSOL Multiphysics 6.0. The initial bulk reagent analyte concentration $A_{surface}$ available at the reacting surface (tissue) was simulated for the range of 10^{-10},

0.5×10^{-10}, 0.33×10^{-10}, and 0.25×10^{-10} mol/m^3. The reagent bulk concentration over the reacting surface tissue can be replenished by the fluid flow according to Fick's second law of diffusion, as shown in equation (4.2),[273]

$$\frac{\partial[A]}{\partial t} + U \cdot \nabla[A] = D\,\nabla^2[A] + R \qquad 4.2$$

where A is the reagent analyte concentration in the bulk fluid, U is the fluid flow velocity, D is the reagent analyte's diffusion coefficient, and R is the reaction rate, which in the bulk fluid equals zero given that there is no reaction occurring in the fluid.

4.3.2 Acoustofluidics

The numerical simulation (using COMSOL 6.1) of the acoustofluidic motion was done in two steps. In the first part, the setup in 2D from the side view was simulated to gain insights into the effect of the transducer actuation and the accompanying acoustic pressure distribution, and the solid stress and

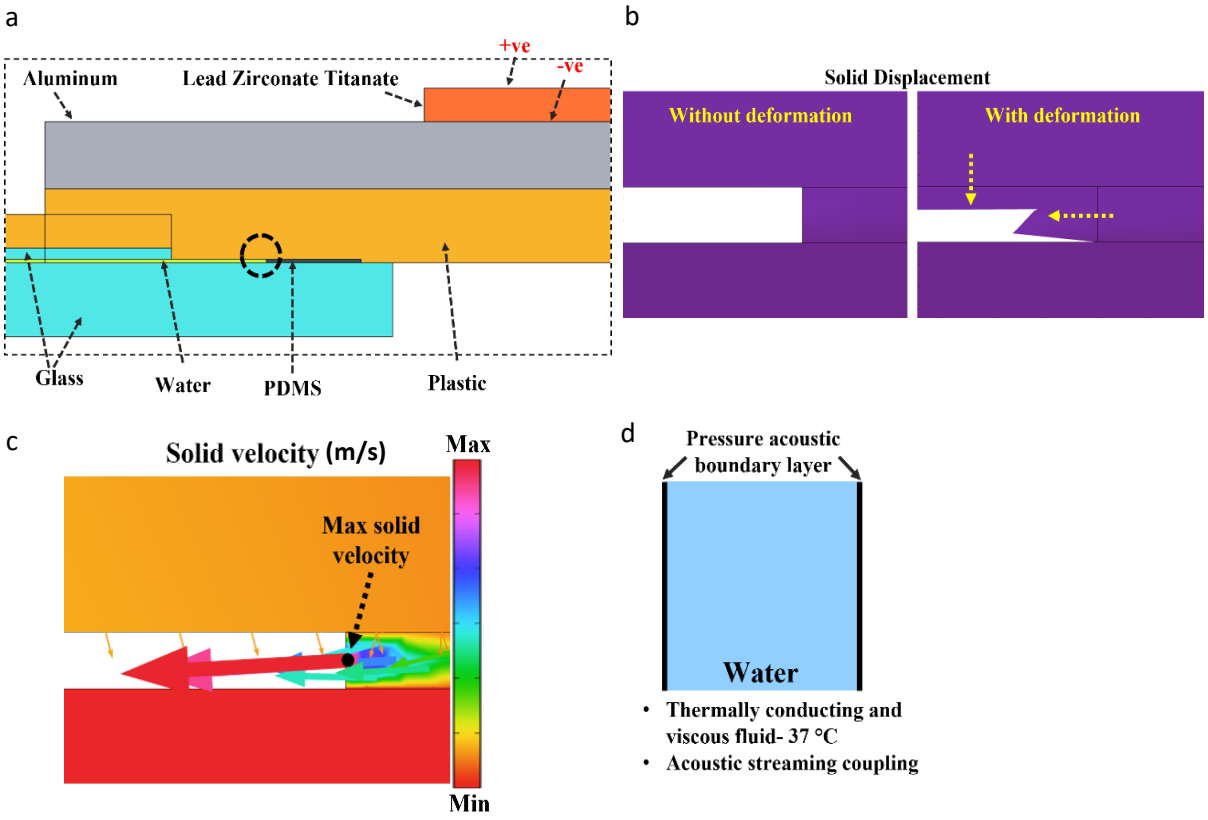

***Figure 4.2 Acoustofluidic simulation**. (a) The components used in the 2D setup (side view) for the characterization of the acoustic vibration and solid mechanics of the system. A transducer (Lead Zirconate Titanate, PZT) is actuated by the AC signal (+ve and -ve) and mounted on the top of a metallic (aluminium) plate which is clamped against the polymer (plastic) chip, and the glass coverslip and glass substrate, and the water chamber sealed from the side with a PDMS ring. (b) The solid displacement of the system at the region of interest (ROI) is indicated by the dash-circle in Figure 4.2a as a result of the actuation of the PZT transducer. The solid deformation shows the displacement of the plastic and PDMS domains. (c) The solid velocity at the same ROI showing the maximum velocity point is located at the PDMS-water interface boundary, and the arrows show the solid velocity direction with the arrows' size proportional to the solid velocity components (X, Y). (d) The 2D setup (top view) that is used for the characterization of the pressure acoustics and the fluid flow and particles' tracing, taking the side walls as vibrating boundaries as obtained from the 2D simulation shown in Figure 4.2c.*

strain (see also Figure 4.8). The electrostatic module was used to actuate the transducer (Lead Zirconate Titanate, PZT) by applying an AC signal as shown in Figure 4.2a, and the solid mechanics module was used to compute the solid components' structural analysis. The PZT material was used in the stress-charge form using the PZT-4D properties. Finally, the pressure acoustics module was simulated to compute the pressure variation and the acoustic wave propagation into the fluid. All three modules were solved in the frequency domain and the piezoelectric effect was used to couple the electrostatics and solid mechanics physics, while the acoustic-structure boundary was used to couple the pressure acoustics and the structural components of the system, as shown in Methods & protocols section 4.6 (Figure 4.8).

Figure 4.2b shows the solid displacement at the region of interest (ROI) (indicated by a dashed circle in Figure 4.2a), which is situated at the first contact point (close to the PZT) between the solid components and the fluid domain. The system deformation at that region shows the displacement of the plastic and PDMS domains (soft materials,[287,288]) as a result of the transducer actuation. Furthermore, the solid velocity as a result of the acoustic structural boundary coupling was computed, which takes into account the fluid load on the structure and the structural acceleration as experienced by the fluid. Figure 4.2c shows that the maximum solid velocity point of the whole simulated setup is located at the boundary layer of the PDMS-water interface, while the colored arrows show that the solid velocity components in the x (lateral) direction are the highest. Both the solid displacement and velocity are scalable with the applied acoustic power, and thus higher actuation (higher voltages) would lead to higher velocities. In the second 2D simulation, the fluid domain from the top view, as shown in Figure 4.2d, with the side acoustic boundary layers was used to simulate the pressure variations and the propagation of acoustic waves and the resulting acoustofluidic motion, as described in the Methods & protocols section 4.6 (Figure 4.8). The pressure acoustics module was used, in which, a thermo-viscous acoustic boundary layer is applied to the right or the left side of the fluid chamber. A mechanical wall vibration was used taking into account the range of wall displacements[289–291] computed in the first part, with a velocity $V_{wall} = D_0\omega$ (m/sec) where D_0 is the displacement magnitude and ω is the angular frequency. The fluid domain was assumed to be thermally conducting and viscous to take into account the attenuation due to bulk viscous losses. Due to the acoustic wave attenuation and the generated gradients in the time-averaged acoustic momentum flux in a viscous fluid, a net displacement of the fluid particles is generated leading to a steady fluid flow known as acoustic streaming[190,292,293]. For fluids and assuming that the pressure varies harmonically in time, the acoustic field pressure can be described according to equation (4.3),

$$\nabla \cdot \left(-\frac{1}{\rho_c}\nabla p\right) - \frac{w^2 p}{c^2 \rho_c} = 0 \qquad 4.3$$

where p is the pressure (Pa), ρ_c is the density (kg/m^3), c is the speed of sound (m/sec), and w is the angular frequency of the pressure field. After solving for the acoustic pressure and the sound levels and the acoustic acceleration in the system, the output was coupled to the laminar flow module, where the pressure and velocity fields of the time-average fluid flow using the Navier–Stokes equations were computed. Finally, the time-averaged Stokes drag force (F_{drag}) on spherical particles with a radius r_p and moving with a velocity u, while being located inside a viscous fluid with a streaming velocity v, can be calculated by equation (4.4),[291]

$$F_{drag} = 6\pi\mu\, r_p(v-u) \qquad 4.4$$

where μ is the dynamic viscosity of the fluid (Pa·s).

4.4 Results

4.4.1 Acoustofluidic mixing

When the piezoelectric transducers located at the sides of the experimental setup shown in Figure 4.1 and Figure 4.2a are actuated, the device resonates. Since the device components are firmly clamped against each other, the resonation of the transducer is translated throughout the device, depending on several factors including the speed and attenuation of sound on each material component. Since most of the setup components are firmly fixed against each other and the surrounding device and are highly sealed to ensure no leakage during the experiments, an analysis of the resulting acoustic pressure distribution and the solid mechanics shows that the inner sides of the polymer chip facing the fluidic chamber possess the highest vibration amplitude, as shown in Figure 4.2b and Figure 4.2c.

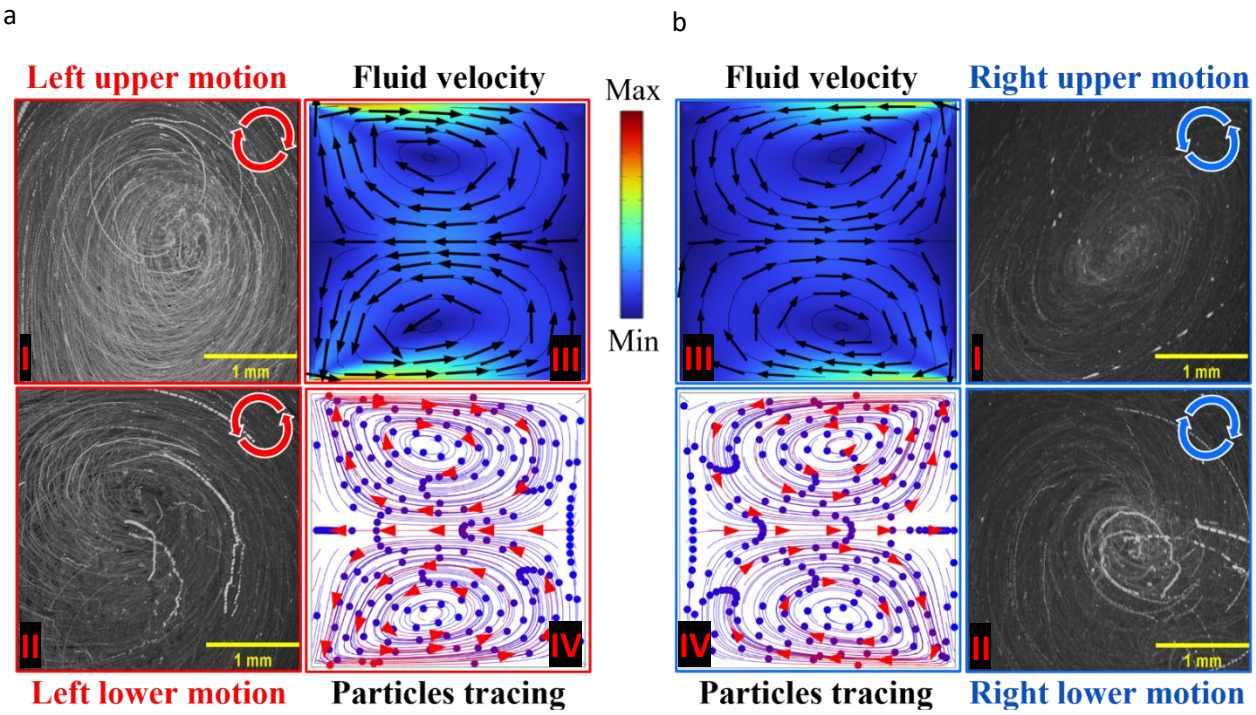

Figure 4.3 Acoustofluidic mixing*. (a) and (b) show the experimental (I and II) and the simulation (III and IV) results of the acoustofluidic motion generated after the activation of the piezoelectric transducers, positioned to the left (a) or to the right (b) of the microfluidic chamber, as shown in Figure 4.1a. The left and the right transducer were actuated at the frequencies of 6.5 and 5.4 kHz, respectively, each generating two vortex-like patterns of fluidic motion. Sub-figures (I and II) show the experimental superimposed images of fluorescent microparticles observed at the top (I) and the bottom (II) parts of the chamber. The red and blue arrows indicate the observed acoustofluidic motion direction when the left (red) or the right (blue) transducers were activated. Sub-figures (III and IV) show the microfluidic fluidic motion direction (III) and the microparticles (3 µm) tracing (IV) in the square chamber, resulting from the actuation of each of the side boundary layers. The simulation was carried out according to the model shown in Figure 4.2d and as described after. Both figures show two fluidic vortices that are similar in fluid direction to those observed in Sub-figures (I and II) at the top and bottom of the chamber.*

This is mainly because the sidewalls made of PDMS are the softest material (with the highest vibration amplitude) used in the system. Since these elements are in direct contact with the fluid, their vibration would lead to the agitation of the fluid and the generation of the acoustofluidic motion. Figures 4.3a and 4.3b show respectively the experimental and numerical simulation results of the acoustofluidic motion observed in the chamber under the actuation of the left transducer (Figure 4.3a) at 6.5 kHz or the right transducer (Figure 4.3b) at 5.4 kHz. This range of frequencies was found to generate the strongest microfluidic motion, as observed by the tracing of fluorescence microparticles. The difference in the frequencies can be due to the non-symmetrical shape of the system components such as the polymer chip and the location where the chip is mounted in the system. Figures 4.3a-I and 4.3a-II and 4.3b-I and 4.3b-II show the superimposed images of the fluorescence microparticles when the left (a) or the right (b) transducer was actuated. Generally, in each case, two large-scale vortex-like patterns of acoustic streaming were observed with opposite directions of motion at the top and bottom regions of the chamber. The direction of the fluid motion is generally pointing horizontally away from the actuated transducer and away from the upper and lower corners of the chamber. We have noted that, during the experiments, some particles tend to aggregate over time, even before applying the acoustic field, probably due to particle-particle interactions[294].

Moreover, some particles under the effect of the acoustic field, showed a circular motion while following the large acoustofluidic vortices. This can be due to the viscous torque as a result of the acoustic streaming in the viscous boundary layer around the particle itself or the acoustic torque induced on the object.[295–297] Figures 4.3 a-III and 4.3b-III show the numerical simulation results of the fluid vortices under the actuation of the left (a) or the right (b) sides of the chamber (shown in Figure 4.2d) as a pressure acoustic boundary layer. The simulated domain is filled with water at 37 °C and assumed to be a thermally conducting and viscous fluid while the acoustic streaming is coupled from the pressure acoustics to the fluid domain and its borders. For each of the actuated side transducers, the numerical simulation shows two acoustofluidic motion areas with vortex like-pattern in the chamber, where the fluid direction of motion for each chamber location agrees with the experimentally observed acoustofluidic vortex-like patterns shown in Figures 4.3a-I, a-II and 3b-I, b-II. Carrying out the numerical simulation, while coupling only the acoustic pressure to the boundary layer and disabling the domain coupling, shows the same results and velocity values. This indicates that the major mechanism behind the acoustic streaming is linked to the PDMS boundary layers, and not the effect of the acoustic pressure acting as a volume force on the bulk fluid.

Figures 4.3a-IV and 3b-IV show the numerical simulation results of the microparticles tracing under the effect of the fluid Stokes drag force calculated using equation (4.4). The microparticles are initially dispersed uniformly throughout the full chamber. However, under the effect of the acoustofluidic generated motion, the microparticles follow the fluidic streamlines. Similarly, the microparticles' direction of motion agrees with the experimentally observed microparticle motion shown in Figures 3-I and 3-II. The simulated microparticles` size was 3 µm, however, a wide range of microparticle sizes were tested and were all found to follow the acoustofluidic vortices direction with expected differences in the particle's velocity. Finally, the microparticles can be affected by the acoustic radiation forces which can move and focus the microparticles in the pressure nodes based on their

acoustic contrast to the surrounding fluid[298]. However, given the frequencies in the low sub-MHz regime used in the current research (6.5 and 5.4 kHz), the streaming-induced velocity tends to be much higher than the acoustic radiation forces [291,299]. This was further confirmed by numerical simulation where the acoustic radiation force acting on the simulated microparticles was found to be 2 to 4 orders of magnitude less than the acting drag forces.

4.4.2 Acoustofluidic smoothening of microfluidic gradients

Here, we show how the acoustofluidic motion helps smoothening the microfluidic gradients, that can be formed inside the chamber due to the laminar flow regime of the fluid and the microfluidic channel network design used, thereby leading to more uniform staining within the thin chamber. Figure 4.4a shows the cross-sectional numerical analysis of the analyte reagent concentration (mol/m^3) at the chamber center as indicated by the cross-sectional dash line in Figure 4.1e, at three different fluidic flow rates of 300, 900, and 1500 µl/min, after 5 and 10 sec of fluid dispensing, obtained by simulation. The high-concentration peaks correspond to the locations in front of the inlet/outlet ports (blue wide lines in schematic Figure 4.1c, while the low-concentration peaks correspond to the locations in between the side-by-side inlet/outlet ports (white wide lines in schematic Figure 4.1c), where the fluid velocity is lower. This evidently leads to big differences in the available reagent concentrations above the tissue slices horizontally along the direction orthogonal to the fluid flow. The average ratio (n=10) of the concentration minima over the peak concentrations along the line in Figure 4.1e, after 5 and 10 sec, is 0.09% and 45% for 300 µl /min, and 26% and 98% for 900 µl/min, and 69% and 100% for 1500 µl/min, respectively. It is worth noting that the tissue is experiencing these concentration differences during the active bioreagent dispensing, where a very fast replenishment of the reacting species is happening above the tissue. These differences, even if happening for a short time, can lead to big differences in the bioreagents` distribution and thus lead to the non-uniform staining of the tissue sample and possibly a false diagnostic analysis of the biological marker of interest. Figure 4.4b shows the experimental staining of a large Bt-474 (Human breast cancer tissue) section with 300 µl/min dispense flow rate and 1 min incubation time of primary antibodies (Her2 rabbit and CK mouse) and secondary antibodies (anti-rabbit 647 and anti-mouse 555) all at 1:200 dilution ratio, without (I) and with (II) the acoustofluidic mixing.

The full immunoassay protocol is described in the Methods & protocols section 4.6. After the immunoassay, the sections were mounted and imaged using an automatic fluorescent scanning system, and the fluorescence intensity was measured, as explained in the Methods & protocols section 4.6. Figure 4.4b-I shows a clear non-homogenous gradient staining of the section with the two markers used (Her2 in green color and cytokeratins in red color), where the direction of the gradients is perpendicular to the fluid flow direction and the multi-inlet/outlet ports. Figure 4.4b-II shows the experimental effect of the acoustofluidic mixing on the active uniform distribution of the bioreagents over the tissue and throughout the chamber thus the elimination of the gradients overserved. The acoustofluidic mixing effect is further clarified by numerical simulation in Figure 4.4c.

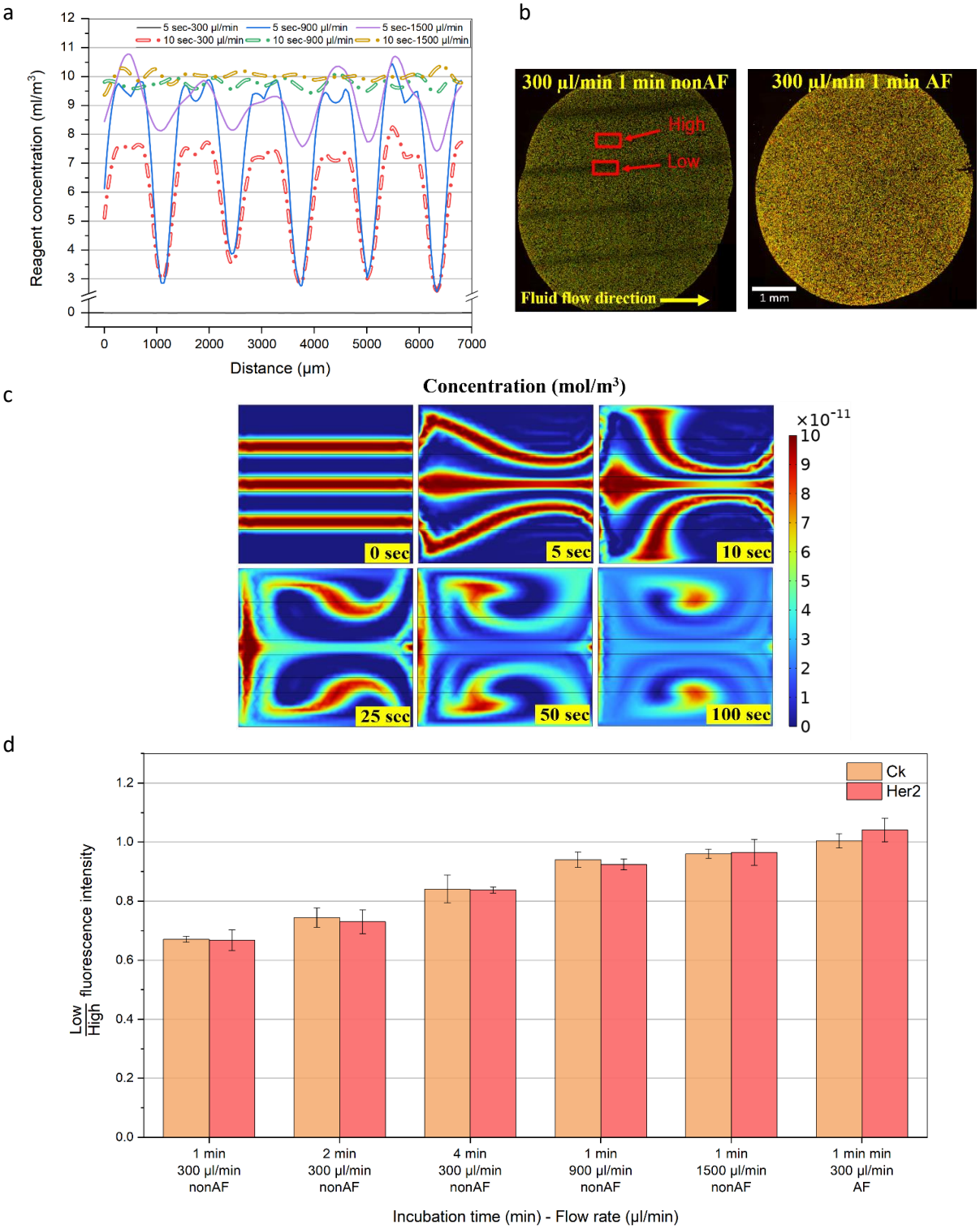

Figure 4.4 Smoothening of microfluidic gradients by acoustofluidics. *(a) The reagent concentration (mol/m³) (at the middle of the chamber as indicated by the cross-sectional dashed line in Figure 4.1c and across the middle of the chamber height, as indicated by the cross-sectional dashed line in Figure 4.1e), for three fluidic flow rates 300, 900, and 1500 µl/min after 5 and 10 seconds, obtained by numerical simulation. (b) Fluorescence images of a Bt-474 cancer cell pellet stained with Her2 marker (green) and CK marker (red) at a 300 µl/min dispense flow rate, followed by an incubation time of 1 min, without (I) and with (II) the acoustofluidic mixing. (c) Time series images of numerical simulation (in 2D) of the acoustofluidic mixing effect to homogenize the concertation gradients. A concentration gradient is assumed to be established already in the chamber by having alternating bands of 0 and 10^{-10} mol/m³, and acoustofluidic mixing was applied as explained before in the acoustofluidic mixing section. (d) Analysis of the experimental microfluidic staining gradients (ratio of the lowest over the highest fluorescent intensity). Different flow rates and incubation times were used (300 µl/min for 1, 2, and 4-min incubation time and 900 and 1500 µl/min for 1 min incubation time), all without acoustofluidic mixing, and finally 300 µl/min with 1 min incubation time with acoustofluidic mixing, the latter condition showing the absence of the staining gradients.*

Here, to reduce the numerical simulation complexity, we have assumed that a concentration gradient is already established in the chamber and the acoustofluidic mixing is applied from the left side at 6.5 kHz, as explained before in the acoustofluidic mixing section. The concentration gradient was established using alternating concentration bands of 0 and 10^{-10} mol/m^3, which resemble the implication of the low and high concentration bands achieved with the distributed channel network chip. The time series images show that the acoustofluidic mixing will induce a large-scale transversal motion that disrupts the laminar flow streams and induces the mixing perpendicularly between the flow lines.

Figure 4.4d shows the statistical analysis of experimental microfluidic gradients experienced by the Bt-474 sections at a flow rate of 300 µl/min after 1, 2, and 4 min of each antibody incubation time, and 900 and 1500 µl/min after 1 min of antibodies incubation time, without the acoustofluidic mixing. In all cases, a similar and large volume of 350 µl of each antibody was dispensed to ensure a full filling of the fluidic tubes and the microfluidic chamber. The low and high fluorescence intensities are measured at the Bt-474 sections affected by the slow flow rate and high flow rate, respectively, as shown in Figure 4.4b. Several locations of the low (n=3) and high (n=3) staining signal bands were considered for the analysis. It is evident that, with slower flow rates, the differences between the microfluidic gradients are higher, as indicated before in the numerical analysis (Figure 4.4a) and this leads to higher differences between the neighboring tissue spots. Moreover, with a low flow rate of 300 µl /min, but with increasing the incubation time from 1 to 2 and 4 min, the differences between the adjacent tissue bands tend to be less (low/high bands intensity signal increases on average from 67% at 1 min to 84% at 4 min for both markers). This can help in decreasing the non-homogeneity in the tissue section staining but at the cost of increasing the incubation time. On the other hand, higher flow rates are capable of dispensing the fluid, while rapidly diminishing the differences between the adjacent microfluidic gradient bands, thus leading to fewer differences in the tissue staining. However, higher flow rates generally require some considerations as explained before such as the need for a high-pressure pump, and very firm sealing of the microfluidic chamber otherwise there is a risk of leakage during the experiment, and the associated high tangential shear stress acting on the biological samples being diagnosed. Moreover, Figure 4.4c shows the effect of the acoustofluidic mixing on diminishing the microfluidic staining gradients for the most non-homogenous experimental settings (300 µl/min and 1 min of incubation time). This shows the clear potential of using acoustofluidic mixing for experiments that require low-pressure pumps or are prone to a potential microfluidic leakage or prone to adverse effects on the tissue or cells due to the high shear stress associated with high flow rates.

4.4.3 Acoustofluidics enabling faster immunoassays

Microfluidic systems may suffer from the laminar flow regime, where the fluid travels in parallel layers without eddies, swirls, or any disruption between the fluidic layers and thus mixing may solely proceed through diffusion. Molecular diffusion in a static fluid (low Péclet values) is the main mechanism of transport in zero-flow microfluidic systems, which relies on several factors including the inverse of the

particle radius or molecule size[37]. This means that particles or reagent molecules with larger sizes have lower diffusion coefficients, leading to possibly very slow diffusional transport in microfluidic systems. Biological reagents have diffusion coefficients in the range of 10^{-11} to 10^{-12} m^2/sec, which means they would need a long time to diffuse across a microfluidic chamber. The implication of this limited transport can be highly adverse on the duration of microfluidic immunoassays, as explained later.

Figure 4.5a shows a time series of the simulated reagent concentration over the chamber cross-section, as indicated by the dashed-blue line box in Figure 4.1e; it shows by numerical simulation the development of a depletion region over the reacting tissue. At the beginning of the immunoassay incubation time, the reacting tissue surface starts to consume the available reagents in the volumetric vicinity of the tissue and thus the concentration of the available reagents starts to drop. After that, the immunoreaction starts to be limited to the slow diffusion of the reagents (large Damköhler values) to be able to reach the reacting surface. Figure 4.5b shows the reaction kinetics of the reacting tissue surface (shown in Figure 4.5a with a static incubation), where the inset plot of the Figure 4.5b shows the non-linear increase in the surface reacting species concentration (mol/m^2) over the incubation time. Figure 4.5b shows the change in the reaction rate of the adsorbing species over the incubation time. It shows that the reaction rate decays rapidly even in the first 20 sec of the reaction, dropping to 50% of the initial reaction rate. The rate further decays to 25% after 70 sec and later to 12.5% after 120 sec. Here we simulated a reacting surface with a large available density of sites (3.3×10^{-8} mol/m^2) to ensure that the reacting surface is not reaching any saturation during the simulated incubation time. The surface adsorbed concentration after 120 sec is still as low as 3.7×10^{-16} mol/m^2. A hypothetical reaction that is not limited by the diffusion transport would show a non-decaying reaction rate. This observed decrease clearly shows the effect of the slow diffusion transport of the bioreagents on the microfluidic immunoassay kinetics. Several microfluidic mixing methods in literature have been utilized to reduce this limitation, and have been shown to enhance the reaction rate as explained before. Here, we have utilized acoustofluidic mixing to counteract this diffusion-limited transport for the immunoassay on the Bt-474 cancer cells. Several immunostaining experiments were conducted with different incubation times of the primary and secondary antibodies, as explained before, all at a 1:200 dilution ratio. After the sections were stained and mounted for imaging, the signal and background values were analyzed, as explained in the Methods & protocols section 4.6. A 5 min incubation time of each antibody mixture was tested without the acoustofluidic (non-AF) mixing while, incubation times of 4, 3, 2, and 1 min with the acoustofluidic (AF) mixing were tested, with each of the above conditions repeated (n=3) to ensure the reproducibility of the observed effects.

In general, given the rapidly decaying reaction rate observed in Figure 4.5b, shortening the incubation time is expected to reduce the achieved reaction signal by a large factor. The surface reacting species concentration shown in the inset plot of Figure 4.5b shows that the signal would decrease from 3.7×10^{-16} to 1.9×10^{-16} mol/m^2 if the incubation time is shortened from 2 to 1 min. However, one sees in Figure 4.5c that, even with shortening the incubation times down by 80% with the active actuation of the piezoelectric transducers, the acoustofluidic mixing is capable of rapidly replenishing the bioreagents over the reacting tissue. We have found that the acoustofluidic mixing with shorter

incubation times is not only capable of sustaining the immuno-fluorescence signal, but it further provides higher signals. With the shortest incubation time of 1 min, on average, 25% of the Her2 and CK signals were achieved higher than the 5 min incubation time without acoustofluidic mixing. This shows the potential of using the acoustofluidic mixing to shorten the immunoassay incubation times, while still achieving higher signal-to-noise ratios. It is worth noting that the increase in the percentage

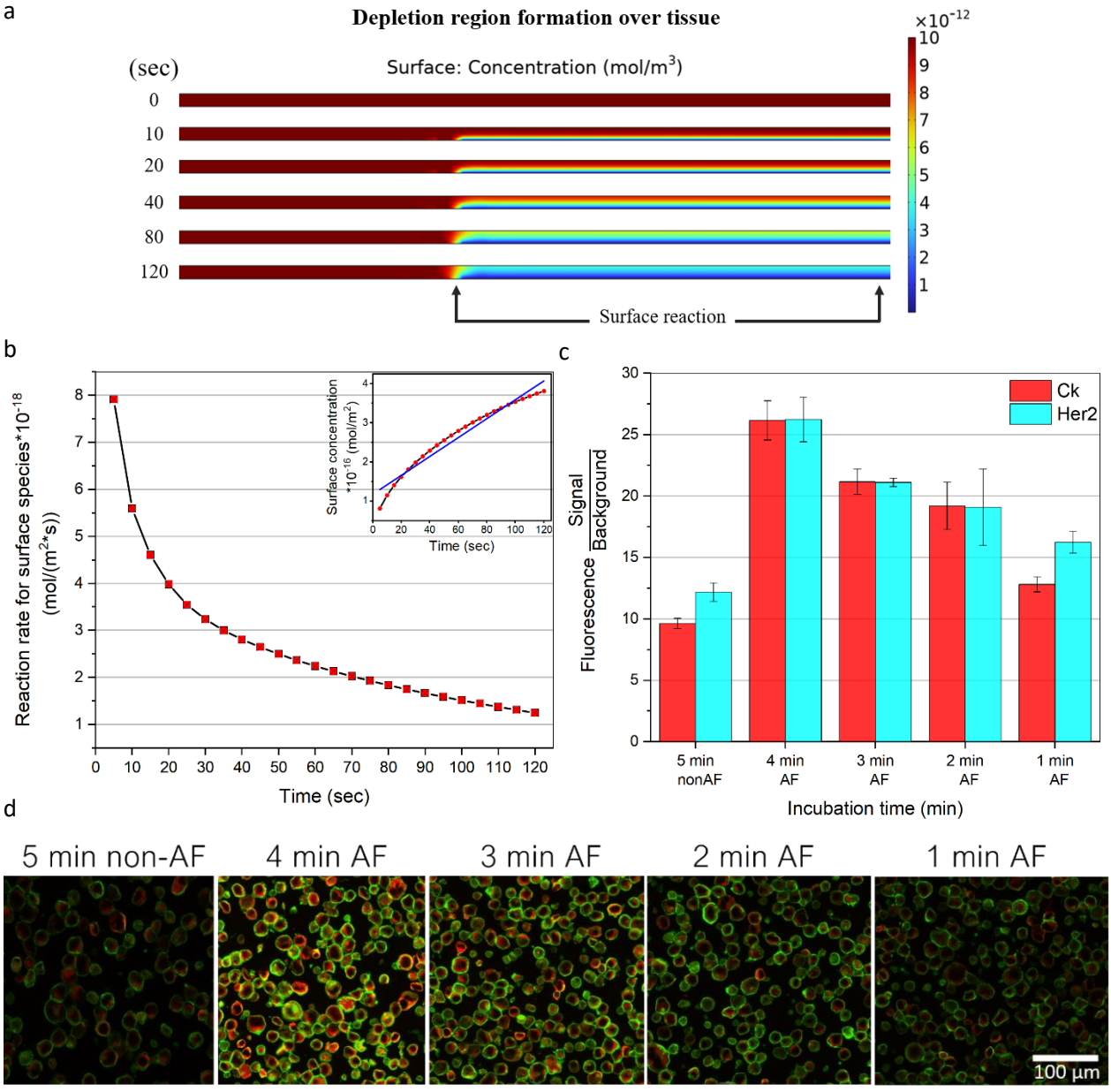

Figure 4.5 Reagent concentration depletion region near a reacting surface and acoustofluidic-enhanced immunostaining. *(a) Time series images (0 to 120 sec) of the chamber cross section (indicated by the dashed-blue line box in Figure 4.1e) showing the reagent concentration depletion over the reacting surface tissue. The initial reagent concentration is 10^{-11} mol/m³ simulated in a microfluidic chamber (17×17×0.05 mm³), under static incubation (no fluid dispensing). (b) Reaction rate (mol/(m².sec)) of the surface species during the incubation time of 120 sec, corresponding to Figure 4.5a. The inset plot of Figure 4.5b shows the non-linear increase in the surface reacting species (mol/m²) over the 120 sec incubation time. (c) Signal/background experimental fluorescence analysis of the Her2 and CK markers on the Bt-474 cancer cells, for 5 min incubation time without acoustofluidic (non-AF) mixing and 4-, 3-, 2-, and 1-min incubation time with acoustofluidic (AF) mixing. Error bars represent the standard deviation (n=3). (d) Fluorescence microscopic images of Bt-474 cancer cells showing the Her2 (green) and CK (red) signals at the different experimental conditions; 5 min incubation time without acoustofluidic (non-AF) mixing and 4-, 3-, 2-, and 1-min incubation time with acoustofluidic (AF) mixing.*

average of the immuno-fluorescence signal with the acoustofluidic from 1 to 4 min over the 5 min static incubation, is lower with the Her2 marker than with the CK. Several factors can lead to this observation, such as the number of the protein epitopes available on the cells for each marker, but it is worth considering that the Her2 receptors are embedded and highly localized in the cellular membrane[300], while the CK are mainly found on the cytoplasm and nucleus[301]. This can potentially show the effect of the microfluidic mixing on the enhancement of the cellular markers that are localized more inside the cells than those on the outside membrane. A similar observation is made with the acoustofluidic mixing at different reagent concentrations. Finally, Figure 4.5d shows the immunofluorescent staining of the BT-474 cancer cell sections at the different experimental conditions of 5 min incubation times without acoustofluidic mixing, and 4-, 3-, 2-, and 1-min incubation times with acoustofluidic mixing. A higher and sharper signal is observed for both the Her2 (green color) membranous marker and the CK (red color) cytoplasmic markers.

4.4.4 Acoustofluidics enabling immunoassays with lower reagents consumption

The concentration of the biological reagents (antibodies, DNA, proteins, aptamers, etc.) used in an immunoassay is an important factor, since these molecules are generally expensive. A high concentration would result in a higher signal, as long as it doesn't adversely affect the immunoassay performance, for example, due to steric repulsion or increasing the non-specific signal, however, that adds a high cost to the analysis. It is noteworthy that, without the acoustofluidic mixing, normalizing the reaction rates of four different simulated concentrations (from 10^{-10} to 0.25×10^{-10} mol/m^3) to the initial concentration of the reacting reagents, shows an equal value for all of the four different concentrations at the same time, as shown by Figure 4.6. This indicates that the change in the reaction rates over the incubation time is not affected by the concentration used and that the system is highly affected by the diffusional limited transport of the reacting reagents, as explained before. At the same time, a higher initial concentration means a higher assay signal. This is shown by Figure 4.7a, which shows the simulation results of the surface concentration achieved after 4 min of incubation time at the four different reagent concentrations (dilutions). It shows clearly that, with a higher initial reagent concentration in the chamber, a higher signal (without reaching surface saturation) is achieved after the same incubation time, while the other lower concentrations (50%, 66.67%, and 75% less concentration than 10^{-10} mol/m^3) showed much lower surface concentrations, scaling nearly with the same dilution percentages. This is mainly due to the high abundance of the bioreagents in the vicinity of the reacting surface (tissue) when using high concentrations. Thus, within the same incubation time, there is a higher limitation imposed on the immunoassay reaction with lower concentrations of the bioreagents due to the scarcity of the bioreagents and the slow diffusional transport.

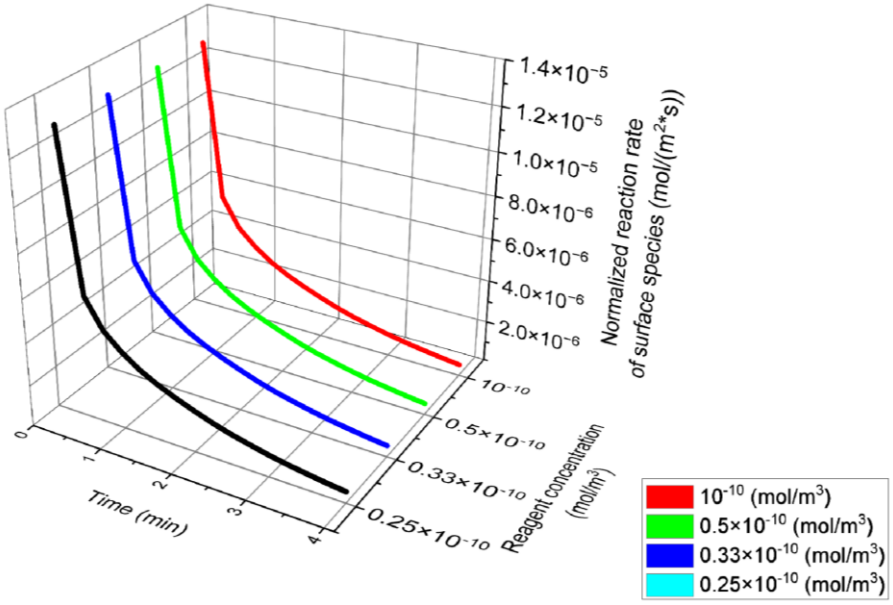

Figure 4.6 Normalized surface reaction rate (numerical simulation). *Different reagents concentrations from 0.25×10^{-10} to 10^{-10} mol/m³ were simulated during the incubation time of 4 min.*

Therefore, acoustofluidic mixing can be a helpful tool here too to mix and replenish the fluid containing the bioreagents over the reacting surface. Figure 4.7b shows the experimental analysis (signal/background fluorescence signal) of the Bt-474 cancer cell pellet sections, immune-stained with the Her2 and CK markers, with 4 min incubation times of the different dilution ratios of the primary and secondary antibodies. A dilution ratio of 1:100 was tested without the acoustofluidic mixing, and dilution ratios of 1:200, 1:300, and 1:400 were tested with the acoustofluidic mixing. As clearly seen, and contrary to what might be expected if a static incubation is used, going to higher dilutions of the primary and secondary antibodies with the acoustofluidic mixing achieved a higher signal over the more concentrated antibodies but with a static incubation. Analogous to the reduction in the incubation time with the acoustofluidic mixing before, reducing the antibodies consumption by 50% and 66.6% with the acoustofluidic mixing not only reduces the experimental cost but also provides a higher signal-to-background ratio. 1:200 and 1:300 dilution rates with the acoustofluidic mixing showed an increase in the signals by 35% in CK and 12% in Her2 and 25% in CK and 6% in Her2, respectively, over the 1:100 dilution rate without the acoustofluidic mixing. However, a 1:400 dilution rate with the acoustofluidic mixing resulted in lower signals (7% in CK and 17% in Her2). Finally, Figure 4.7c shows the immunofluorescent images of the BT-474 cell pellet sections at the different antibodies' dilution ratios of 1:100 without the acoustofluidic mixing, and 1:200, 1:300, and 1:400 with the acoustofluidic mixing. A higher signal is observed for Her2 and CK markers even with the 1:200 and 1:300 dilution rate of the antibodies when the acoustofluidic mixing is used. This shows the possibility of using acoustofluidic mixing to achieve higher immunoassay signal-to-noise ratios while consuming lower volumes of the expensive bioreagents.

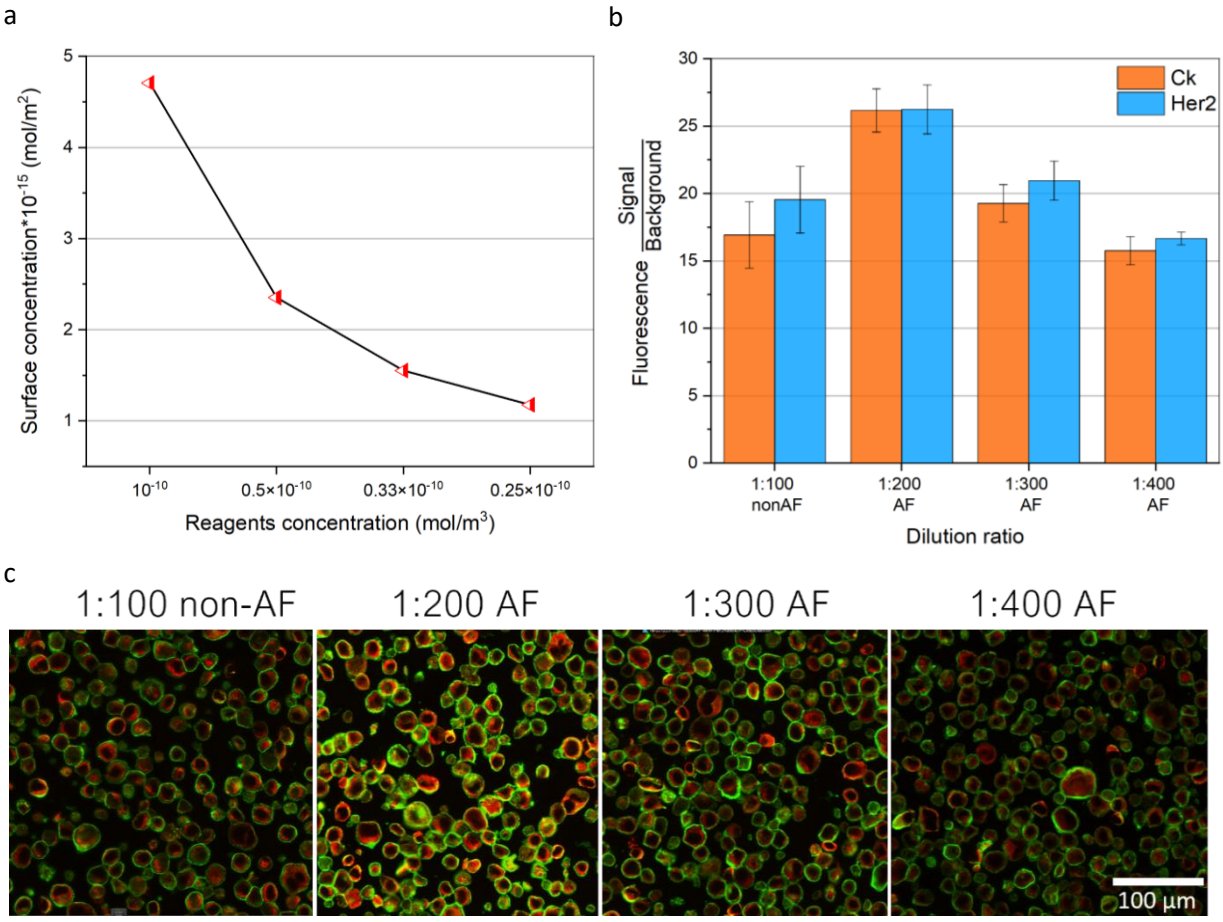

Figure 4.7 Acoustofluidic enhanced immunoassays resulting in lower reagents consumption. *(a) Simulation of the surface reacting species concentration (mol/m^2) obtained after 4 min using different initial reagents concentrations of 10^{-10}, 0.5×10^{-10}, 0.33×10^{-10}, 0.25×10^{-10} mol/m^3 inside the chamber shown in Figure 4.5a. (b) The signal/background experimental fluorescence analysis of the Her2 and CK markers on the Bt-474 cancer cells, at 1:100 antibodies dilution rate without acoustofluidic (non-AF) mixing and at 1:200, 1:300, and 1:400 antibodies dilution rates with acoustofluidic (AF) mixing, all with 4 min of incubation time. Error bars represent the standard deviation (n=3). (c) Fluorescence microscopic images of Bt-474 cancer cells showing the Her2 (green) and CK (red) signals at the different experimental conditions; 1:100 antibodies dilution rate without acoustofluidic (non-AF) mixing and at 1:200, 1:300, and 1:400 antibodies dilution rates with acoustofluidic (AF) mixing, all with 4 min of incubation time.*

4.5 Conclusion

The integration of microfluidics for automated and rapid immunoassays has garnered significant interest in recent decades. However, challenges arise due to the reconciliation of laminar flow patterns in micro-scale systems with diffusion-limited mass transport. To address this issue, various methods, including acoustic-based fluidic streaming, have been investigated to enhance microfluidic mixing. In this study, we utilize numerical simulations and experiments to demonstrate the beneficial effect of acoustic agitation on the uniformity of immunostaining in large-sized and thin microfluidic chambers. Furthermore, we investigate the impact of reducing incubation times and concentrations of biochemical detection reagents on the obtained immunoassay signal through numerical simulations. Remarkably, acoustofluidic mixing successfully reduces the incubation time of Her2 and CK biomarkers by 80% for spatial immunostaining of breast cancer cell pellets, or reduces their

concentration by 66%, while achieving a higher signal-to-background ratio compared to immunoassays with static incubation. These findings highlight the potential of acoustic-based fluidic streaming as a promising approach for enhancing microfluidic immunoassays, allowing for faster and more efficient detection of biomarkers in complex biological samples.

4.6 Methods & protocols

4.6.1 Numerical simulation protocols

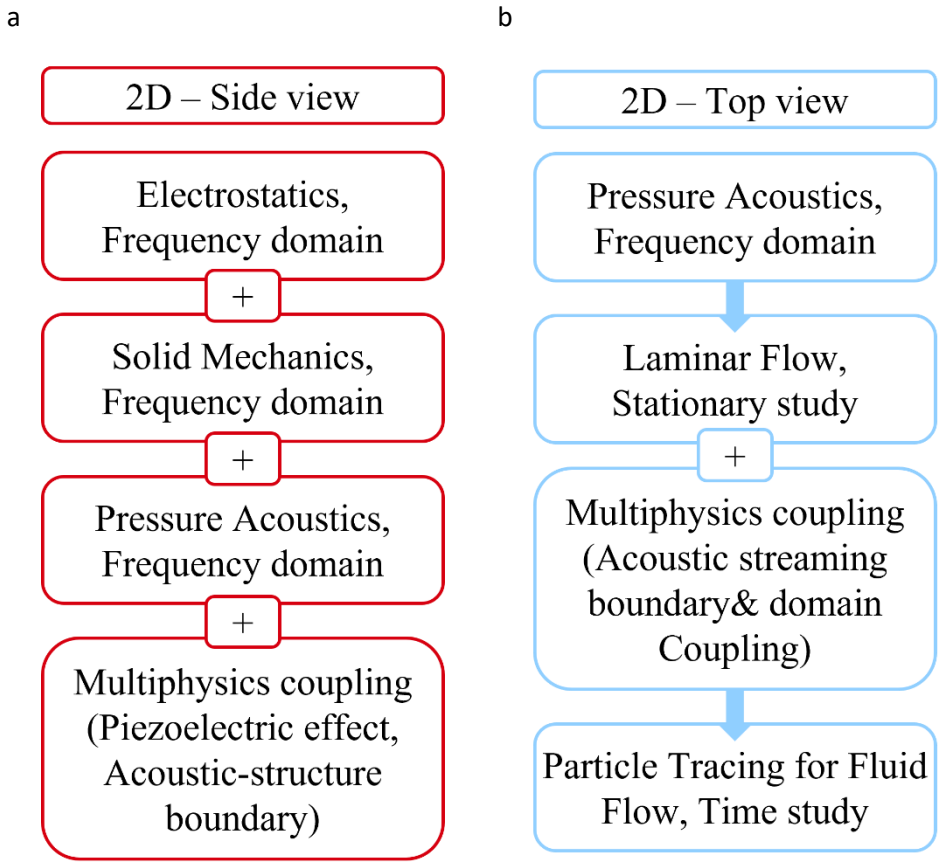

Figure 4.8 Pipeline of the numerical simulation strategy. *Top (a) and side (b) view simulation protocols of the microfluidic system, showing the order of the physics simulation and the Multiphysics modules coupling.*

4.6.2 Immunoassay and imaging protocols

Preparation and blocking:

A BT-474 FFPE cell pellet block (Amsbio) was sectioned (5 µm thick slices) and loaded on Superfrost Plus adhesion microscopic slides (Epredia). Before the immunostaining, the cell pellet sections were dewaxed and deparaffinized using the PT module (Epredia) for 1 hour into the Dewax and HIER Buffer H (PH 9) at 102 °C. After that, the slides were kept in TBST (Tris-buffer saline with 0.005% tween-20) until the blocking step. The slides were then quenched for 2 minutes with Quenching buffer 1x (BU08-L, Lunaphore) diluted into TBS buffer (Tris-buffer saline). The slides were then washed thoroughly with TBST (TBS-tween) and then incubated for 5 minutes with bovine serum albumin (3%, AURION BSA-c, diluted in staining buffer). Finally, the slides were washed thoroughly and then kept in TBS till the immunostaining step.

Immunostaining:

The slides were then loaded into the microfluidic system shown in Figure 4.1a and the following bioassay protocol was used for all the slides. The BT474 cell sections were first incubated with a mixture of Her2/Neu (EP3) rabbit monoclonal primary antibody (237R-25-ASR, Cell marque) and Cytokeratin (Concentrate) mouse monoclonal primary antibody (M351501, Agilent) at the described dilution ratio and incubation time of each experimental section. The slides were then washed thoroughly with TBST and subsequently incubated with a mixture of goat anti-rabbit IgG highly cross-adsorbed secondary antibody-Alexa Fluor Plus 647 (A32733, Thermofisher) and goat anti-mouse IgG highly cross-adsorbed secondary antibody-Alexa Fluor Plus 555 (A32727, Thermofisher) at the described dilution ratio and incubation time of each experimental section. The primary and secondary antibodies were diluted into 1x TBST. Dapi (62248, Thermofisher) was diluted to 1:1000 with the secondary antibodies and used for nuclear counterstaining. After washing thoroughly with TBST, the slides were unloaded from the microfluidic stainer system for microscopic imaging.

Fluorescence microscopic imaging and analysis:

Finally, the slides were mounted with coverslips using the SlowFade Gold mounting medium (S36936, Invitrogen) for microscopic imaging. The slides were imaged using the PANNORAMIC MIDI II automatic slide scanner (3DHISTECH) with SOLA Light illumination engine (Lumencor). The focal level was adjusted for each imaging tile, and the whole cell-pellet section was imaged using a 20x (NA 0.8) objective. The exposure time was adjusted for each slide to avoid over- or under-exposure of the cell sections, and the different exposure times were considered during the image analysis. A similar region-of-interest (ROI) size for all the images was exported and analyzed using a CellProfiler (4.2.1) pipeline. Briefly, an adaptive Otsu thresholding was used to classify the Her2 and Ck signal for each cell and assigned it as Signal, and the inverse mask was used as Background to account for any fluorescent signal coming from outside the cells.

For the visualization of acousto-fluidic streamlines, several sizes of fluorescent microparticles (4, 4.96, 8.87, 10.14 µm) were diluted in TBST buffer and imaged by 4x objective.

Infrared thermal imaging:

An infrared thermal camera (PI 640i, Optris), was used for the thermal monitoring at a frequency of 31 Hz during the actuation of the acoustic transducers.

5 Conclusion and future perspectives

5.1 Achieved results

In this work, we have investigated several methods for enhancing the performance of microfluidic applications for spatial proteomic analysis for cancer diagnostics.

First, a novel electrode design leading to more efficient ACET patterns and improved immunoassays has been presented. The design has two commonly side electrodes biased and tilted versus a middle electrode to generate two counter-rotating in-plane fluidic vortices. A comparison with the more traditional ACET parallel electrodes` design was investigated. We demonstrated that the new design can provide microfluidic mixing over an increased volume in a microfluidic cell, leading to an enhanced reaction between the reagents in the fluid and the target antigen surface. Both numerical simulation and experimental validation have been used to illustrate the working concept of the new design. Additionally, numerical simulation of an ACET-enhanced surface-based assay has been shown. Moreover, the interplay between experimental conditions (association constant of the reaction, reagent concentration) and the ability of the microfluidic mixing to enhance surface-based reactions has been illustrated. Furthermore, an experimental proof of concept of the ACET-enhanced immunofluorescent staining on cancer cells was shown, using the traditional parallel and the newly proposed in-plane design. Moreover, the design concept has been investigated, both by simulation and experiments, on its scalability potential: larger designs (longer electrodes and larger gaps) are capable of fluid mixing over larger microfluidic volumes and thus enhance further the immunoassays. This effectively led to an enhancement of 6 times in the assay output signal and a 75% reduction in the assay time. This can be valuable for having more accurate and faster diagnostics.

Next, we have carried out a systematic study of the in-plane ACET design. We have elaborated further on the working concept and the comparison between the parallel and in-plane ACET designs, and how the tilted electrode design can create a biased ACET effect leading to the in-plane fluidic motion. We then have shown how the tilting angle between the side and the middle electrode can affect the induced in-plane fluid motion, the ACET fluid velocity, and the temperature achieved due to the Joule heating effect. Moreover, we have investigated the possibility to have some DEP interference affecting the achieved ACET microfluidic motion. In addition to that, new microelectrode designs, based on the working concept of the biased geometry of the tilted electrodes, have been shown and investigated by numerical simulation and experimental validation to achieve the in-plane fluidic motion. The new designs are capable of providing four in-plane semi-circular fluidic motions, and one design has been investigated by modeling microparticles` tracing and further confirmed its motion by experiments. Finally, an arc design has been proposed and investigated for ACET microfluidic pumping applications. The design array has been modeled by numerical simulation for the induced fluidic motion, and some characterization insights have been discussed to be taken into consideration for the ACET pumping

design. Microparticles` tracing has been then used to illustrate the microfluidic pumping using the arc design.

The application of microfluidic systems for spatial proteomic and transcriptomic analysis on large-size tissues (up to 6 mm long and 2.5 mm wide) has left us with the question of how to provide large-scale microfluidic mixing. The scaled-up in-plane ACET design and the proposed alternatives can be solutions to induce large-scale mixing, but as per our experience, the mixing and the corresponding enhancement in the immunoassays` staining are not spatially homogenous. Moreover, further improvements of the applications in different forms are needed, such as the ease of integration of the solution and especially on the industrial scale, the cost efficiency, and the limited side-effects as compared to the alternative solutions.

Therefore, we have investigated the integration of acoustofluidic streaming for microfluidic mixing and for enhancing microfluidic immunoassays for cancer diagnostics. Piezoelectric elements were mounted close to the microfluidic chamber and were capable of inducing large-scale acoustic streaming vortex-like patterns. Numerical simulation was conducted to explain the working concept of acoustofluidic mixing in microfluidic systems. After that, the possibility of obtaining non-homogenous staining of tumor tissues using a microfluidic chip with network channel design at low fluidic flow rates was investigated by simulation and experiments. Additionally, we have elaborated by numerical simulation on how the shorter incubation times and the lower reagent concentrations, and their diffusion-limited transport inside microfluidic systems can be an obstacle against the enhancement of the microfluidic immunoassay performance. Finally, acoustofluidic mixing was used for improving the immunostaining of Her2 and Ck markers on BT-474 cancel cell pellet sections. Acoustofluidic mixing was capable of providing homogeneous and uniform staining, even at conditions that would generate a very sharp concentration and staining gradients at static incubation. Moreover, acoustofluidic mixing further enhanced the immunoassay performance by reducing the regent incubation time by 80% and the reagent concentration by 66%, while obtaining a higher signal than with static incubation. The reported method therefore can serve as a good approach for obtaining faster and cost-effective diagnostic assays in microfluidic systems.

5.2 Future perspectives

Generally speaking, the integration of microfluidic mixing technologies for different applications would require first answering the golden question, if the application of interest with the given microfluidic chamber design and the reagents to be used would benefit from mixing? And to which extent? We have seen that a system can be limited due to the limited mass transport and the slow diffusion of the reagents, but it can be also limited due to the reaction rate kinetics and thus mixing wouldn’t help. On the other hand, it can be limited due to the low abundance of the target markers in the sample, and thus it is expression-limited. In this case, target or signal amplification techniques are needed. At the same time, the system not always will be experiencing only one of these limitations categories but can be experiencing a combination of them. Therefore, a deep understanding and

characterization of the full system can be highly valuable to achieve the optimum system performance.

ACET technology has been shown to achieve efficient microfluidic mixing and enhance the immunoassay signal. Here we discuss our future perspectives and considerations for the technology. One application that can obtain the maximum benefit from the ACET mixing but also from the generated temperature is that of the polymerase chain reaction (PCR. In PCR, short synthetic DNA fragments are used to amplify a segment of the genome, through a multiple round of denaturation, annealing, and extension steps. Each step has to be done at a specific temperature, and therefore, several microfluidic devices have been suggested to automate this process [302,303]. For example, space-domain PCR systems have been proposed where the sample is moved through different microchannels with different temperatures along the system length. However, these systems need long and well-thermally characterized microchannels. Additionally, time-domain PCR systems have been also implemented where the amplification of the stationary sample is carried out through active cooling and heating. However, these systems can limit the PCR throughput due to the time needed to achieve heating and cooling of the stationary sample, and similarly, would require an efficient control of the microfluidic chamber temperature. Here, we believe that the ACET In combination with the natural heat convection through a well-designed microfluidic system can offer an alternative for efficient and rapid PCR. ACET can offer a hot spot while the natural heat convection within the fluid and the heat capacity and heat dissipation through chamber materials can offer the temperature gradients needed for the different PCR steps. This would eliminate the need for long microchannels, or the integration of the time-limiting fast and active heating/cooling elements (e.g. Peltier elements). In parallel, ACET can offer sample mixing and translocation within the chamber thus enhancing the PCR throughput. At the same time, the newly proposed ACET design with its in-plane microfluidic motion can offer further improvements (as compared to the vertical ACET) by agitating larger volumes of the fluid.

Further improvements of the ACET can be achieved with the integration of transparent metallic electrodes such as indium tin oxide (ITO) for the ACET actuation, which can help provide imaging accessibility throughout the microfluidic chamber. This can eliminate the need to unmount the sample for the subsequent imaging and analysis, and could possibly pave the way for continuous real-time measurements and monitoring of reaction kinetics. It has to be considered also that the ACET-induced temperature can affect the stability and performance of the used reagents, such as the non-specific binding of antibodies at high temperatures and the limited temperature range at which enzymes work efficiently. Therefore, negative controls have to be done to ensure the safe application of the ACET. Similarly, the ACET can interfere with the kinetic rates of the bioreagents and this has to be optimally considered with the numerical simulation analysis.

Acoustofluidic technology, on the other hand, has been proven to provide efficient and large-scale microfluidic mixing and can be integrated for different applications, while satisfying different requirements such as the low cost and ease of integration. Numerical modeling can help us obtain advanced insights into the system performance and hardware considerations for different applications. The acoustofluidic technology, even though it has been widely investigated by the

scientific community, by our experience still requires improved numerical modeling to make it more accessible to different researchers. This task lies in the hand of skilled software researchers and simulation software companies so that a wide range of basic to advanced application examples of the larger scientific community can be addressed.

It can be highly interesting to investigate the application of the acoustofluidic technology for concentrating and trapping the detection reagents at specific locations in 3D and over the target sample with the possibility to translocate them. We believe this would require advanced and more complicated acoustofluidic integration schemes, but this approach can offer a 3D constant supply of the reacting reagents closer to the sample and can potentially reduce further the reagents consumption. Microfluidic technology is also investigated for building and growing spheroids and organoids on a chip. The organoid technology on a chip might look different from the applications listed in this study such as the immunoassays and spatial proteomic analysis. However, we foresee that the future of efficient medical diagnostics can be by harvesting and spatially directing a few cells derived from a patient to grow an organoid, human organs, and *in vitro* tissues. Subsequently, a large set of applications and analysis possibilities can be carried out such as drug screening, sequencing, and even spatial proteomic analysis on more preserved tissue samples.

Finally, the application of the *in-situ* hybridization technique for spatial transcriptomic analysis on tissue samples can potentially benefit from the acoustofluidic technology. Commonly, the spatial transcriptomic protocols are lengthy with tens of experimental steps, which can limit the application throughput. Secondly, it can include enzymatic reactions for the amplification of the target sequence, and therefore, mixing technologies such as the ACET can interfere with the optimum temperature for the enzymatic reaction. Thirdly, the microfluidic flow rate might be limited to lower values, since some of the used reagents are provided by manufacturing companies to be diluted in viscous solutions, and thus, higher flow rates can induce air bubbles in the system. Similarly, we have experimentally seen that the frozen tissue samples, which preserve the DNA, RNA, and native proteins better than the FFPE, can be delaminated with high fluid flow rates. Therefore, acoustofluidic mixing technology can be helpful here to speed up the process, eliminate the non-homogenous staining resulting from the low fluid flow rates, and avoid the generation of bubbles. Moreover, it can offer microfluidic mixing without any thermal interference with the enzymatic reactions, while paving the way for improved sample imaging through the system, especially if several rounds of fluorophore barcodes are needed to analyze several genes or protein markers simultaneously.

Bibliography

1. Sackmann EK, Fulton AL, Beebe DJ. The present and future role of microfluidics in biomedical research. Nature. 2014;507:181–9.

2. He S, Joseph N, Feng S, Jellicoe M, Raston CL. Application of microfluidic technology in food processing. Food Funct. 2020;11:5726–37.

3. Gao H, Yan C, Wu W, Li J. Application of Microfluidic Chip Technology in Food Safety Sensing. Sensors. 2020;20:1792.

4. Park D, Kim H, Kim JW. Microfluidic production of monodisperse emulsions for cosmetics. Biomicrofluidics. 2021;15:051302.

5. Alberti M, Dancik Y, Sriram G, Wu B, Teo YL, Feng Z, et al. Multi-chamber microfluidic platform for high-precision skin permeation testing. Lab Chip. 2017;17:1625–34.

6. Jokerst JC, Emory JM, Henry CS. Advances in microfluidics for environmental analysis. Analyst. 2011;137:24–34.

7. Kung CT, Hou CY, Wang YN, Fu LM. Microfluidic paper-based analytical devices for environmental analysis of soil, air, ecology and river water. Sensors and Actuators B: Chemical. 2019;301:126855.

8. Samiei E, Tabrizian M, Hoorfar M. A review of digital microfluidics as portable platforms for lab-on a-chip applications. Lab Chip. 2016;16:2376–96.

9. Ortseifen V, Viefhues M, Wobbe L, Grünberger A. Microfluidics for Biotechnology: Bridging Gaps to Foster Microfluidic Applications. Frontiers in Bioengineering and Biotechnology [Internet]. 2020 [cited 2023 Jan 12];8. Available from: https://www.frontiersin.org/articles/10.3389/fbioe.2020.589074

10. Berlanda SF, Breitfeld M, Dietsche CL, Dittrich PS. Recent Advances in Microfluidic Technology for Bioanalysis and Diagnostics. Anal Chem. 2021;93:311–31.

11. Forigua A, Kirsch RL, Willerth SM, Elvira KS. Recent advances in the design of microfluidic technologies for the manufacture of drug releasing particles. Journal of Controlled Release. 2021;333:258–68.

12. Ren K, Zhou J, Wu H. Materials for Microfluidic Chip Fabrication. Acc Chem Res. 2013;46:2396–406.

13. Reboud J, Xu G, Garrett A, Adriko M, Yang Z, Tukahebwa EM, et al. Paper-based microfluidics for DNA diagnostics of malaria in low resource underserved rural communities. Proceedings of the National Academy of Sciences. 2019;116:4834–42.

14. Shen K, Chen X, Guo M, Cheng J. A microchip-based PCR device using flexible printed circuit technology. Sensors and Actuators B: Chemical. 2005;105:251–8.

15. J. Easley C, M. Karlinsey J, P. Landers J. On-chip pressure injection for integration of infrared-mediated DNA amplification with electrophoretic separation. Lab on a Chip. 2006;6:601–10.

16. Ellett F, Jorgensen J, Marand AL, Liu YM, Martinez MM, Sein V, et al. Diagnosis of sepsis from a drop of blood by measurement of spontaneous neutrophil motility in a microfluidic assay. Nat Biomed Eng. 2018;2:207–14.

17. Chin CD, Laksanasopin T, Cheung YK, Steinmiller D, Linder V, Parsa H, et al. Microfluidics-based diagnostics of infectious diseases in the developing world. Nat Med. 2011;17:1015–9.

18. Zhou X, Liu D, Zhong R, Dai Z, Wu D, Wang H, et al. Determination of SARS-coronavirus by a microfluidic chip system. ELECTROPHORESIS. 2004;25:3032–9.

19. Huang S, Li C, Lin B, Qin J. Microvalve and micropump controlled shuttle flow microfluidic device for rapid DNA hybridization. Lab on a Chip. 2010;10:2925–31.

20. Bernacka-Wojcik I, Lopes P, Catarina Vaz A, Veigas B, Jerzy Wojcik P, Simões P, et al. Bio-microfluidic platform for gold nanoprobe based DNA detection—application to Mycobacterium tuberculosis. Biosensors and Bioelectronics. 2013;48:87–93.

21. Tay A, Pavesi A, Yazdi SR, Lim CT, Warkiani ME. Advances in microfluidics in combating infectious diseases. Biotechnology Advances. 2016;34:404–21.

22. Zhang W, Lee WY, Siegel DS, Tolias P, Zilberberg J. Patient-Specific 3D Microfluidic Tissue Model for Multiple Myeloma. Tissue Engineering Part C: Methods. 2014;20:663–70.

23. Mazzocchi AR, Rajan SAP, Votanopoulos KI, Hall AR, Skardal A. In vitro patient-derived 3D mesothelioma tumor organoids facilitate patient-centric therapeutic screening. Sci Rep. 2018;8:2886.

24. S. Shirure V, Bi Y, B. Curtis M, Lezia A, M. Goedegebuure M, Peter Goedegebuure S, et al. Tumor-on-a-chip platform to investigate progression and drug sensitivity in cell lines and patient-derived organoids. Lab on a Chip. 2018;18:3687–702.

25. Lorenz T, Bojko S, Bunjes H, Dietzel A. An inert 3D emulsification device for individual precipitation and concentration of amorphous drug nanoparticles. Lab Chip. 2018;18:627–38.

26. Theberge AB, Mayot E, Harrak AE, Kleinschmidt F, Huck WTS, Griffiths AD. Microfluidic platform for combinatorial synthesis in picolitre droplets. Lab Chip. 2012;12:1320–6.

27. Wei Y, Zhu Y, Fang Q. Nanoliter Quantitative High-Throughput Screening with Large-Scale Tunable Gradients Based on a Microfluidic Droplet Robot under Unilateral Dispersion Mode. Anal Chem. 2019;91:4995–5003.

28. Ultrahigh-throughput magnetic sorting of large blood volumes for epitope-agnostic isolation of circulating tumor cells | PNAS [Internet]. [cited 2023 Apr 27]. Available from: https://www.pnas.org/doi/full/10.1073/pnas.2006388117

29. Elvira KS. Microfluidic technologies for drug discovery and development: friend or foe? Trends in Pharmacological Sciences. 2021;42:518–26.

30. High-Throughput Secretomic Analysis of Single Cells to Assess Functional Cellular Heterogeneity | Analytical Chemistry [Internet]. [cited 2023 Apr 27]. Available from: https://pubs.acs.org/doi/full/10.1021/ac400082e

31. Wang J, Tham D, Wei W, Shin YS, Ma C, Ahmad H, et al. Quantitating Cell–Cell Interaction Functions with Applications to Glioblastoma Multiforme Cancer Cells. Nano Lett. 2012;12:6101–6.

32. Yamanaka YJ, Berger CT, Sips M, Cheney PC, Alter G, Love JC. Single-cell analysis of the dynamics and functional outcomes of interactions between human natural killer cells and target cells. Integrative Biology. 2012;4:1175–84.

33. Functional single-cell analysis of T-cell activation by supported lipid bilayer-tethered ligands on arrays of nanowells - Lab on a Chip (RSC Publishing) DOI:10.1039/C2LC40869D [Internet]. [cited 2023 Apr 27]. Available from: https://pubs.rsc.org/en/content/articlehtml/2013/lc/c2lc40869d

34. A Systems Approach to Measuring the Binding Energy Landscapes of Transcription Factors | Science [Internet]. [cited 2023 Apr 27]. Available from: https://www.science.org/doi/10.1126/science.1131007

35. Shin YS, Remacle F, Fan R, Hwang K, Wei W, Ahmad H, et al. Protein Signaling Networks from Single Cell Fluctuations and Information Theory Profiling. Biophysical Journal. 2011;100:2378–86.

36. Ma C, Fan R, Ahmad H, Shi Q, Comin-Anduix B, Chodon T, et al. A clinical microchip for evaluation of single immune cells reveals high functional heterogeneity in phenotypically similar T cells. Nat Med. 2011;17:738–43.

37. Draz MS, Uning K, Dupouy D, Gijs MAM. Efficient AC electrothermal flow (ACET) on-chip for enhanced immunoassays. Lab Chip. 2023;23:1637–48.

38. Jo K, Heien ML, Thompson LB, Zhong M, Nuzzo RG, Sweedler JV. Mass spectrometric imaging of peptide release from neuronal cells within microfluidic devices. Lab Chip. 2007;7:1454–60.

39. Jönsson C, Aronsson M, Rundström G, Pettersson C, Mendel-Hartvig I, Bakker J, et al. Silane–dextran chemistry on lateral flow polymer chips for immunoassays. Lab Chip. 2008;8:1191–7.

40. He H, Yuan Y, Wang W, Chiou NR, Epstein AJ, Lee LJ. Design and testing of a microfluidic biochip for cytokine enzyme-linked immunosorbent assay. Biomicrofluidics. 2009;3:022401.

41. Tan SN, Ge L, Tan HY, Loke WK, Gao J, Wang W. Paper-Based Enzyme Immobilization for Flow Injection Electrochemical Biosensor Integrated with Reagent-Loaded Cartridge toward Portable Modular Device. Anal Chem. 2012;84:10071–6.

42. Huh YS, Chung AJ, Erickson D. Surface enhanced Raman spectroscopy and its application to molecular and cellular analysis. Microfluid Nanofluid. 2009;6:285–97.

43. Drury JL, Mooney DJ. Hydrogels for tissue engineering: scaffold design variables and applications. Biomaterials. 2003;24:4337–51.

44. Cheng CM, Martinez AW, Gong J, Mace CR, Phillips ST, Carrilho E, et al. Paper-Based ELISA. Angewandte Chemie International Edition. 2010;49:4771–4.

45. Hossain SMZ, Luckham RE, McFadden MJ, Brennan JD. Reagentless Bidirectional Lateral Flow Bioactive Paper Sensors for Detection of Pesticides in Beverage and Food Samples. Anal Chem. 2009;81:9055–64.

46. Wang H, Liu Y, Liu C, Huang J, Yang P, Liu B. Microfluidic chip-based aptasensor for amplified electrochemical detection of human thrombin. Electrochemistry Communications. 2010;12:258–61.

47. Fernandez-Lorente G, Rocha-Martín J, Guisan JM. Immobilization of Lipases by Adsorption on Hydrophobic Supports: Modulation of Enzyme Properties in Biotransformations in Anhydrous Media. In: Guisan JM, Bolivar JM, López-Gallego F, Rocha-Martín J, editors. Immobilization of Enzymes and Cells: Methods and Protocols [Internet]. New York, NY: Springer US; 2020 [cited 2023 Apr 27]. p. 143–58. (Methods in Molecular Biology). Available from: https://doi.org/10.1007/978-1-0716-0215-7_9

48. Wang YC, Han J. Pre-binding dynamic range and sensitivity enhancement for immuno-sensors using nanofluidic preconcentrator. Lab Chip. 2008;8:392–4.

49. Schroeder H, Adler M, Gerigk K, Müller-Chorus B, Götz F, Niemeyer CM. User Configurable Microfluidic Device for Multiplexed Immunoassays Based on DNA-Directed Assembly. Anal Chem. 2009;81:1275–9.

50. Glass NR, Tjeung R, Chan P, Yeo LY, Friend JR. Organosilane deposition for microfluidic applications. Biomicrofluidics. 2011;5:036501.

51. Delamarche E, Bernard A, Schmid H, Michel B, Biebuyck H. Patterned Delivery of Immunoglobulins to Surfaces Using Microfluidic Networks. Science. 1997;276:779–81.

52. Wang DS, Fan SK. Microfluidic Surface Plasmon Resonance Sensors: From Principles to Point-of-Care Applications. Sensors. 2016;16:1175.

53. Joo S, Park S, Chung TD, Kim HC. Integration of a Nanoporous Platinum Thin Film into a Microfluidic System for Non-enzymatic Electrochemical Glucose Sensing. ANAL SCI. 2007;23:277–81.

54. Microfluidic cantilever detects bacteria and measures their susceptibility to antibiotics in small confined volumes | Nature Communications [Internet]. [cited 2023 Apr 27]. Available from: https://www.nature.com/articles/ncomms12947

55. A Surface Acoustic Wave Biosensor Concept with Low Flow Cell Volumes for Label-Free Detection | Analytical Chemistry [Internet]. [cited 2023 Apr 27]. Available from: https://pubs.acs.org/doi/full/10.1021/ac0207574

56. cytivalifesciences. SPR systems [Internet]. Cytiva. [cited 2023 Apr 27]. Available from: https://www.cytivalifesciences.com/en/us/shop/protein-analysis/spr-label-free-analysis/systems?sort=NameAsc&chunk=1

57. bruker. Surface Plasmon Resonance [Internet]. [cited 2023 Apr 27]. Available from: https://www.bruker.com/en/products-and-solutions/surface-plasmon-resonance.html

58. Smart Microfluidic Solutions | MicruX [Internet]. [cited 2023 Apr 27]. Available from: https://www.micruxfluidic.com/en/microfluidic-solutions/

59. Dolomite. Electrochemical sensor development kit [Internet]. Dolomite Microfluidics. [cited 2023 Apr 27]. Available from: javascript://void(0);/

60. Raman Spectroscopy | Raman Spectroscopy Instrumentation - CH [Internet]. [cited 2023 Apr 27]. Available from: https://www.thermofisher.com/uk/en/home/industrial/spectroscopy-elemental-isotope-analysis/molecular-spectroscopy/raman-microscopy/instruments.html

61. Raman Spectrometers - Agiltron Inc. [Internet]. [cited 2023 Apr 27]. Available from: https://agiltron.com/category/raman-chemical-detection-spectrometers/

62. QSense | Biolin Scientific [Internet]. [cited 2023 Apr 27]. Available from: https://www.biolinscientific.com/qsense

63. Kwon S, Cho CH, Kwon Y, Lee ES, Park JK. A Microfluidic Immunostaining System Enables Quality Assured and Standardized Immunohistochemical Biomarker Analysis. Sci Rep. 2017;7:45968.

64. Migliozzi D, Pelz B, Dupouy DG, Leblond AL, Soltermann A, Gijs MAM. Microfluidics-assisted multiplexed biomarker detection for in situ mapping of immune cells in tumor sections. Microsyst Nanoeng. 2019;5:1–12.

65. Dupouy DG, Ciftlik AT, Fiche M, Heintze D, Bisig B, de Leval L, et al. Continuous quantification of HER2 expression by microfluidic precision immunofluorescence estimates *HER2* gene amplification in breast cancer. Scientific Reports. 2016;6:20277.

66. Horowitz LF, Rodriguez AD, Ray T, Folch A. Microfluidics for interrogating live intact tissues. Microsyst Nanoeng. 2020;6:1–27.

67. A Method for Combining RNAscope In Situ Hybridization with Immunohistochemistry in Thick Free-Floating Brain Sections and Primary Neuronal Cultures | PLOS ONE [Internet]. [cited 2023 Apr 3]. Available from: https://journals.plos.org/plosone/article?id=10.1371/journal.pone.0120120

68. Ciftlik AT, Lehr HA, Gijs MAM. Microfluidic processor allows rapid HER2 immunohistochemistry of breast carcinomas and significantly reduces ambiguous (2+) read-outs. PNAS. 2013;110:5363–8.

69. PhenoCycler System | Akoya Biosciences [Internet]. 2021 [cited 2023 Apr 27]. Available from: https://www.akoyabio.com/phenocycler/

70. MACSima™ Imaging System | MACSima Imaging System | Ultra high content imaging | MACS Imaging and Microscopy | Products and services | Schweiz [Internet]. [cited 2023 Apr 27]. Available from: https://www.miltenyibiotec.com/CH-en/products/macsima-imaging-system.html

71. GeoMx DSP Overview [Internet]. NanoString. [cited 2023 Apr 27]. Available from: https://nanostring.com/products/geomx-digital-spatial-profiler/geomx-dsp-overview/

72. Hyperion Imaging System [Internet]. [cited 2023 Apr 27]. Available from: https://www.standardbio.com/products/instruments/hyperion

73. COMET™ | Easy Multiplex Immunofluorescence | Lunaphore [Internet]. Lunaphore Technologies - We build tumor analysis platforms performing immunohistochemistry using microfluidic technology. 2021 [cited 2023 Apr 27]. Available from: https://lunaphore.com/products/comet/

74. Cooksey GA, Sip CG, Folch A. A multi-purpose microfluidic perfusion system with combinatorial choice of inputs, mixtures, gradient patterns, and flow rates. Lab Chip. 2009;9:417–26.

75. Berthier E, Beebe DJ. Gradient generation platforms: new directions for an established microfluidic technology. Lab Chip. 2014;14:3241–7.

76. Jeon NL, Dertinger SKW, Chiu DT, Choi IS, Stroock AD, Whitesides GM. Generation of Solution and Surface Gradients Using Microfluidic Systems. Langmuir. 2000;16:8311–6.

77. Effects of flow and diffusion on chemotaxis studies in a microfabricated gradient generator - Lab on a Chip (RSC Publishing) [Internet]. [cited 2023 Apr 3]. Available from: https://pubs.rsc.org/en/content/articlelanding/2005/LC/b417245k#!divCitation

78. Chung BG, Flanagan LA, Rhee SW, Schwartz PH, Lee AP, Monuki ES, et al. Human neural stem cell growth and differentiation in a gradient-generating microfluidic device. Lab Chip. 2005;5:401–6.

79. Paliwal S, Iglesias PA, Campbell K, Hilioti Z, Groisman A, Levchenko A. MAPK-mediated bimodal gene expression and adaptive gradient sensing in yeast. Nature. 2007;446:46–51.

80. Dertinger SKW, Jiang X, Li Z, Murthy VN, Whitesides GM. Gradients of substrate-bound laminin orient axonal specification of neurons. Proceedings of the National Academy of Sciences. 2002;99:12542–7.

81. Toh AGG, Wang ZP, Yang C, Nguyen NT. Engineering microfluidic concentration gradient generators for biological applications. Microfluid Nanofluid. 2014;16:1–18.

82. Nguyen HT, Migliozzi D, Bisig B, de Leval L, Gijs MAM. High-content, cell-by-cell assessment of HER2 overexpression and amplification: a tool for intratumoral heterogeneity detection in breast cancer. Lab Invest. 2019;99:722–32.

83. Microfluidics-based immunofluorescence for fast staining of ALK in lung adenocarcinoma | Diagnostic Pathology | Full Text [Internet]. [cited 2023 Apr 3]. Available from: https://diagnosticpathology.biomedcentral.com/articles/10.1186/s13000-018-0757-1

84. Brajkovic S, Dupouy DG, de Leval L, Gijs MA. Microfluidics for rapid cytokeratin immunohistochemical staining in frozen sections. Laboratory Investigation. 2017;97:983–91.

85. A microfluidic platform towards automated multiplexed in situ sequencing | Scientific Reports [Internet]. [cited 2023 Apr 3]. Available from: https://www.nature.com/articles/s41598-019-40026-6

86. Ultra-fast and automated immunohistofluorescent multistaining using a microfluidic tissue processor | Scientific Reports [Internet]. [cited 2023 Apr 3]. Available from: https://www.nature.com/articles/s41598-019-41119-y

87. Rev. Mod. Phys. 77, 977 (2005) - Microfluidics: Fluid physics at the nanoliter scale [Internet]. [cited 2023 Apr 27]. Available from: https://journals.aps.org/rmp/abstract/10.1103/RevModPhys.77.977

88. Squires TM, Quake SR. Microfluidics: Fluid physics at the nanoliter scale. Rev Mod Phys. 2005;77:977–1026.

89. Neufeld Z, Haynes PH, Tél T. Chaotic mixing induced transitions in reaction–diffusion systems. Chaos: An Interdisciplinary Journal of Nonlinear Science. 2002;12:426–38.

90. Sigurdson M, Wang D, Meinhart CD. Electrothermal stirring for heterogeneous immunoassays. Lab Chip. 2005;5:1366–73.

91. Carvalho F, Marques MPC, Fernandes P. Sucrose Hydrolysis in a Bespoke Capillary Wall-Coated Microreactor. Catalysts. 2017;7:42.

92. Saltzman WM, Radomsky ML, Whaley KJ, Cone RA. Antibody diffusion in human cervical mucus. Biophysical Journal. 1994;66:508–15.

93. Lukacs GL, Haggie P, Seksek O, Lechardeur D, Freedman N, Verkman AS. Size-dependent DNA Mobility in Cytoplasm and Nucleus*. Journal of Biological Chemistry. 2000;275:1625–9.

94. Lee CY, Chang CL, Wang YN, Fu LM. Microfluidic Mixing: A Review. International Journal of Molecular Sciences. 2011;12:3263–87.

95. Suh YK, Kang S. A Review on Mixing in Microfluidics. Micromachines. 2010;1:82–111.

96. Capretto L, Cheng W, Hill M, Zhang X. Micromixing Within Microfluidic Devices. In: Lin B, editor. Microfluidics: Technologies and Applications [Internet]. Berlin, Heidelberg: Springer; 2011 [cited 2023 Apr 27]. p. 27–68. (Topics in Current Chemistry). Available from: https://doi.org/10.1007/128_2011_150

97. Ward K, Fan ZH. Mixing in microfluidic devices and enhancement methods. J Micromech Microeng. 2015;25:094001.

98. Soleymani A, Kolehmainen E, Turunen I. Numerical and experimental investigations of liquid mixing in T-type micromixers. Chemical Engineering Journal. 2008;135:S219–28.

99. Kamholz AE, Weigl BH, Finlayson BA, Yager P. Quantitative Analysis of Molecular Interaction in a Microfluidic Channel: The T-Sensor. Anal Chem. 1999;71:5340–7.

100. Ismagilov RF, Stroock AD, Kenis PJA, Whitesides G, Stone HA. Experimental and theoretical scaling laws for transverse diffusive broadening in two-phase laminar flows in microchannels. Applied Physics Letters. 2000;76:2376–8.

101. Cha J, Kim J, Ryu SK, Park J, Jeong Y, Park S, et al. A highly efficient 3D micromixer using soft PDMS bonding. J Micromech Microeng. 2006;16:1778.

102. Kim DS, Lee SH, Kwon TH, Ahn CH. A serpentine laminating micromixer combining splitting/recombination and advection. Lab Chip. 2005;5:739–47.

103. Schönfeld F, Hessel V, Hofmann C. An optimised split-and-recombine micro-mixer with uniform 'chaotic' mixing. Lab Chip. 2004;4:65–9.

104. Knight JB, Vishwanath A, Brody JP, Austin RH. Hydrodynamic Focusing on a Silicon Chip: Mixing Nanoliters in Microseconds. Phys Rev Lett. 1998;80:3863–6.

105. Pollack L, Tate MW, Darnton NC, Knight JB, Gruner SM, Eaton WA, et al. Compactness of the denatured state of a fast-folding protein measured by submillisecond small-angle x-ray scattering. Proceedings of the National Academy of Sciences. 1999;96:10115–7.

106. Kunstmann-Olsen C, Hoyland JD, Rubahn HG. Influence of geometry on hydrodynamic focusing and long-range fluid behavior in PDMS microfluidic chips. Microfluid Nanofluid. 2012;12:795–803.

107. Nguyen NT, Wu Z. Micromixers—a review. J Micromech Microeng. 2004;15:R1.

108. Stroock AD, Dertinger SKW, Ajdari A, Mezić I, Stone HA, Whitesides GM. Chaotic Mixer for Microchannels. Science. 2002;295:647–51.

109. Stroock AD, Dertinger SK, Whitesides GM, Ajdari A. Patterning Flows Using Grooved Surfaces. Anal Chem. 2002;74:5306–12.

110. Hayes MA, Polson NA, Phayre AN, Garcia AA. Flow-Based Microimmunoassay. Anal Chem. 2001;73:5896–902.

111. Microfluidics Based Magnetophoresis: A Review - Alnaimat - 2018 - The Chemical Record - Wiley Online Library [Internet]. [cited 2023 Apr 27]. Available from: https://onlinelibrary.wiley.com/doi/10.1002/tcr.201800018

112. Lee SH, Noort D van, Lee JY, Zhang BT, Park TH. Effective mixing in a microfluidic chip using magnetic particles. Lab Chip. 2009;9:479–82.

113. Manipulation of Self-Assembled Structures of Magnetic Beads for Microfluidic Mixing and Assaying | Analytical Chemistry [Internet]. [cited 2023 Apr 27]. Available from: https://pubs.acs.org/doi/10.1021/ac049415j

114. Enhanced Microfluidic Sample Homogeneity and Improved Antibody-Based Assay Kinetics Due to Magnetic Mixing | ACS Sensors [Internet]. [cited 2023 Apr 27]. Available from: https://pubs.acs.org/doi/full/10.1021/acssensors.1c00050

115. Scherer C, Figueiredo Neto AM. Ferrofluids: properties and applications. Braz J Phys. 2005;35:718–27.

116. Tsai TH, Liou DS, Kuo LS, Chen PH. Rapid mixing between ferro-nanofluid and water in a semi-active Y-type micromixer. Sensors and Actuators A: Physical. 2009;153:267–73.

117. Fu LM, Tsai CH, Leong KP, Wen CY. Rapid micromixer via ferrofluids. Physics Procedia. 2010;9:270–3.

118. Hejazian M, Nguyen NT. A Rapid Magnetofluidic Micromixer Using Diluted Ferrofluid. Micromachines. 2017;8:37.

119. Qiu T, Lee TC, Mark AG, Morozov KI, Münster R, Mierka O, et al. Swimming by reciprocal motion at low Reynolds number. Nat Commun. 2014;5:5119.

120. Hanasoge S, Hesketh PJ, Alexeev A. Microfluidic pumping using artificial magnetic cilia. Microsyst Nanoeng. 2018;4:1–9.

121. Chen CY, Chen CY, Lin CY, Hu YT. Magnetically actuated artificial cilia for optimum mixing performance in microfluidics. Lab Chip. 2013;13:2834–9.

122. Sahadevan V, Panigrahi B, Chen CY. Microfluidic Applications of Artificial Cilia: Recent Progress, Demonstration, and Future Perspectives. Micromachines. 2022;13:735.

123. Chen CY, Hsu CC, Mani K, Panigrahi B. Hydrodynamic influences of artificial cilia beating behaviors on micromixing. Chemical Engineering and Processing: Process Intensification. 2016;99:33–40.

124. Enhancement of microalgae growth using magnetic artificial cilia - Verburg - 2021 - Biotechnology and Bioengineering - Wiley Online Library [Internet]. [cited 2023 Apr 27]. Available from: https://onlinelibrary.wiley.com/doi/10.1002/bit.27756

125. Shanko ES, van de Burgt Y, Anderson PD, den Toonder JMJ. Microfluidic Magnetic Mixing at Low Reynolds Numbers and in Stagnant Fluids. Micromachines. 2019;10:731.

126. Putnam RW. Chapter 17 - Intracellular pH Regulation. In: Sperelakis N, editor. Cell Physiology Source Book (Fourth Edition) [Internet]. San Diego: Academic Press; 2012 [cited 2023 Apr 27]. p. 303–21. Available from: https://www.sciencedirect.com/science/article/pii/B9780123877383000172

127. Aleman J, Kilic T, Mille LS, Shin SR, Zhang YS. Microfluidic integration of regeneratable electrochemical affinity-based biosensors for continual monitoring of organ-on-a-chip devices. Nat Protoc. 2021;16:2564–93.

128. Gu S, Lu Y, Ding Y, Li L, Song H, Wang J, et al. A droplet-based microfluidic electrochemical sensor using platinum-black microelectrode and its application in high sensitive glucose sensing. Biosensors and Bioelectronics. 2014;55:106–12.

129. Keng PY, Chen S, Ding H, Sadeghi S, Shah GJ, Dooraghi A, et al. Micro-chemical synthesis of molecular probes on an electronic microfluidic device. Proceedings of the National Academy of Sciences. 2012;109:690–5.

130. Li HF, Lin JM. Applications of microfluidic systems in environmental analysis. Anal Bioanal Chem. 2009;393:555–67.

131. Ramos A, García-Sánchez P, Morgan H. AC electrokinetics of conducting microparticles: A review. Current Opinion in Colloid & Interface Science. 2016;24:79–90.

132. Ramos A, Morgan H, Green NG, Castellanos A. Ac electrokinetics: a review of forces in microelectrode structures. J Phys D: Appl Phys. 1998;31:2338–53.

133. Lu Y, Liu T, Lamanda AC, Sin MLY, Gau V, Liao JC, et al. AC Electrokinetics of Physiological Fluids for Biomedical Applications. J Lab Autom. 2015;20:611–20.

134. Green NG, Ramos A, González A, Morgan H, Castellanos A. Fluid flow induced by nonuniform ac electric fields in electrolytes on microelectrodes. I. Experimental measurements. Phys Rev E. 2000;61:4011–8.

135. Islam N, Wu J. Microfluidic transport by AC electroosmosis. J Phys: Conf Ser. 2006;34:356.

136. Green NG, Ramos A, González A, Morgan H, Castellanos A. Fluid flow induced by nonuniform ac electric fields in electrolytes on microelectrodes. III. Observation of streamlines and numerical simulation. Phys Rev E. 2002;66:026305.

137. García-Sánchez P, Ramos A. AC Electroosmosis: Basics and Lab-on-a-Chip Applications. In: Bhushan B, editor. Encyclopedia of Nanotechnology [Internet]. Dordrecht: Springer Netherlands; 2012 [cited 2023 Apr 27]. p. 25–30. Available from: https://doi.org/10.1007/978-90-481-9751-4_125

138. Ramos A, González A, Castellanos A, Green NG, Morgan H. Pumping of liquids with ac voltages applied to asymmetric pairs of microelectrodes. Phys Rev E. 2003;67:056302.

139. Bazant MZ, Ben Y. Theoretical prediction of fast 3D AC electro-osmotic pumps. Lab Chip. 2006;6:1455–61.

140. Huang CC, Z. Bazant M, Thorsen T. Ultrafast high-pressure AC electro-osmotic pumps for portable biomedical microfluidics. Lab on a Chip. 2010;10:80–5.

141. Cahill BP, Heyderman LJ, Gobrecht J, Stemmer A. Electro-osmotic streaming on application of traveling-wave electric fields. Phys Rev E. 2004;70:036305.

142. Ramos A, Morgan H, Green NG, González A, Castellanos A. Pumping of liquids with traveling-wave electroosmosis. Journal of Applied Physics. 2005;97:084906.

143. Wang SC, Chen HP, Lee CY, Yu CC, Chang HC. AC electro-osmotic mixing induced by non-contact external electrodes. Biosensors and Bioelectronics. 2006;22:563–7.

144. Modarres P, Tabrizian M. Phase-controlled field-effect micromixing using AC electroosmosis. Microsyst Nanoeng. 2020;6:1–11.

145. Cheng IF, Yang HL, Chung CC, Chang HC. A rapid electrochemical biosensor based on an AC electrokinetics enhanced immuno-reaction. Analyst. 2013;138:4656–62.

146. Wu CC, Yang DJ. A label-free impedimetric DNA sensing chip integrated with AC electroosmotic stirring. Biosensors and Bioelectronics. 2013;43:348–54.

147. Vafaie RH, Madanpasandi A, Vafaie RH, Madanpasandi A. In-situ AC electroosmotic and thermal perturbation effects for wide range of ionic strength. AIMSBPOA. 2017;4:451–64.

148. Koklu A, Tansel O, Oksuzoglu H, Sabuncu AC. Electrothermal flow on electrodes arrays at physiological conductivities. IET Nanobiotechnology. 2016;10:54–61.

149. Wong PK, Wang TH, Deval JH, Ho CM. Electrokinetics in micro devices for biotechnology applications. IEEE/ASME Transactions on Mechatronics. 2004;9:366–76.

150. Salari A, Thompson M. Recent advances in AC electrokinetic sample enrichment techniques for biosensor development. Sensors and Actuators B: Chemical. 2018;255:3601–15.

151. Park S, Zhang Y, Wang TH, Yang S. Continuous dielectrophoretic bacterial separation and concentration from physiological media of high conductivity. Lab Chip. 2011;11:2893–900.

152. Pethig R, Markx GH. Applications of dielectrophoresis in biotechnology. Trends in Biotechnology. 1997;15:426–32.

153. Zheng L, Brody JP, Burke PJ. Electronic manipulation of DNA, proteins, and nanoparticles for potential circuit assembly. Biosensors and Bioelectronics. 2004;20:606–19.

154. Clarke RW, White SS, Zhou D, Ying L, Klenerman D. Trapping of Proteins under Physiological Conditions in a Nanopipette. Angewandte Chemie. 2005;117:3813–6.

155. Wang XB, Yang J, Huang Y, Vykoukal J, Becker FF, Gascoyne PRC. Cell Separation by Dielectrophoretic Field-flow-fractionation. Anal Chem. 2000;72:832–9.

156. Washizu M, Suzuki S, Kurosawa O, Nishizaka T, Shinohara T. Molecular dielectrophoresis of biopolymers. IEEE Transactions on Industry Applications. 1994;30:835–43.

157. Kawabata T, Washizu M. Dielectrophoretic detection of molecular bindings. IEEE Transactions on Industry Applications. 2001;37:1625–33.

158. de la Rica R, Mendoza E, Lechuga LM, Matsui H. Label-Free Pathogen Detection with Sensor Chips Assembled from Peptide Nanotubes. Angewandte Chemie International Edition. 2008;47:9752–5.

159. Gong JR. Label-Free Attomolar Detection of Proteins Using Integrated Nanoelectronic and Electrokinetic Devices. Small. 2010;6:967–73.

160. Mittal N, Rosenthal A, Voldman J. nDEP microwells for single-cell patterning in physiological media. Lab Chip. 2007;7:1146–53.

161. Voldman J. Electrical Forces for Microscale Cell Manipulation. Annual Review of Biomedical Engineering. 2006;8:425–54.

162. Castellanos A, Ramos A, González A, Green NG, Morgan H. Electrohydrodynamics and dielectrophoresis in microsystems: scaling laws. J Phys D: Appl Phys. 2003;36:2584.

163. Sin MLY, Gau V, Liao JC, Wong PK. Electrothermal Fluid Manipulation of High-Conductivity Samples for Laboratory Automation Applications. JALA: Journal of the Association for Laboratory Automation. 2010;15:426–32.

164. Meinhart C, Wang D, Turner K. Measurement of AC Electrokinetic Flows. Biomedical Microdevices. 2003;5:139–45.

165. Ren Q, Meng F, Chan CL. Cell transport and suspension in high conductivity electrothermal flow with negative dielectrophoresis by immersed boundary-lattice Boltzmann method. International Journal of Heat and Mass Transfer. 2019;128:1229–44.

166. González A, Ramos A, Morgan H, Green NG, Castellanos A. Electrothermal flows generated by alternating and rotating electric fields in microsystems. Journal of Fluid Mechanics. 2006;564:415–33.

167. Liu X, Yang K, Wadhwa A, Eda S, Li S, Wu J. Development of an AC electrokinetics-based immunoassay system for on-site serodiagnosis of infectious diseases. Sensors and Actuators A: Physical. 2011;171:406–13.

168. Yu C, Kim GB, Clark PM, Zubkov L, Papazoglou ES, Noh M. A microfabricated quantum dot-linked immuno-diagnostic assay (μQLIDA) with an electrohydrodynamic mixing element. Sensors and Actuators B: Chemical. 2015;209:722–8.

169. Yang K, Islam N, Eda S, Wu J. Optimization of an AC electrokinetics immunoassay lab-chip for biomedical diagnostics. Microfluid Nanofluid. 2017;21:35.

170. Wu J, Lian M, Yang K. Micropumping of biofluids by alternating current electrothermal effects. Appl Phys Lett. 2007;90:234103.

171. Lian M, Wu J. Ultrafast micropumping by biased alternating current electrokinetics. Appl Phys Lett. 2009;94:064101.

172. Zhang R, Dalton C, Jullien GA. Two-phase AC electrothermal fluidic pumping in a coplanar asymmetric electrode array. Microfluid Nanofluid. 2011;10:521–9.

173. Frkonja-Kuczin A, Ray L, Zhao Z, Konopka MC, Boika A. Electrokinetic preconcentration and electrochemical detection of Escherichia coli at a microelectrode. Electrochimica Acta. 2018;280:191–6.

174. Lamanda A, Lu Y, Gill N, Wong PK. An electrokinetic microdevice for isolation and quantification of circulating cell-free DNA from physiological samples. In: 2015 Transducers - 2015 18th International Conference on Solid-State Sensors, Actuators and Microsystems (TRANSDUCERS). 2015. p. 544–7.

175. Sun H, Ren Y, Hou L, Tao Y, Liu W, Jiang T, et al. Continuous Particle Trapping, Switching, and Sorting Utilizing a Combination of Dielectrophoresis and Alternating Current Electrothermal Flow. Anal Chem. 2019;91:5729–38.

176. Friend J, Yeo LY. Microscale acoustofluidics: Microfluidics driven via acoustics and ultrasonics. Rev Mod Phys. 2011;83:647–704.

177. Kundt A. Ueber eine neue Art akustischer Staubfiguren und über die Anwendung derselben zur Bestimmung der Schallgeschwindigkeit in festen Körpern und Gasen. Annalen der Physik. 1866;203:497–523.

178. Dvořák V. Ueber die akustische Anziehung und Abstossung. Annalen der Physik. 1876;233:42–73.

179. Strutt JW. I. On the circulation of air observed in Kundt's tubes, and on some allied acoustical problems. Philosophical Transactions of the Royal Society of London. 1997;175:1–21.

180. Westervelt PJ. The Theory of Steady Rotational Flow Generated by a Sound Field. The Journal of the Acoustical Society of America. 2005;25:60–7.

181. Nyborg WL. Acoustic Streaming due to Attenuated Plane Waves. The Journal of the Acoustical Society of America. 2005;25:68–75.

182. Wu M, Ozcelik A, Rufo J, Wang Z, Fang R, Jun Huang T. Acoustofluidic separation of cells and particles. Microsyst Nanoeng. 2019;5:1–18.

183. Connacher W, Zhang N, Huang A, Mei J, Zhang S, Gopesh T, et al. Micro/nano acoustofluidics: materials, phenomena, design, devices, and applications. Lab on a Chip. 2018;18:1952–96.

184. Ding X, Li P, Lin SCS, Stratton ZS, Nama N, Guo F, et al. Surface acoustic wave microfluidics. Lab Chip. 2013;13:3626–49.

185. Leibacher I, Reichert P, Dual J. Microfluidic droplet handling by bulk acoustic wave (BAW) acoustophoresis. Lab Chip. 2015;15:2896–905.

186. Sarvazyan AP, Rudenko OV, Nyborg WL. Biomedical Applications of Radiation Force of Ultrasound: Historical Roots and Physical Basis. Ultrasound in Medicine & Biology. 2010;36:1379–94.

187. Nilsson A, Petersson F, Jönsson H, Laurell T. Acoustic control of suspended particles in micro fluidic chips. Lab Chip. 2004;4:131–5.

188. Lenshof A, Magnusson C, Laurell T. Acoustofluidics 8: Applications of acoustophoresis in continuous flow microsystems. Lab Chip. 2012;12:1210–23.

189. Shi J, Huang H, Stratton Z, Huang Y, Jun Huang T. Continuous particle separation in a microfluidic channel via standing surface acoustic waves (SSAW). Lab on a Chip. 2009;9:3354–9.

190. Wiklund M, Green R, Ohlin M. Acoustofluidics 14: Applications of acoustic streaming in microfluidic devices. Lab Chip. 2012;12:2438–51.

191. Chen Z, Shen L, Zhao X, Chen H, Xiao Y, Zhang Y, et al. Acoustofluidic micromixers: From rational design to lab-on-a-chip applications. Applied Materials Today. 2022;26:101356.

192. Huang PH, Nama N, Mao Z, Li P, Rufo J, Chen Y, et al. A reliable and programmable acoustofluidic pump powered by oscillating sharp-edge structures. Lab Chip. 2014;14:4319–23.

193. Heron SR, Wilson R, Shaffer SA, Goodlett DR, Cooper JM. Surface Acoustic Wave Nebulization of Peptides As a Microfluidic Interface for Mass Spectrometry. Anal Chem. 2010;82:3985–9.

194. Ahmed D, Ozcelik A, Bojanala N, Nama N, Upadhyay A, Chen Y, et al. Rotational manipulation of single cells and organisms using acoustic waves. Nat Commun. 2016;7:11085.

195. Taller D, Richards K, Slouka Z, Senapati S, Hill R, Go DB, et al. On-chip surface acoustic wave lysis and ion-exchange nanomembrane detection of exosomal RNA for pancreatic cancer study and diagnosis. Lab Chip. 2015;15:1656–66.

196. Huang PH, Xie Y, Ahmed D, Rufo J, Nama N, Chen Y, et al. An acoustofluidic micromixer based on oscillating sidewall sharp-edges. Lab Chip. 2013;13:3847–52.

197. Zhang C, Guo X, Brunet P, Costalonga M, Royon L. Acoustic streaming near a sharp structure and its mixing performance characterization. Microfluid Nanofluid. 2019;23:104.

198. Li X, Huffman J, Ranganathan N, He Z, Li P. Acoustofluidic enzyme-linked immunosorbent assay (ELISA) platform enabled by coupled acoustic streaming. Analytica Chimica Acta. 2019;1079:129–38.

199. Tho P, Manasseh R, Ooi A. Cavitation microstreaming patterns in single and multiple bubble systems. Journal of Fluid Mechanics. 2007;576:191–233.

200. Liu RH, Yang J, Pindera MZ, Athavale M, Grodzinski P. Bubble-induced acoustic micromixing. Lab Chip. 2002;2:151–7.

201. Liu RH, Lenigk R, Druyor-Sanchez RL, Yang J, Grodzinski P. Hybridization Enhancement Using Cavitation Microstreaming. Anal Chem. 2003;75:1911–7.

202. Chen H, Gao Y, Petkovic K, Yan S, Best M, Du Y, et al. Reproducible bubble-induced acoustic microstreaming for bead disaggregation and immunoassay in microfluidics. Microfluid Nanofluid. 2017;21:30.

203. Shilton RJ, Yeo LY, Friend JR. Quantification of surface acoustic wave induced chaotic mixing-flows in microfluidic wells. Sensors and Actuators B: Chemical. 2011;160:1565–72.

204. Bourquin Y, Reboud J, Wilson R, Zhang Y, Cooper JM. Integrated immunoassay using tuneable surface acoustic waves and lensfree detection. Lab Chip. 2011;11:2725–30.

205. Galopin E, Beaugeois M, Pinchemel B, Camart JC, Bouazaoui M, Thomy V. SPR biosensing coupled to a digital microfluidic microstreaming system. Biosensors and Bioelectronics. 2007;23:746–50.

206. Renaudin A, Chabot V, Grondin E, Aimez V, Charette PG. Integrated active mixing and biosensing using surface acoustic waves (SAW) and surface plasmon resonance (SPR) on a common substrate. Lab Chip. 2010;10:111–5.

207. Cular S, Branch DW, Bhethanabotla VR, Meyer GD, Craighead HG. Removal of Nonspecifically Bound Proteins on Microarrays Using Surface Acoustic Waves. IEEE Sensors Journal. 2008;8:314–20.

208. Meyer GD, Moran-Mirabal JM, Branch DW, Craighead HG. Nonspecific binding removal from protein microarrays using thickness shear mode resonators. IEEE Sensors Journal. 2006;6:254–61.

209. Sankaranarayanan SKRS, Singh R, Bhethanabotla VR. Acoustic streaming induced elimination of nonspecifically bound proteins from a surface acoustic wave biosensor: Mechanism prediction using fluid-structure interaction models. Journal of Applied Physics. 2010;108:104507.

210. Sankaranarayanan SKRS, Cular S, Bhethanabotla VR, Joseph B. Flow induced by acoustic streaming on surface-acoustic-wave devices and its application in biofouling removal: A computational study and comparisons to experiment. Phys Rev E. 2008;77:066308.

211. Petkovic-Duran K, Manasseh R, Zhu Y, Ooi A. Chaotic micromixing in open wells using audio-frequency acoustic microstreaming. BioTechniques. 2009;47:827–34.

212. Gao Y, Tran P, Petkovic-Duran K, Swallow T, Zhu Y. Acoustic micromixing increases antibody-antigen binding in immunoassays. Biomed Microdevices. 2015;17:79.

213. soniccatch [Internet]. website soniccatch & sonicwipe by usePAT. [cited 2023 Apr 27]. Available from: http://www.usepat.com/products/soniccatch/

214. AcouSort »Automated sample preparation - More reliable results by AcouSort [Internet]. 2023 [cited 2023 Apr 27]. Available from: https://acousort.com/

215. Acoustic Focusing Cytometry Technology Overview - CH [Internet]. [cited 2023 Apr 27]. Available from: https://www.thermofisher.com/uk/en/home/life-science/cell-analysis/flow-cytometry/flow-cytometers/acoustic-focusing-technology-overview.html

216. Rivet C, Lee H, Hirsch A, Hamilton S, Lu H. Microfluidics for medical diagnostics and biosensors. Chemical Engineering Science. 2011;66:1490–507.

217. Liu Y, Jiang X. Why microfluidics? Merits and trends in chemical synthesis. Lab Chip. 2017;17:3960–78.

218. Junkin M, Tay S. Microfluidic single-cell analysis for systems immunology. Lab Chip. 2014;14:1246–60.

219. Yin H, Marshall D. Microfluidics for single cell analysis. Current Opinion in Biotechnology. 2012;23:110–9.

220. Shembekar N, Chaipan C, Utharala R, Merten CA. Droplet-based microfluidics in drug discovery, transcriptomics and high-throughput molecular genetics. Lab Chip. 2016;16:1314–31.

221. Eduati F, Utharala R, Madhavan D, Neumann UP, Longerich T, Cramer T, et al. A microfluidics platform for combinatorial drug screening on cancer biopsies. Nat Commun. 2018;9:2434.

222. Nguyen HT, Trouillon R, Matsuoka S, Fiche M, Leval L de, Bisig B, et al. Microfluidics-assisted fluorescence in situ hybridization for advantageous human epidermal growth factor receptor 2 assessment in breast cancer. Lab Invest. 2017;97:93–103.

223. Han D, Park JK. Optoelectrofluidic enhanced immunoreaction based on optically-induced dynamic AC electroosmosis. Lab Chip. 2016;16:1189–96.

224. Yang CK, Chang JS, Chao SD, Wu KC. Effects of diffusion boundary layer on reaction kinetics of immunoassay in a biosensor. Journal of Applied Physics. 2008;103:084702.

225. Nguyen HT, Dupont LN, Cuttaz EA, Jean AM, Trouillon R, Gijs MAM. Breast cancer HER2 analysis by extra-short incubation microfluidics-assisted fluorescence in situ hybridization (ESIMA FISH). Microelectronic Engineering. 2018;189:33–8.

226. Kim MS, Kim T, Kong SY, Kwon S, Bae CY, Choi J, et al. Breast Cancer Diagnosis Using a Microfluidic Multiplexed Immunohistochemistry Platform. PLOS ONE. 2010;5:e10441.

227. Kim MS, Kwon S, Kim T, Lee ES, Park JK. Quantitative proteomic profiling of breast cancers using a multiplexed microfluidic platform for immunohistochemistry and immunocytochemistry. Biomaterials. 2011;32:1396–403.

228. Varga Z, Noske A, Ramach C, Padberg B, Moch H. Assessment of HER2 status in breast cancer: overall positivity rate and accuracy by fluorescence in situ hybridization and immunohistochemistry in a single institution over 12 years: a quality control study. BMC Cancer. 2013;13:615.

229. Moctar AOE, Aubry N, Batton J. Electro-hydrodynamic micro-fluidic mixer. Lab Chip. 2003;3:273–80.

230. Oddy MH, Santiago JG, Mikkelsen JC. Electrokinetic Instability Micromixing. Anal Chem. 2001;73:5822–32.

231. Chang M, Gabayno JLF, Ye R, Huang KW, Chang YJ. Mixing efficiency enhancing in micromixer by controlled magnetic stirring of Fe3O4 nanomaterial. Microsyst Technol. 2017;23:457–63.

232. Phan HV, Coşkun MB, Şeşen M, Pandraud G, Neild A, Alan T. Vibrating membrane with discontinuities for rapid and efficient microfluidic mixing. Lab Chip. 2015;15:4206–16.

233. Ozcelik A, Ahmed D, Xie Y, Nama N, Qu Z, Nawaz AA, et al. An Acoustofluidic Micromixer via Bubble Inception and Cavitation from Microchannel Sidewalls. Anal Chem. 2014;86:5083–8.

234. Xia Q, Zhong S. Liquid mixing enhanced by pulse width modulation in a Y-shaped jet configuration. Fluid Dyn Res. 2013;45:025504.

235. Green NG, Ramos A, González A, Castellanos A, Morgan H. Electric field induced fluid flow on microelectrodes: the effect of illumination. J Phys D: Appl Phys. 1999;33:L13–7.

236. Feldman HC, Sigurdson M, Meinhart CD. AC electrothermal enhancement of heterogeneous assays in microfluidics. Lab Chip. 2007;7:1553–9.

237. Numerical Study of Particle-Fluid Flow Under AC Electrokinetics in Electrode-Multilayered Microfluidic Device | IEEE Journals & Magazine | IEEE Xplore [Internet]. [cited 2022 Jun 14]. Available from: https://ieeexplore.ieee.org/document/8388274

238. Velasco V, Williams SJ. Electrokinetic concentration, patterning, and sorting of colloids with thin film heaters. Journal of Colloid and Interface Science. 2013;394:598–603.

239. Mishra A, Khor JW, Clayton KN, Williams SJ, Pan X, Kinzer-Ursem T, et al. Optoelectric patterning: Effect of electrode material and thickness on laser-induced AC electrothermal flow. ELECTROPHORESIS. 2016;37:658–65.

240. Ng WY, Goh S, Lam YC, Yang C, Rodríguez I. DC-biased AC-electroosmotic and AC-electrothermal flow mixing in microchannels. Lab Chip. 2009;9:802–9.

241. Güven E, Duus K, Lydolph MC, Jørgensen CS, Laursen I, Houen G. Non-specific binding in solid phase immunoassays for autoantibodies correlates with inflammation markers. Journal of Immunological Methods. 2014;403:26–36.

242. Wang J, Yiu B, Obermeyer J, Filipe CDM, Brennan JD, Pelton R. Effects of Temperature and Relative Humidity on the Stability of Paper-Immobilized Antibodies. Biomacromolecules. 2012;13:559–64.

243. Liu T. Electrokinetic Real-Time Polymerase Chain Reaction Toward Point-Of-Care Diagnosis. 2015 [cited 2022 Nov 9]; Available from: https://repository.arizona.edu/handle/10150/579083

244. Lee S, Kim J, Wereley ST, Kwon JS. Light-actuated electrothermal microfluidic flow for micro-mixing. J Micromech Microeng. 2018;29:017003.

245. Yuan Q, Yang K, Wu J. Optimization of planar interdigitated microelectrode array for biofluid transport by AC electrothermal effect. Microfluid Nanofluid. 2014;16:167–78.

246. Gao J, Sin MLY, Liu T, Gau V, Liao JC, Wong PK. Hybrid electrokinetic manipulation in high-conductivity media. Lab Chip. 2011;11:1770–5.

247. Ng WY, Ramos A, Lam YC, Wijaya IPM, Rodriguez I. DC-biased AC-electrokinetics: a conductivity gradient driven fluid flow. Lab Chip. 2011;11:4241–7.

248. Liu W, Ren Y, Tao Y, Chen X, Wu Q. Electrode Cooling Effect on Out-Of-Phase Electrothermal Streaming in Rotating Electric Fields. Micromachines. 2017;8:327.

249. Green NG, Ramos A, González A, Castellanos A, Morgan H. Electrothermally induced fluid flow on microelectrodes. Journal of Electrostatics. 2001;53:71–87.

250. Loire S, Kauffmann P, Mezić I, Meinhart CD. A theoretical and experimental study of ac electrothermal flows. J Phys D: Appl Phys. 2012;45:185301.

251. Langmuir I. THE ADSORPTION OF GASES ON PLANE SURFACES OF GLASS, MICA AND PLATINUM. J Am Chem Soc. 1918;40:1361–403.

252. Huang KR, Chang JS. Three dimensional simulation on binding efficiency of immunoassay for a biosensor with applying electrothermal effect. Heat Mass Transfer. 2013;49:1647–58.

253. Yang CK, Chang JS, Chao SD, Wu KC. Two dimensional simulation on immunoassay for a biosensor with applying electrothermal effect. Appl Phys Lett. 2007;91:113904.

254. Berthier J, Silberzan P. Microfluidics for Biotechnology, Second Edition [Internet]. [cited 2022 Jun 15]. Available from: https://ieeexplore.ieee.org/document/9100092

255. Islam MA. Einstein–Smoluchowski Diffusion Equation: A Discussion. Phys Scr. 2004;70:120–5.

256. Hong FJ, Cao J, Cheng P. A parametric study of AC electrothermal flow in microchannels with asymmetrical interdigitated electrodes. International Communications in Heat and Mass Transfer. 2011;38:275–9.

257. Ouyang M, Mohan R, Lu Y, Liu T, Mach KE, Sin MLY, et al. An AC electrokinetics facilitated biosensor cassette for rapid pathogen identification. Analyst. 2013;138:3660–6.

258. Cui H, Li S, Yuan Q, Wadhwa A, Eda S, Chambers M, et al. An AC electrokinetic impedance immunosensor for rapid detection of tuberculosis. Analyst. 2013;138:7188–96.

259. Yuan Q, Wu J. Thermally biased AC electrokinetic pumping effect for Lab-on-a-chip based delivery of biofluids. Biomed Microdevices. 2013;15:125–33.

260. Lian M, Islam N, Wu J. AC electrothermal manipulation of conductive fluids and particles for lab-chip applications. IET Nanobiotechnology. 2007;1:36–43.

261. Migliozzi D, Pelz B, Dupouy DG, Leblond AL, Soltermann A, Gijs MAM. Microfluidics-assisted multiplexed biomarker detection for in situ mapping of immune cells in tumor sections. Microsyst Nanoeng. 2019;5:1–12.

262. Ciftlik AT, Lehr HA, Gijs MAM. Microfluidic processor allows rapid HER2 immunohistochemistry of breast carcinomas and significantly reduces ambiguous (2+) read-outs. PNAS. 2013;110:5363–8.

263. Alturkistani HA, Tashkandi FM, Mohammedsaleh ZM. Histological Stains: A Literature Review and Case Study. Glob J Health Sci. 2016;8:72–9.

264. Ultrafast tissue staining with chemical tags | PNAS [Internet]. [cited 2023 Apr 3]. Available from: https://www.pnas.org/doi/10.1073/pnas.1411087111

265. Nguyen HT, Migliozzi D, Bisig B, de Leval L, Gijs MAM. High-content, cell-by-cell assessment of HER2 overexpression and amplification: a tool for intratumoral heterogeneity detection in breast cancer. Lab Invest. 2019;99:722–32.

266. Silverio V, Guha S, Keiser A, Natu R, Reyes DR, van Heeren H, et al. Overcoming technological barriers in microfluidics: Leakage testing. Frontiers in Bioengineering and Biotechnology [Internet]. 2022 [cited 2023 Apr 3];10. Available from: https://www.frontiersin.org/articles/10.3389/fbioe.2022.958582

267. Ogden S, Bodén R, Hjort K. A Latchable Valve for High-Pressure Microfluidics. Journal of Microelectromechanical Systems. 2010;19:396–401.

268. Naskar S, Kumaran V, Basu B. Reprogramming the Stem Cell Behavior by Shear Stress and Electric Field Stimulation: Lab-on-a-Chip Based Biomicrofluidics in Regenerative Medicine. Regen Eng Transl Med. 2019;5:99–127.

269. Sidhaye VK, Schweitzer KS, Caterina MJ, Shimoda L, King LS. Shear stress regulates aquaporin-5 and airway epithelial barrier function. Proc Natl Acad Sci U S A. 2008;105:3345–50.

270. Liu B, Zhao J, Qian J. Numerical analysis of cavitation erosion and particle erosion in butterfly valve. Engineering Failure Analysis. 2017;80:312–24.

271. Liu X, Wu Z, Li B, Zhao J, He J, Li W, et al. Influence of inlet pressure on cavitation characteristics in regulating valve. Engineering Applications of Computational Fluid Mechanics. 2020;14:299–310.

272. Katoh K. Rapid fixation and immunofluorescent staining of cultured cells using microwave irradiation. Journal of Histotechnology. 2011;34:29–34.

273. Sigurdson M, Wang D, Meinhart CD. Electrothermal stirring for heterogeneous immunoassays. Lab Chip. 2005;5:1366–73.

274. Saltzman WM, Radomsky ML, Whaley KJ, Cone RA. Antibody diffusion in human cervical mucus. Biophysical Journal. 1994;66:508–15.

275. Lukacs GL, Haggie P, Seksek O, Lechardeur D, Freedman N, Verkman AS. Size-dependent DNA Mobility in Cytoplasm and Nucleus*. Journal of Biological Chemistry. 2000;275:1625–9.

276. Magaki S, Hojat SA, Wei B, So A, Yong WH. An Introduction to the Performance of Immunohistochemistry. In: Yong WH, editor. Biobanking: Methods and Protocols [Internet]. New York, NY: Springer; 2019 [cited 2023 Apr 3]. p. 289–98. (Methods in Molecular Biology). Available from: https://doi.org/10.1007/978-1-4939-8935-5_25

277. Hoffman GE, Murphy KJ, Sita LV. The Importance of Titrating Antibodies for Immunocytochemical Methods. Current Protocols in Neuroscience. 2016;76:2.12.1-2.12.37.

278. Phan HV, Coşkun MB, Şeşen M, Pandraud G, Neild A, Alan T. Vibrating membrane with discontinuities for rapid and efficient microfluidic mixing. Lab Chip. 2015;15:4206–16.

279. Bachman H, Chen C, Rufo J, Zhao S, Yang S, Tian Z, et al. An acoustofluidic device for efficient mixing over a wide range of flow rates. Lab Chip. 2020;20:1238–48.

280. Ozcelik A, Ahmed D, Xie Y, Nama N, Qu Z, Nawaz AA, et al. An Acoustofluidic Micromixer via Bubble Inception and Cavitation from Microchannel Sidewalls. Anal Chem. 2014;86:5083–8.

281. Lee CY, Chang CL, Wang YN, Fu LM. Microfluidic Mixing: A Review. International Journal of Molecular Sciences. 2011;12:3263–87.

282. Ng WY, Goh S, Lam YC, Yang C, Rodríguez I. DC-biased AC-electroosmotic and AC-electrothermal flow mixing in microchannels. Lab Chip. 2009;9:802–9.

283. Sin MLY, Gau V, Liao JC, Wong PK. Electrothermal Fluid Manipulation of High-Conductivity Samples for Laboratory Automation Applications. JALA: Journal of the Association for Laboratory Automation. 2010;15:426–32.

284. Waks AG, Winer EP. Breast Cancer Treatment: A Review. JAMA. 2019;321:288–300.

285. Shao MM, Chan SK, Yu AMC, Lam CCF, Tsang JYS, Lui PCW, et al. Keratin expression in breast cancers. Virchows Arch. 2012;461:313–22.

286. Langmuir I. THE ADSORPTION OF GASES ON PLANE SURFACES OF GLASS, MICA AND PLATINUM. J Am Chem Soc. 1918;40:1361–403.

287. Parnell WJ, De Pascalis R. Soft metamaterials with dynamic viscoelastic functionality tuned by pre-deformation. Philosophical Transactions of the Royal Society A: Mathematical, Physical and Engineering Sciences. 2019;377:20180072.

288. Tensional acoustomechanical soft metamaterials | Scientific Reports [Internet]. [cited 2023 Apr 3]. Available from: https://www.nature.com/articles/srep27432

289. Dual J, Schwarz T. Acoustofluidics 3: Continuum mechanics for ultrasonic particle manipulation. Lab Chip. 2011;12:244–52.

290. Aghakhani A, Cetin H, Erkoc P, Tombak GI, Sitti M. Flexural wave-based soft attractor walls for trapping microparticles and cells. Lab Chip. 2021;21:582–96.

291. Muller PB, Barnkob R, Jensen MJH, Bruus H. A numerical study of microparticle acoustophoresis driven by acoustic radiation forces and streaming-induced drag forces. Lab Chip. 2012;12:4617–27.

292. Lighthill SJ. Acoustic streaming. Journal of Sound and Vibration. 1978;61:391–418.

293. Wu J. Acoustic Streaming and Its Applications. Fluids. 2018;3:108.

294. Shahzad K, Aeken WV, Mottaghi M, Kamyab VK, Kuhn S. Aggregation and clogging phenomena of rigid microparticles in microfluidics. Microfluid Nanofluid. 2018;22:104.

295. Nyborg WL. Acoustic Streaming near a Boundary. The Journal of the Acoustical Society of America. 1958;30:329–39.

296. Deng S, Jia K, Wu E, Hu X, Fan Z, Yang K. Controllable Micro-Particle Rotation and Transportation Using Sound Field Synthesis Technique. Applied Sciences. 2018;8:73.

297. Lamprecht A, Schwarz T, Wang J, Dual J. Viscous torque on spherical micro particles in two orthogonal acoustic standing wave fields. The Journal of the Acoustical Society of America. 2015;138:23–32.

298. Bach JS, Bruus H. Theory of pressure acoustics with viscous boundary layers and streaming in curved elastic cavities. The Journal of the Acoustical Society of America. 2018;144:766–84.

299. Barnkob R, Augustsson P, Laurell T, Bruus H. Acoustic radiation- and streaming-induced microparticle velocities determined by microparticle image velocimetry in an ultrasound symmetry plane. Phys Rev E. 2012;86:056307.

300. Hudis CA. Trastuzumab — Mechanism of Action and Use in Clinical Practice. New England Journal of Medicine. 2007;357:39–51.

301. Barak V, Goike H, Panaretakis KW, Einarsson R. Clinical utility of cytokeratins as tumor markers. Clinical Biochemistry. 2004;37:529–40.

302. Dong X, Liu L, Tu Y, Zhang J, Miao G, Zhang L, et al. Rapid PCR powered by microfluidics: A quick review under the background of COVID-19 pandemic. TrAC Trends in Analytical Chemistry. 2021;143:116377.

303. Polymerase chain reaction in microfluidic devices - Lab on a Chip (RSC Publishing) [Internet]. [cited 2023 Apr 27]. Available from: https://pubs.rsc.org/en/content/articlelanding/2016/lc/c6lc00984k

Muaz Salama Draz

Address: Lausanne, Switzerland **LinkedIn**: linkedin.com/in/muaz-draz
Phone: +41-787584888 **E-Mail**: m.salamadraz@gmail.com

Education

Ph.D. in Microsystems and Microelectronics (industrial Ph.D.), School of Engineering

- Ecole Polytechnique Federale de Lausanne (EPFL), Switzerland, Nov 2018 – June 2023

Erasmus Mundus Master of Science in Nanoscience and Nanotechnology, Nano Biophysics Track

- TU Dresden, Germany, 2016/17 • Grade: **Magna Cum Laude,** Great Distinction
- KU Leuven, Belgium, 2015/16

Bachelor of Science in Biomedical Engineering, (**2007-2012)**, Higher Technological Institute (HTI), Egypt

- GPA: 3.62/4.0 • Grade: **Distinction** with **Honor** Degree • Rank: 5th

Awards & Honors

- European Union's Horizon 2020 research and innovation fellowship - Marie Skłodowska-Curie grant for industrial innovative technologies and entrepreneurship training, Nov 2018-Jan 2023.
- Erasmus Mundus M.Sc. in Nanoscience and Nanotechnology tuition waiver Scholarship, 2015/16/17.
- Misr El-Kheir Foundation (MEK) supplemental scholarship 2015/16.
- HTI Excellent student's partial tuition waiver scholarship for three consecutive years 2010/11/12.
- Dean's honoring list for excellent students for three consecutive years 2010/11/12, HTI, Egypt.
- Egyptian champion (3rd) ranking in National Fencing Sport Championship held in Olympic Center, 2005/06.
- Champion (1st) ranking in Championship of Education in Gharbia Governorate, Egypt, 2001.

Professional Experience

PhD researcher, Lab of microsystems 2-EPFL and Lunaphore Technologies SA, Switzerland, (2018 – 2023)

- **Topic** "Development of next-generation microfluidic systems for enhanced, faster and cost-effective immunoassays for tissue diagnostics - Ac electro-kinetics & Acousto-fluidics"
- Clean room microfabrication: Surface treatment and measurements, photolithography (mask & mask-less), sputtering and lift-off techniques, etching, microfluidic fabrication, laser cutting and milling, and 3D printing.
- Bio-assay: Optimization of tissue diagnostic immunoassays (proteomics and transcriptomics)
    - Tissue and cell pellets diagnostics (FFPE & Frozen): Multiplex fluorescence immunohistochemistry and fluorescence in situ hybridization (FISH), multi-color fluorescence microscopy and bright field imaging, and image processing and analysis.
    - Immunoassays optimization: Antigen retrieval, blocking methods, auto-fluorescence quenching, assay buffers, and elution.
    - Amplification techniques: Tyramide signal (TSA) and streptavidin/biotin amplification, and indirect assays.
    - Glass surface-based assays: Surface preparation and functionalization for tissue mounting, and surface assays (streptavidin/avidin-biotin fluorescence assays)
- Finite element analysis (COMSOL): Modeling and optimization of microfluidic systems - AC electrokinetic and acousto-fluidic approaches to enhance the microfluidic immunoassay performance.
    - Strong experience working with Electrostatics, fluid flow mechanics, heat transfer in solids and fluids, transport of chemical species, and surface-based reactions.
    - Good experience with solid mechanics, pressure, and thermoviscous acoustics.
    - Multiphysics couplings of fluid-particle and fluid-solid interaction, non-isothermal flow, acoustic-thermoviscous, acoustic streaming, piezoelectric effect, and acoustic-structure interaction.
- Coordination with assay development scientists, R&D engineers, IP experts, and hardware and software teams.

Research scientist, Fraunhofer Institute for Ceramic Technologies and Systems IKTS, Department of Bio- and Nanotechnology, Dresden, (Nov 2017 – Oct 2018)

- Development of the ceramic-based electrochemical biosensing platform from my master's thesis.
- Designing and integrating a microfluidic structure, all-in-one microelectrode LTCC chip for a future step of having a ceramic electrochemical multi-sensor array.
- Investigating the integration of polymer (PET, PEEK) substrates with Pt electrodes for flexible electronics and biosensing using the key learnings and results obtained with LTCC chips.

Master thesis, Fraunhofer Institute for Ceramic Technologies and Systems IKTS, Department of Bio- and Nanotechnology, Dresden, Germany (March –Sep 2017)

- **Topic** "Aptamer-based Electrochemical Bio-sensing using LTCC chips with screen printed gold electrodes"
- Investigate the usage of low-temperature co-fired ceramic (LTCC) chips with Au electrodes for electrochemical biosensing, and assay development, and surface treatment and functionalization.
- In parallel to using Au-coated SiO_2 chips as pure gold for reference measurements and SPR as an optical reference measurement for sensor development, functionalization, detection, and regeneration.

Research Assistant, Max Bergmann Center of Biomaterials, BioNanoSensorics group, Dresden, Germany, (Nov 2016 – Jan 2017)

- **Topic**: "Fluid-Integrated Silicon Nanowire based Memristive Biosensors – Ebola virus"
- Investigate the voltage gap opening between current minima reached in forward and backward loops of the I_{ds}–V_{ds} due to different gate voltages, dry/liquid conditions, and scan rates, using an electrical probe station.

Research assistant, IMEC, Leuven, Belgium, (Feb – May) 2016

- **Topic**: "Single Cancer Cell Characterization using High-Density Microelectrode Array"
- Investigating differences in the impedance spectra of IMEC-CMOS microelectrode array chip using equivalent circuit (ZVIEW software) and statistically process these results to gain insights about the biology of different cancer cell lines.

Product Specialist, EG Medical Systems - Karl Storz for Medical Optics-Neurosurgery, Egypt, (Jan - April 2015).

Technical Support Engineer, AL-Galaa Hospital, Cairo, Egypt, (Sep 2013 - Sep 2014).

Maintenance team leader, Biotechnology for Medical Engineering CO., Neuro-Electrophysiology, (2012-13)

Publications, Patents, & Conferences

- **Publication: Draz, M. S**.., Dupouy, D., & Gijs, M. (2023). Acoustofluidic large-scale mixing for enhanced microfluidic immunostaining for tissue diagnostics. Lab on a Chip. https://doi.org/10.1039/D3LC00312D.
- **Patent**: **Draz, M. S**.., Dupouy, D., & Gijs, Invention on acoustic-microfluidic tissue processing systems for enhanced spatial proteomics and transcriptomics. EU patent-EP23176247.7, filled May 2023, Patent pending.
- **Publication: Draz, M. S**., Uning, K., Dupouy, D., & Gijs, M. (2023). Efficient AC electrothermal flow (ACET) on-chip for enhanced immunoassays. Lab on a Chip. https://doi.org/10.1039/D2LC01147F.
- **Patent**: **Draz, M. S**., Dupouy, D., & Gijs, M., Nov 2022, Invention on microfluidic cartridge for biological sample processing**,** EU patent EP22207056, filled Nov 2022, EPFL & Lunaphore, Patent pending.
- **Poster** and **talk**: **Muaz Draz** and Dupouy, D., & Gijs, M., Electrothermal effects for enhancing surface-based assays, NanoBioTech conference, Montreux, Switzerland, Nov 2021.
- **Poster**: **Muaz Draz** and Martin Gijs, Microfluidic technologies for automated tissue diagnostics EPFL Center for Cancer Science and Engineering retreat, ECCSE Retreat-Agora, Lausanne, Switzerland, Feb 2020.
- **Poster**: **Muaz Draz**, N. Dennison, S. Ziesche, U. Partsch, U. Gierth, M. Schneider, J. Opitz, L. Römhildt, Ceramic-based chips for Bio-analytics, NanoBioSensor Conference, Sep 2017, Dresden, Germany.

Internships & Training

Research Assistant–Internship, Life Science Technology department, IMEC, Leuven, Belgium, (July - Sep 2016)

- **Topic** "Acoustic-neuron interaction study in a simple animal model"
- Development of a mathematical model for designing a 3D lens that can generate a focal point at a specific distance, to be developed as a multi-focal lens with different focal points.
- Modeling of the lens using COMSOL Multiphysics followed by 3D fabrication and testing in aqueous mediums.

Clean Room Training, CHALMERS University of Technology, SWEDEN, (19 - 21 April 2016)

- Deposition techniques (Sputtering/Evaporation), Optical Lithography, Dry and wet etching, SEM, and CVD.

Summer Training, HTI Training Center, Cairo, Egypt, (May - July 2012)

- Advanced training on the following medical devices (X-ray-Philips, Ultrasound-Siemens, EEG-Compumedics)

Summer Training, HTI Training Center, Cairo, Egypt, (May - July 2011)

- Technical training and troubleshooting of (Trumpf Endoscopes, Hamilton Ventilators, and Fresenius Hemodialysis systems) and software course: C++

Bioelectronics and Biosensors Training, Biomedical & Scientific Training Center, Egypt, (June - July 2010)

- Technical training and troubleshooting of (Microscopes, Hot air oven, Centrifuge, Lab incubator)

Hospital planning and organization training, Al Salam International Hospital, Egypt, (May - July 2009)

- Hospital design and planning, safety precautions, and risk management.

Extracurricular Activities

Ph.D. student representative, EDMI school, EPFL, (Jan 2021- Jan 2023)

- Participating in program regulations, study and exams planning, course credits, and student health and well-being assessments.
- Acting as a liaison person between EDMI students and committee members for any requests.

Teaching assistant for Microfabrication course (clean room on photolithography, coatings, development, and wet etching and surface measurements), and Design of experiments course (1 semester): introduction to statistical-based planning and analysis of experiments with JMP software.

Supervision of master and bachelor students' projects, EPFL, (2018-2022)

Peer-Education Trainer for Sexual & Reproductive Health and HIV/AIDS prevention, United Nations Population Fund - Y-PEER, (2011-2017)

Member of (Egyptian Food Bank, Egyptian Cure Bank, and Life Makers) NGOs.

Player in the UNIL-EPFL center for professional fencing team (2019), KU Leuven professional fencing team (2015/16), and Egyptian national fencing team (2000/2005).

Non-scientific Courses

Lecturing and presenting in engineering, EPFL, Lausanne, Switzerland, (Nov 2022)

- Training on how to design and deliver lessons in engineering and science for diverse audiences.

My thesis in 180 seconds (MT180), EPFL, Lausanne, Switzerland, (Mar 2022)

- Training followed by a competition for presenting the Ph.D. research in plain language to a large and non-specialist audience of researchers, journalists, and business people.

Entrepreneurial opportunity identification and exploitation, EPFL, Lausanne, Switzerland, (Nov 2021)

- Training on the process of market opportunity identification and evaluation in the context of new technologies and training on practical tools such as the market opportunity navigator, business model canvas, and lean start-up methodology.

Innosuisse business concept, EPFL, Lausanne, Switzerland, (Sep-Dec 2020)

- Training with actual start-ups on practical tools to transform a project idea step-by-step into a concrete business concept, including Market analysis & value proposition, strong team building, protection of IP, product market fit, and financial planning.

Academic Projects

Bachelor Graduation Project, Mobile X-Ray Device with wireless control, HTI, 2012, Grade: Excellent.

Patient's body temperature remote monitoring – GSM/SMS based system, using LM35 sensor, Intel 8051 microcontroller.

Infant's Incubator - Controlling board using PIC 16F877A, LCD, and fan motor and simulation using Proteus Professional.

Skills

- COMSOL Multiphysics, Origin Pro, IviumSoft, Clewin, KLayout, Autodesk Inventor CAD, Adobe Illustrator.
- CellProfiler, ImageJ, QuPath, JMP, Tracker (Compadre), ZView, FLIR & Optris thermal systems.
- Circuit's designing and simulation applications: Proteus, Altium (basic experience)
- Lunaphore COMET™ and LabSat® devices, HORIZON™ software.
- Biosafety training levels 1, 2, and 3 (Basic)
- Programming languages: Python, MATLAB, C++, Python, 8051 assembly language
- Microcontroller programming: 8051 microcontrollers, PIC microcontroller.
- Strong multi-disciplinary background, self-motivated, team player, and challenge seeker.